JMeXFRI

Indexed in: EMBASE/Excerpta Medica, SciELO, BIBLAT, MIAR, DOAJ, ASCI-Database, Latindex
Preserved in: CLOCKSS

Journal of the Mexican Federation of Radiology and Imaging

J Mex Fed Radiol Imaging

Volume 4. Number 4, October-December 2025
ISSN: 2938-1215
eISSN: 2696-8444

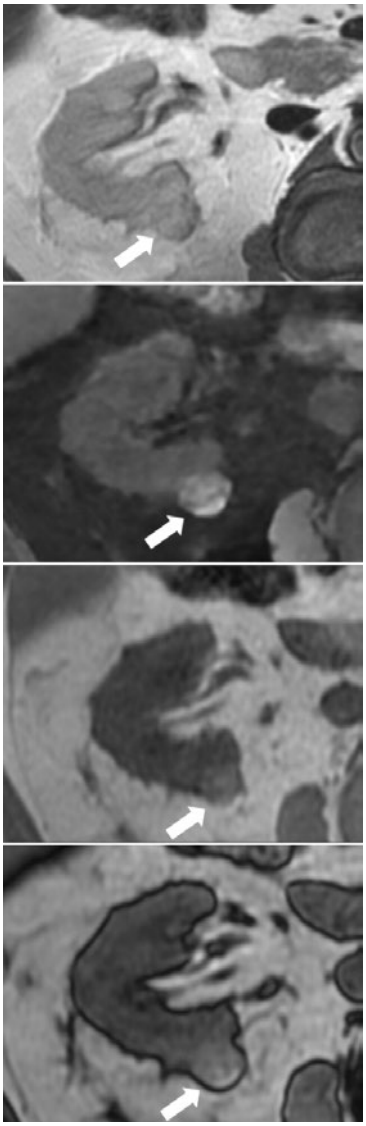

Official Journal of the

FEDERACIÓN MEXICANA DE RADIOLOGÍA E IMAGEN, A.C

PERMANYER
www.permanyer.com

WWW.JMeXFRI.COM

JMeXFRI

Journal of the Mexican Federation of Radiology and Imaging

J Mex Fed Radiol Imaging

Volume 4. Number 4, October-December 2025

ISSN: 2938-1215

eISSN: 2696-8444

The *Journal of the Mexican Federation of Radiology and Imaging* (JMeXFRI) is the official journal of the Federacion Mexicana de Radiologia e Imagen. The aim of the journal is to disseminate scientific knowledge and technological developments for innovation in diagnostic and therapeutic radiology with original articles on basic and clinical aspects of modern radiology in an international context with global impact. JMeXFRI is published in American English with 4 issues per year (print and online) and the first issue was published in the first quarter of 2022. Articles undergo a rigorous, double-blind peer-review process. Publication of articles in JMexFRI is free of charge and all published articles are open access.

The journal publishes the following types of manuscripts: *Full Research Article, Pictorial Essay, Brief Research Article, Technical Note, In-Depth Review, Case Report, Images in Radiology, and Editorial.*

EDITORIAL BOARD

Follow us

https://linkedin.com/company/jmexfri

https://instagram.com/jmexfri

https://facebook.com/jmexfri

https://youtube.com/@jmexfri

https://x.com/jmexfri

Original papers should be deposited in their electronic version through the following URL:

https://publisher.jmexfri.permanyer.com

PERMANYER
www.permanyer.com

Permanyer Mexico
Temistocles, 315
Col. Polanco, Del. Miguel Hidalgo
11560 Ciudad de Mexico
mexico@permanyer.com

Permanyer
Mallorca, 310 – Barcelona (Cataluña), España
permanyer@permanyer.com

www.permanyer.com

ISSN: 2696-8444
Ref.: 10990AMEX254

JMeXFRI

Journal of the Mexican Federation of Radiology and Imaging

Check for updates

EDITORIAL

Shaping global imaging and health policy: the importance of the International Society of Radiology

Bibb Allen

Department of Radiology, Grandview Medical Center, Birmingham, AL, USA; President, International Society of Radiology

The International Society of Radiology (ISR) is a century-old global leader in medical imaging. We are a federation of more than 70 national, continental, and regional radiology societies united by a common mission – to improve global health through greater access to safe, high-quality medical imaging and to promote radiological education, quality, and safety worldwide. Our federated structure enables radiology to speak with a unified voice on global issues affecting both our profession and the patients and communities we serve. For over 50 years, the ISR has been a Non-State Actor in official relations with the World Health Organization (WHO) and a trusted partner of the International Atomic Energy Agency (IAEA). These relationships allow us to bring diverse perspectives from around the world into health policy discussions, advocate for equitable access to imaging, and ensure that radiology expertise informs international standards and regulations. While other radiological societies engage in international outreach and collaborate with organizations such as the IAEA, the ISR is unique in having as its primary mission the improvement of health in low- and middle-income countries. This focus guides our collaborations, advocacy, and educational programs, ensuring our efforts are directed where they can have the greatest impact.

The value of collaboration with WHO and IAEA: since becoming a WHO Non-State Actor in 1969, the ISR has worked to integrate medical imaging into global health strategies. Our decades-long collaboration with the IAEA, formalized through Practical Arrangements, has advanced workforce training, radiation protection, and safe imaging practices. One milestone was the 2012 International Conference on Radiation Protection in Medicine, co-sponsored by WHO and IAEA, which produced the Bonn Call for Action – a roadmap of ten priorities to improve radiation protection for patients and healthcare workers. The ISR continues to align its quality and safety work with these principles, particularly in low-resource settings. In the Caribbean, the ISR partnered with the IAEA to deliver hands-on breast imaging and biopsy training in St. Vincent and the Grenadines and St. Lucia, strengthening diagnostic capacity and establishing a model for other underserved regions. These efforts underscore the ISR's unique position as radiology's unified voice in discussions with WHO, IAEA, health ministries, and other professional societies.

Imaging, NCDs, and a global ethical imperative: noncommunicable diseases (NCDs) such as cancer, stroke, and heart disease are now the leading causes of premature death worldwide, with the highest burden in low- and middle-income countries (LMICs). Early, accurate diagnosis, which is central to improving NCD outcomes, is impossible without the medical imaging capacity for timely diagnosis. Yet two-thirds of the world's population lack access to the medical imaging necessary for early diagnosis. This is not only a medical crisis but also an ethical imperative. Without imaging, early cancer detection, timely stroke intervention, and effective heart disease management cannot be delivered at scale. Closing this accessibility gap is

Corresponding author:
Bibb Allen
E-mail: bibb@mac.com

Received for publication: 13-08-2025
Accepted for publication: 14-09-2025
DOI: 10.24875/JMEXFRI.25000023

Available online: 15-01-2026
J Mex Fed Radiol Imaging. 2025;4(4):215-217
www.JMeXFRI.com

essential to reducing preventable deaths and addressing global health inequities.

Landmark Resolution at the 78th World Health Assembly: in May 2025, the 78th World Health Assembly (WHA) adopted the first-ever resolution focused solely on strengthening medical imaging capacity (WHA78.13, expanding on a 2023 WHA resolution on strengthening diagnostics capacity (WHA76.5)[1,2]. While Non-State Actors cannot introduce resolutions, the ISR, along with the Lancet Commission on Medical Imaging and Nuclear Medicine and the World Federation of Nuclear Medicine and Biology, strongly supported the measure introduced by the Republic of Cameroon as the primary sponsor, with Brazil and other Member States as co-sponsors. ISR's role included refining resolution language, recruiting support, and briefing WHA delegates in person in Geneva and through several online educational sessions. Brazil's co-sponsorship ensured that Latin America's priorities were represented in the development of the resolution. WHA78.13 recognizes that strengthening imaging is essential to reducing NCD mortality and other health burdens, and calls on Member States to:

- Make medical imaging available at the point of care, supported by transport, electricity, and internet infrastructure.
- Address financial, workforce, and policy barriers, especially in rural and underserved areas.
- Promote safe, high-quality imaging as part of integrated health systems.

The resolution's adoption validates decades of ISR advocacy and sets a clear mandate for action.

From resolution to lasting change: for the ISR, passing a WHA resolution is just the starting point for increasing access to medical imaging. However, lasting impact depends on its implementation. The ISR's approach is to link each priority area in the resolution to existing ISR-led programs, networks, and expertise to ensure rapid and sustainable progress:

- *Workforce development* – Expanding the capacity of radiologists, radiographers, and medical physicists through targeted on-site and virtual training. The ISR's Education Committee coordinates with regional societies to deliver webinars, short courses, and workshops tailored to local needs. Partnerships with the IAEA and WHO enable faculty exchange and curriculum development, while the ISR's online learning platform provides free access to educational materials worldwide. These programs emphasize not only clinical skills but also the development of sustainable training capacity within countries, enabling local leaders to continue education and mentoring long after the initial program ends.
- *Quality and safety* – Advancing best practices through the ISR Quality and Safety Alliance, which connects global campaigns and regional initiatives. By working with member-led programs such as Image Gently, EuroSafe Imaging, AFROSAFE, and LatinSafe, ISR helps standardize protocols, disseminate safety guidelines, and promote a culture of radiation protection in settings where awareness and resources are limited.
- *Technology and innovation* – Leveraging collaborations with artificial intelligence (AI) and data science experts, including the Medical Imaging Computing and Computer Assisted Intervention Society (MICCAI) initiative AFRICAI, the ISR helps create imaging tools adapted for LMIC realities. The AFRICAI pilot project on AI-assisted obstetric ultrasound in Africa demonstrated how local data scientists can adapt existing AI tools for resource-challenged settings and extend expertise to areas without subspecialists. Expansion to Southeast Asia and Latin America is planned, using open-access frameworks to minimize costs and enable local adaptation.
- *Guideline adaptation* – Partnering with WHO, IAEA, and disease-specific organizations to adapt imaging and screening guidelines for resource-limited settings. The ISR facilitates expert panels to ensure recommendations are evidence-based and practical, accounting for available equipment, workforce skills, and epidemiologic priorities in each region.
- *Equipment solutions* – Advising governments, NGOs, and donors on imaging technologies suited to infrastructure realities, including transport, installation, power supply, maintenance, and cost considerations. ISR's collaborations with industry partners and engineering groups help identify durable, cost-effective equipment that can function in challenging environments.
- *Advocacy and policy engagement* – Maintaining a strong ISR presence in WHO, IAEA, and other global policy forums. By contributing to the WHO Global Diagnostics Coalition[3] and the WHO Strategic and Technical Advisory Group on Medical Devices (STAG MeDev)[4], the ISR ensures imaging remains a central component of national and global diagnostic strategies.

Through these aligned efforts, the ISR can help WHO Member States in underserved areas translate the WHA resolution from policy into tangible improvements in access and quality.

The ISR Centennial, the ISR Béclère-Fuchs Foundation and a Leadership Opportunity for Latin America: Brazil's leadership as a WHA78.13 resolution co-sponsor creates momentum for the Americas. At the International Congress of Radiology (ICR) 2026 in Cartagena, Colombia, Brazil will present its national implementation strategy, providing a regional platform for collaboration among health officials, professional societies, and global partners. These discussions can guide other nations in scaling up imaging capacity and may serve as a blueprint for collective regional action. As the ISR marks its Centennial, we celebrate a century of progress while looking to the future. The new ISR Béclère-Fuchs Foundation supports mission-aligned projects, including expanding imaging access and training in underserved regions. Resources at isradiology.org highlight our history, partnerships, and current initiatives, and invite engagement and support for the Foundation from industry, professional societies, institutions, individuals, and other foundations.

In conclusion, the ISR brings together the global radiology community to ensure its expertise informs health policy at the highest levels. The WHA78.13 resolution offers a timely opportunity to translate the ISR's mission into measurable action. For Latin America and the Caribbean, this is a moment to lead. By building on Brazil's co-sponsorship, strategies developed at the ICR 2026 in Cartagena, and the strength of regional professional societies, radiologists can help ensure that access to life-saving medical imaging is determined by need, rather than geography.

Funding

The author declares that he has not received funding.

Conflicts of interest

The author declares no conflicts of interest.

REFERENCES

1. World Health Organization. Seventy-eighth World Health Assembly. Resolution WHA78.13: Strengthening medical imaging capacity. Geneva: World Health Organization; 2025 [cited 2025 Aug 13]. Available from: https://apps.who.int/gb/ebwha/pdf_files/WHA78/A78_R13-en.pdf.
2. World Health Organization. Seventy-sixth World Health Assembly. Resolution WHA76.5: Strengthening diagnostics capacity. Geneva: World Health Organization; 2023 [cited 2025 Aug 31]. Available from: https://apps.who.int/gb/ebwha/pdf_files/WHA76/A76_R5-en.pdf.
3. World Health Organization. Global Diagnostic Coalition. Geneva: World Health Organization; c2025 [cited 2025 Aug 31]. Available from: https://www.who.int/initiatives/global-diagnostic-coalition.
4. World Health Organization. Strategic and Technical Advisory Group of Experts on Medical Devices (STAG-MEDEV). Geneva: World Health Organization; c2025 [cited 2025 Aug 13]. Available from: https://www.who.int/groups/strategic-and-technical-advisory-group-of-experts-on-medical-devices-(stag-medev).

JMeXFRI

Journal of the Mexican Federation of Radiology and Imaging

Check for updates

IN-DEPTH REVIEW

State of the art: imaging of solid renal lesions

Mariem Bensalah-Faria[1]*, *Giorgio Raia*[1] and *Harriet C. Thoeny*[1,2]

[1]*Department of Radiology, Fribourg Hospital, University Teaching and Research Hospital;* [2]*University of Fribourg. Fribourg, Switzerland*

ABSTRACT

Renal lesions are frequently and increasingly detected as incidentalomas on different imaging techniques of the abdomen in various clinical contexts and concerning all age groups of patients. In this context, the radiologist's expertise plays a key role in accurately characterizing renal lesions leading to the optimal patient management, in order to efficiently treat malignant lesions while avoiding unnecessary interventions for benign lesions or in patients with underlying comorbidities limiting radical treatment. Cystic lesions are characterized by the Bosniak classification system and are out of the scope of this review. Solid renal lesions exhibit various morphological and functional imaging features that facilitate their characterization and contribute to the differentiation between benign and malignant entities. The aim of this review is to provide radiologists with a guide for accurate and up-to-date interpretation of solid renal lesions, leading to the most probable diagnosis and optimal management. This review begins with an overview of imaging modalities for renal lesions, followed by an analysis of key imaging features relevant to renal lesion characterization. Additionally, we present a literature-based analysis of the principal findings of relevant solid renal lesions. Finally, we propose a diagnostic algorithm to guide the radiologist's interpretation.

Keywords: *Kidney neoplasm. Renal cell carcinoma. Diagnostic ultrasound. Tomodensitometry. Magnetic resonance imaging. Dynamic contrast enhancement.*

INTRODUCTION

Renal lesions are frequently and increasingly detected as incidental findings on various imaging techniques of the upper abdomen in different clinical contexts and concerning all age groups of patients[1]. In the literature, reported rates of incidental renal findings range from 4% to 37%. These renal incidentalomas are predominantly of low clinical relevance, with simple cysts being the most commonly detected renal lesions. However, the vast majority of solid renal masses correspond to renal cell carcinoma (RCC). At least 60% of RCCs are detected incidentally[1,2].

Therefore, the radiologist's expertise in evaluating these renal lesions is of utmost importance[2], and represents a common concern in daily practice. In order to set the appropriate management – whether further imaging, biopsy, surveillance, ablation, surgery, or radiotherapy – it is crucial to characterize and differentiate between benign and malignant lesions as well as between specific diagnoses and RCC subtypes. Cystic lesions can be characterized using the Bosniak classification system[3]. Solid renal lesions are malignant in most cases, especially those larger than 4 cm; these are mainly RCCs, representing 2% of adult cancers[2]. The most common benign solid lesions are angiomyolipomas followed by oncocytomas[2]. Recognizing the features of typical benign renal lesions or slowly growing malignant lesions is noteworthy to be recognized in order to initiate or postpone active treatment and to

***Corresponding author:**
Mariem Bensalah-Faria
E-mail: mariem.bensalah@h-fr.ch

Received for publication: 30-09-2025
Accepted for publication: 21-10-2025
DOI: 10.24875/JMEXFRI.M25000114

Available online: 15-01-2026
J Mex Fed Radiol Imaging. 2025;4(4):218-232
www.JMeXFRI.com

avoid unnecessary surgical procedures and their potential side effects. Additionally, features of malignancy should be identified and characterized to ensure optimal treatment selection.

The aim of this review is to provide a guide that will allow the radiologist to perform accurate and up-to-date interpretation of solid renal lesions, and to propose the most probable diagnosis, leading to the optimal management option. This review begins with an overview of imaging modalities and protocols for renal lesions, followed by a detailed analysis of the key imaging features relevant to renal lesion assessment. We then present a literature-based analysis of the principal characteristics of relevant solid renal lesions. Finally, we propose a diagnostic algorithm to guide the radiologist's interpretation.

IMAGING TECHNIQUE AND PROTOCOL

Incidental renal lesions are most often detected on computed tomography (CT) scans, usually with a single portal venous phase performed for unrelated indications such as oncologic staging, trauma assessment, or evaluation of inflammatory or infectious conditions, as well as on ultrasound or magnetic resonance imaging (MRI) for example in the context of liver cirrhosis. While some incidental renal lesions can be easily diagnosed, many require further assessment with a dedicated imaging technique: contrast-enhanced CT, spectral CT, kidney-specific MRI protocol or contrast-enhanced ultrasound (CEUS)[2]. To assess the enhancement pattern, a multiphasic imaging should be performed, including non-contrast, early arterial phase, and parenchymal phase with intravenous contrast material[2]. The multiparametric MRI protocol for evaluating renal lesions at our institution includes T2-weighted images (T2-WI), chemical shift imaging (in-phase and opposed-phase), T1-weighted images (T1-WI), fat-saturated T1-WI pre- and post-contrast, diffusion-weighted imaging (DWI) and dynamic contrast-enhanced (DCE) sequences. Image subtraction is extremely important to assess and highlight enhancement areas especially in T1 hyperintense lesions. In cases of small renal lesions, contraindications to contrast media, or impaired renal function, MRI is preferred followed by CEUS[2].

On ultrasound, incidental renal lesions can be classified as cystic or solid, and their morphological features can be assessed (echogenicity, size, location, local and vascular extension). CEUS offers the advantage of evaluating the lesion´s enhancement pattern compared to adjacent renal parenchyma, as well as the presence or absence of a pseudo-capsule defined as rim enhancement. Although CEUS is useful, especially in patients with renal impairment, it is limited by availability, user dependence and less robust supporting data[4]. Furrer et al.[5] in their meta-analysis, showed that CEUS performs similarly to contrast-enhanced CT and MRI in distinguishing benign from malignant cystic and solid renal lesions, although the data analysis had limitations (data heterogeneity, a small number of MRI studies, and high risk of confounding factors). Nonetheless, in another systematic review assessing the performance of these imaging techniques performance for diagnosing and staging RCC, CEUS showed satisfactory sensitivity but mediocre specificity[6]. Contrast-enhanced CT and MRI remain the standard imaging modalities[6].

APPROACH FOR IMAGING ASSESSMENT

Upon detection of a renal lesion, comprehensive characterization of key imaging features should be performed.

Mass type

The first step is to differentiate between cystic and solid lesions. If the lesion is cystic, diagnosis and management are based on the Bosniak classification system[3], which is out of the scope of this review article. A solid lesion is defined by the presence of more than 25% of a tissue component enhancing after contrast medium administration on CT or MRI[3,7].

Shape and margins

A solid lesion can be massforming or expansile, with well-defined margin that deforms the renal contour. On the other hand, it can be infiltrative, with ill-defined margins that preserve the kidney's bean shape and contour. These lesions are more challenging to identify, especially on non-contrast CT.

Capsular location – endophytic/exophytic

An exophytic renal mass with an angular interface with the renal cortex on coronal T2-WI is highly predictive of being benign, especially if the lesion measures 2 cm or larger with a reported sensitivity of 78% and specificity of 100%[8].

Location

A lesion may be centrally or peripherally located, depending on its origin.

Size

The lesion should be measured in three orthogonal dimensions. The risk of malignancy increases with lesion size. The probability of benignity is approximately 40% for lesions less than 1 cm, 20% for lesions measuring 1-4 cm, and decreases to 10% for lesions greater than 4 cm[9]. Because small lesions (< 1 cm) are almost impossible to characterize, follow-up is usually suggested, and immediate intervention is not recommended[9].

Growth rate

If previous radiological exams are available, comparative assessment can help differentiate benign from malignant solid lesions. Obvious and rapid growth may indicate malignancy. A stable lesion over time does not exclude malignancy; morphological and functional parameters must be considered in the radiological interpretation. However, a renal lesion with an average growth rate of less than 3 mm/year during at least 5 years of follow-up, without changes in other imaging features, can be considered stable and is most likely of no clinical significance[9]. Additionally, some MRI features have been reported to predict the growth rate of solid renal lesions such as lesion homogeneity on T2-WI and post-contrast images and T2 hypointensity, which may be associated with slowly growing renal lesions[10].

Presence of calcifications, necrosis, or hemorrhage

Extension-Invasiveness

The extension to the collection system, perirenal fat and fascia, adjacent organs, as well as the assessment of venous thrombosis should be analyzed. In fact, determining collecting duct invasion is crucial for local staging of RCC[2].

MRI signal intensity on T1-WI and especially on T2-WI

Macroscopic fat

Defined as density of less than – 20 Hounsfield units (HU) on non-contrast CT, high signal on T1- and T2-WI, loss of signal on fat-saturated sequences and “India ink” artifact at fat-water interfaces on opposed-phase chemical shift sequences. The presence of these features should immediately suggest angiomyolipoma (AML).

MRI detection of intracellular lipid

Intracellular lipid represents the intravoxel coexistence of small amounts of fat and water, resulting in a signal intensity drop on opposed-phase images compared with in-phase images. This feature can help distinguish renal lesions, as it may be present in lipid-poor AML, which lacks bulk fat, as well as in RCCs, namely clear cell RCC. Some studies have investigated the chemical shift signal intensity index of these renal lesions, but no established threshold has been determined yet[11-13].

Contrast-enhancement CT

On CT, enhancement is defined as an increase in density of at least 20 HU between pre- and post-contrast acquisitions. A change of 10-20 HU is considered equivocal. On MRI, enhancement is defined as an increase of 15% in signal intensity after contrast medium administration[9]. Image subtraction is essential for detecting enhancement in equivocal cases.

To improve the radiological characterization and diagnosis of renal lesions, some studies have assessed enhancement patterns using multiphasic contrast enhanced CT or MRI, by measuring the difference in signal intensity between pre-contrast and each post-contrast phase[14,15]. For example, clear cell RCCs typically show strong enhancement in the corticomedullary and nephrographic phases, followed by a plateau in the excretory phase[14,15]. In contrast, papillary RCCs show little enhancement in the corticomedullary and nephrographic phases, with a plateau in the excretory phase[14]. Moreover, chromophobe RCC shows an enhancement pattern intermediate between the previously mentioned RCCs[14].

Diffusion-weighted imaging (DWI)

The diagnostic performance of various DWI parameters, namely the apparent diffusion coefficient (ADC) value, has been investigated in several studies[16-22]. Although it has been reported that the ADC, a quantitative DWI parameter, is not useful for differentiating benign from malignant lesions[23], it can help characterize renal lesions, especially when combined with other sequences and morphological imaging features[16]. In fact, diffusion restriction and low ADC values may be

observed in both malignant and benign lesions, such as RCCs, AMLs, and abscesses. In a recent meta-analysis, Tordjman et al.[18] demonstrated that clear cell RCCs exhibit higher ADC values than other RCC subtypes (papillary RCCs, and chromophobe RCCs), and lipid-poor AML, but lower ADC values than oncocytomas. Another key finding of this study was that measuring the ADC in selected regions was more reliable and accurate than using the whole lesion ADC[18]. In fact, necrotic, cystic, and hemorrhagic tumor components may mask true ADC values and changes related to tumor tissue cellularity. In the same study[18], the pooled sensitivity and specificity for distinguishing clear cell RCC from other tumors were satisfactory, but moderate (80% and 78%, respectively).

DWI may be better suited as a complementary tool to morphological features and enhancement patterns rather than as a primary method for RCC subtype characterization[24]. Furthermore, there are no absolute ADC values that allow differentiation between benign and malignant renal lesions or characterization of each histologic type.

Spectral CT

Dual-energy CT (DECT), based on image acquisition at two different energy levels, has been increasingly used and investigated in the context of renal lesion assessment[25]. Compared to standard CT, spectral CT offers improved tissue characterization by distinguishing different components, as each material has its own spectral response for each energy band. Additionally, it offers several post-processing algorithms that generate various images: virtual unenhanced images (VUE) through iodine subtraction, iodine maps showing areas of iodine uptake, monoenergetic images, and optimum contrast images that improve image quality. Additionally, it allows for better correction of iodine-induced beam hardening artifacts, reducing the pseudo-enhancement effect[25].

Unenhanced images play a crucial role in detecting hemorrhage and calcifications, classifying cystic renal lesions, and represent a reference for evaluating contrast-enhanced acquisitions[3,9,25]. VUE images, by potentially replacing true unenhanced CT (TUE) images, may reduce the need for additional investigations, radiation dose, healthcare costs, and acquisition time, supporting sustainable radiology principles[26]. Several studies have shown that VUE and TUE are comparable in assessing renal enhancement, with no significant difference in renal lesion attenuation[27-29]. However, some studies have reported variability in attenuation measurements of renal lesions between VUE and TUE imaging[30-34]. For example, Cao et al.[32] demonstrated a significant difference in attenuation measurements and concluded that VUE images underestimated the attenuation of simple and spontaneous hyperdense renal cysts. Discrepancies in attenuation values between different DECT scanner types have been reported, particularly during follow-up[35]. Therefore, the use of VUE reconstructions in clinical setting remains controversial and cannot yet confidently replace TUE images, yet. Further research is needed to understand the impact of post-processing algorithms and noise reduction techniques on attenuation values[25].

Additionally, quantification of iodine concentration within renal lesions, expressed in mg/mL, is a promising tool for characterizing renal lesions, especially those with equivocal enhancement and spontaneous density between 20 and 70 HU[25,36]. Several studies have shown that iodine quantification can distinguish between enhancing and non-enhancing lesions, although a concentration threshold has not yet been defined[30,37-39]. Furthermore, iodine maps have been shown to help discriminate between RCC subtypes, which have different blood supply and vascularity[40,41].

TYPES OF SOLID RENAL LESIONS

Renal tumors include a wide range of histopathological types, as defined in the 5th edition of the World Health Organization (WHO)[42] classification of urogenital tumors, published in 2022. In addition to morphology-based classification, this updated edition incorporates several newly defined entities based on molecular features, marking a shift toward molecular-based categorization[42]. In this review article, we summarize the key imaging characteristics of the main radiologically described types of renal lesions.

BENIGN RENAL LESIONS

Angiomyolipoma (AML)

These are the most common benign solid renal lesions, composed of varying amounts of fat, smooth muscle, and blood vessels. Most cases are sporadic (80%), but they can be associated with syndromes such as tuberous sclerosis and lymphangioleiomyomatosis. Based on fat content, subtypes include classic AML (95%), lipid-poor AML (5%), and epithelioid AML[43,44].

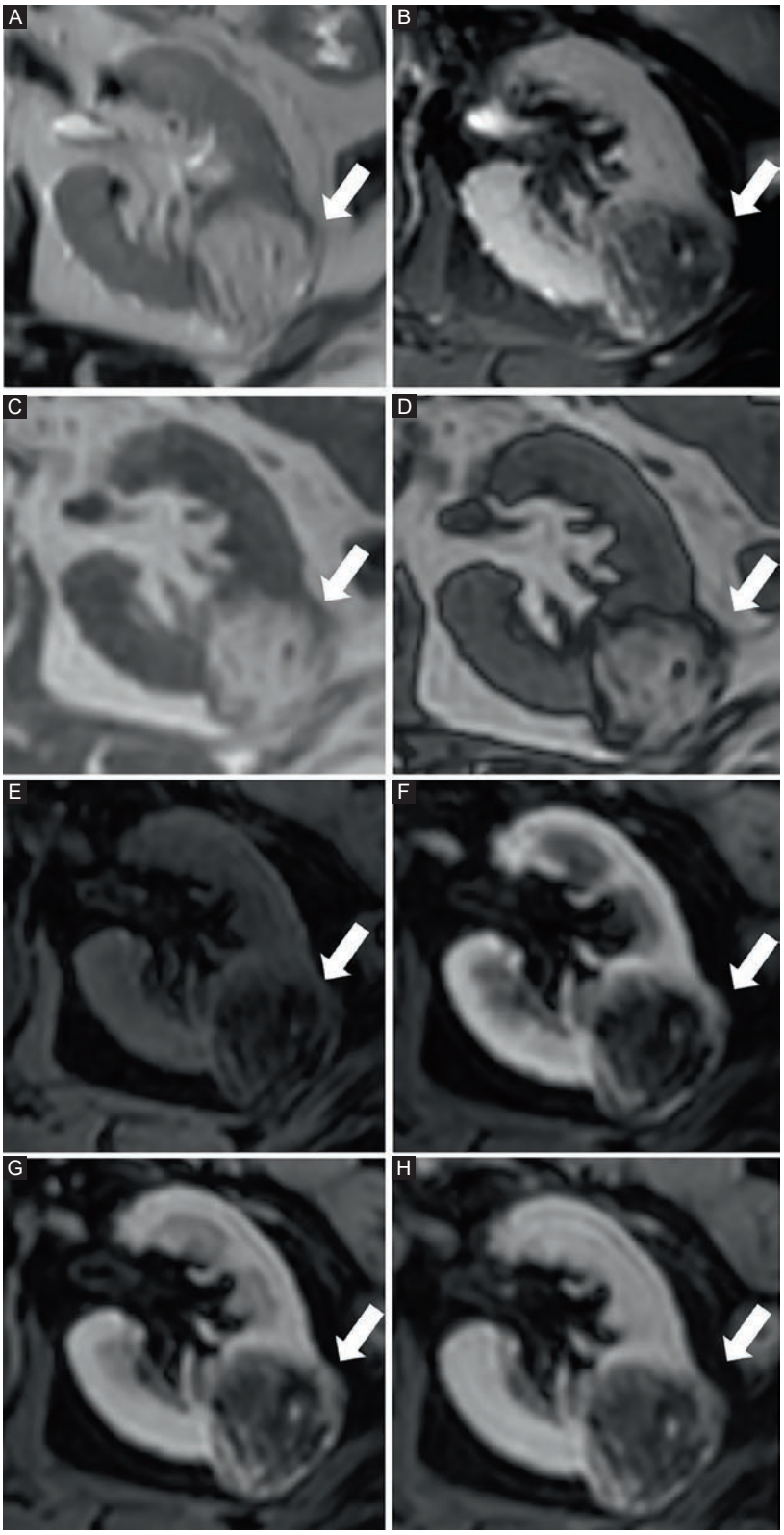

Figure 1. MRI of a 71-year-old woman with a left renal AML **A:** a typical appearance, characterized by a signal similar to fat, hyperintense on T2-WI (arrow). **B:** signal drop on T2 fat-saturated sequence (arrow). **C:** hyperintense on T1-WI (arrow). **D:** no signal drop on T1 opposed-phase image (arrow). **E:** hypointense on T1 fat-saturated non-contrast sequence (arrow). **F:** arterial phase, **G:** venous phase, and **H:** late phase T1 post-contrast images show heterogeneous enhancement, corresponding to the vascular component (arrows).

MRI: magnetic resonance imaging; AML: angiomyolipoma; T2-WI: T2-weighted image; T1-WI: T1-weighted image.

Classic AML

It is heterogeneous and exhibits the hallmark feature of abundant macroscopic fat, making it easy to diagnose on cross-sectional imaging. It shows low density on non-contrast CT (< 10 HU), high signal on T1- and T2-WI, loss of signal on fat-saturated sequences, and an "India ink" artifact at fat-water interfaces within the AML and at its border with adjacent renal tissue on opposed-phase chemical shift sequences. The non-fat-containing component enhances homogeneously, and the muscle component is T2 hypointense (Figure 1). On ultrasound, classic AMLs typically appear hyperechoic, with a hypo- or anechoic rim; aneurysms and bridging vessels may also be identified[45].

One serious complication of AMLs to consider is eventual hemorrhage due to intra-tumoral microaneurysm rupture, particularly when AMLs are larger than 4 cm[43]. However, the association between AML size and hemorrhage risk remains unclear[2]. In rare cases, AMLs can be exophytic and challenging to differentiate from perinephric liposarcomas. Some features are discriminating and suggestive of AMLs, such as a renal parenchymal defect (claw sign), other intrarenal fatty lesions, encapsulated margins, and intra-tumoral enlarged vessels with aneurysms[46,47]. In contrast, liposarcomas are frequently associated with anterior displacement of the ipsilateral kidney without parenchymal defect, intramural calcification, and non–fat-attenuating enhancing intra-tumoral nodules[48].

Lipid-poor AML

It is usually homogeneous and tend to be small, with an average diameter of 3 cm[49]. They are typically isoechoic on ultrasound, iso- or hyperdense on non-contrast CT, and hypointense on T1- and T2-WI due to their tissue content composed of smooth muscle[44]. Typically, no signal drop is observed on fat-saturated or opposed-phase images. However, chemical shift suppression can be present in some cases, particularly in iso-attenuating lipid-poor AMLs with some diffuse fat cells among their vascular and fibrous components[44,49,50]. Unlike classic AMLs, lipid-poor AMLs can be challenging to diagnose, as their features overlap with those of RCCs, especially papillary RCCs. Although their enhancement pattern is variable, they are usually characterized by early intense enhancement followed by washout, unlike papillary RCCs, which are hypovascular and exhibit progressive enhancement[49,50]. Additionally, a meta-analysis by Wilson et al.[51] reported that MRI has satisfactory accuracy in detecting lipid-poor AMLs despite variability in MRI sequences and parameters.

Epithelioid AML

It is an extremely rare variant of lipid-poor AML, corresponding to a potentially malignant mesenchymal tumor that may behave aggressively, with vascular, local, and even regional extension, for which surgical resection is recommended. These tumors are difficult to distinguish from benign AMLs due to the lack of characteristic imaging features. However, in a study by Di Wang et al.[52] it has been reported that epithelioid AMLs tend to be larger, are more heterogeneously hyperdense on non-contrast CT, and show a faster and stronger enhancement pattern than other lipid-poor AMLs.

Oncocytoma

Oncocytomas are considered benign tumors that represent 3-7% of solid renal masses[53]. Their imaging features are nonspecific and may overlap with those of RCCs. They are typically well-defined with sharp, regular contours (Figure 2). They usually appear as isodense lesions on non-contrast CT, hypointense on T1-WI and hyperintense on T2-WI[53,54]. Homogeneous late enhancement with a central scar is seen in about 50%-60% of cases and is suggestive of oncocytoma, but not diagnostic[49,55]. Scars are difficult to distinguish from necrosis or cystic changes seen in renal cancers[53,56]. Another possible distinguishing feature is the segmental enhancement inversion sign, which describes a "flip-flop" of enhancement between the tumor and central scar on early and late phases after contrast agent administration[53,57]. However, this sign is not specific and can also be seen in RCCs[53,58]. Furthermore, the role of DWI in differentiating oncocytoma from RCC has been studied, but without robust results. Some studies have found that oncocytomas have significantly higher ADC values compared with RCCs[18,20,22,24,59] while Hötker et al.[19] reported similar ADC values for both tumor types. These findings may be explained by the variability in oncocytoma cellularity[53] or by the measurement of heterogeneous lesions.

Renal papillary adenoma

Renal papillary adenoma is a rare benign lesion, and the most common renal epithelial neoplasm[42]. It has been reported in 7% of renal resections performed for other lesions, mainly RCC[60], with an incidence of 19% in an autopsy study[61]. Papillary adenomas are usually found in patients with chronic renal damage such as

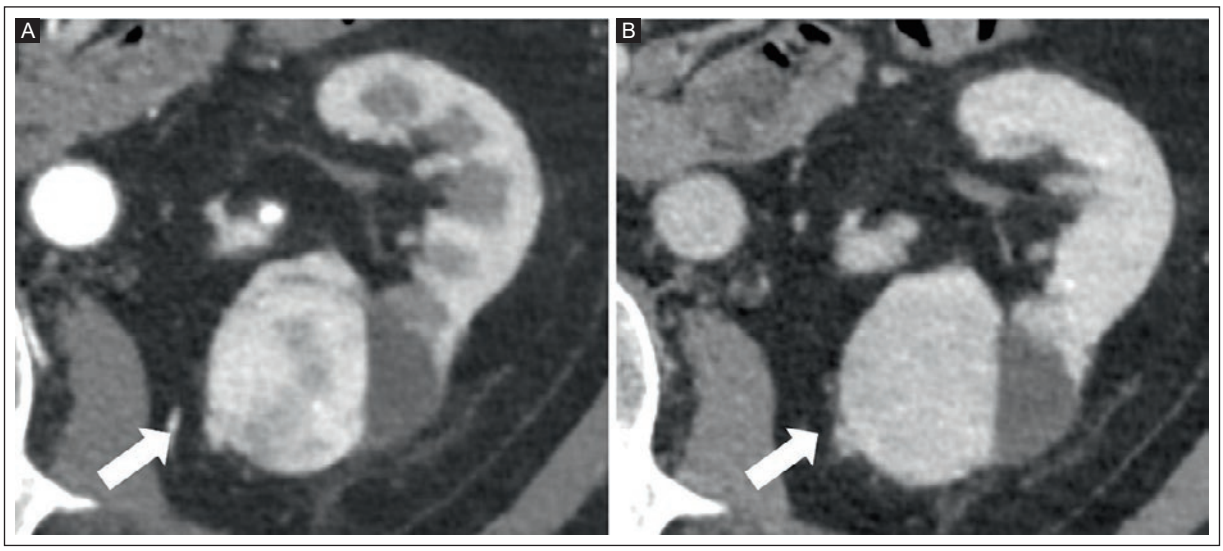

Figure 2. CT of an 84-year-old man with a left kidney oncocytoma. **A:** arterial phase, and **B:** portal phase show a well-defined expansile lesion with strong and homogeneous late enhancement (arrows).
CT: computed tomography.

renal cystic disease or in patients with prolonged dialysis[61,62]. They are typically small (< 15 mm) and lack specific imaging features[42,62]. However, they often appear with a mildly hypointense T2 signal, an isointense T1 signal, and poor enhancement[63]. They are difficult to differentiate from other renal tumors, especially papillary RCC[62,63]. Papillary adenomas can be solitary or multiple in cases of renal adenomatosis[63]. It is postulated that it might be precursor lesion to papillary RCC[60].

Metanephric adenoma

Metanephric adenoma is a rare renal neoplasm, that has been reported at any age, with peak prevalence in the fifth decade, and a female predominance. It typically appears as a well-circumscribed, unilateral, expansile, unencapsulated, and centrally located lesion originating from the medulla. It usually appears hyperdense on non-contrast CT, iso- to hypointense on T1-WI, and iso- to slightly hyperintense on T2-WI. It can be homogeneous or heterogeneous containing hemorrhage, necrosis and calcifications (20%). It is a hypovascular tumor characterized by a progressive, mild and prolonged enhancement. Some cases of metanephric adenoma have been described to contain foci of papillary or clear cell RCC at postoperative histopathology[64].

Juxtaglomerular cell tumor (reninoma)

Reninoma is a rare functional renin-producing tumor arising from afferent arteriolar juxtaglomerular cells, leading to hyperaldosteronism[42,65]. In the literature, fewer than 200 cases have been described since its discovery, and its prevalence is not well known[65]. Reninoma is usually seen in young adults (second and third decades), with a female predominance[65,66]. It appears as well-defined cortical mass, with variable radiological features. Nonetheless, it is usually hypoechoic on ultrasound[67], hypodense on non-contrast CT, iso-intense on T1-WI and shows variable T2 signal[68]. On contrast-enhanced imaging, it demonstrates mild enhancement during the delayed phase[68]. Surgical resection allows the treatment of hyperaldosteronism, especially the associated hypertension[65].

Renomedullary interstitial cell tumor (medullary fibroma)

Medullary fibroma is a rare benign renal mesenchymal tumor, frequently asymptomatic and commonly described in autopsy series, though it may be detected incidentally on imaging or in renal excision specimen[69,70]. In the literature, it has been described as a well-defined small millimetric lesion, that may measure up to 5 cm[66,70]. It is hypodense on CT, with low T2 and T1 signal on MRI, and mild enhancement[66,71]. These radiological characteristics reflect its pathological fibrous content and low cell density[71]. The differential diagnosis includes papillary RCC and lipid-poor AML. However, these tumor types have higher cellularity and are therefore hyperintense on DWI sequences with diffusion restriction on the ADC map, unlike medullary fibromas[71].

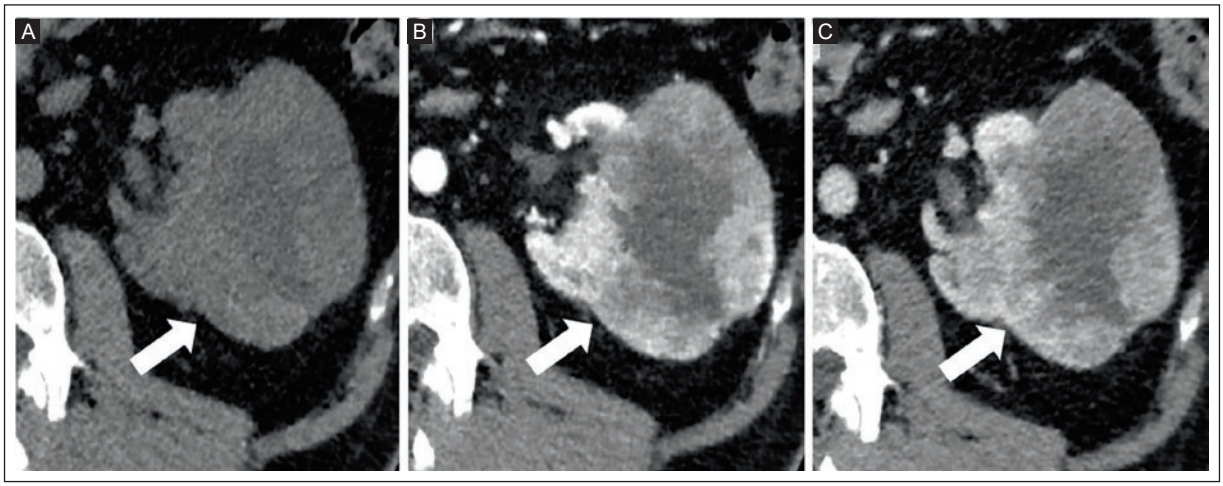

Figure 3. CT of a 53-year-old man with a left-kidney lesion diagnosed as ccRCC. **A:** hypodense lesion with a necrotic central part on non-contrast CT (arrow). **B:** arterial phase, and **C:** nephrographic phase, show strong and heterogeneous enhancement (arrows).
CT: computed tomography; ccRCC: clear cell renal cell carcinoma.

Leiomyoma

It is a rare renal mesenchymal lesion with a prevalence of 5% based on autopsy findings with a scarce imaging literature. It has been described as a peripheral, capsular or subcapsular, or peripelvic lesion that is well-defined and hyperdense on non-contrast CT, with a density similar to that of muscle, and mild enhancement less than that of renal parenchyma[72].

MALIGNANT RENAL LESIONS

Renal cell carcinoma (RCC)

It is the most common malignant solid renal tumor, accounting for 90% of cases. It is typically diagnosed at a median age of 65 years and occurs more frequently in male patients. Major risk factors include cigarette smoking, dialysis, and hypertension. The main histologic subtypes are clear cell RCC (ccRCC, 75%), followed by papillary RCC (papRCC, 15%), and chromophobe RCC (chRCC, 5%). ccRCC is the most aggressive subtype, with the lowest 5-year survival rate (44-69%), while papRCC and chRCC have a more favorable prognosis, with a 5-year survival rate of approximately 90%. ccRCC has the highest likelihood of metastasis, particularly at diagnosis, accounting for 94% of metastatic RCCs, mainly to the lungs[73,74]. Other metastatic sites include the brain, bones and adrenal glands. On ultrasound, RCCs usually appear iso- or hypoechoic relative to the renal parenchyma, with eventually hyperechoic regions representing intratumoral fat[45].

Clear cell renal cell carcinoma (ccRCC)

It is usually sporadic (95%) and is associated with hereditary syndromes in 5% of cases such as Von Hippel Lindau disease and tuberous sclerosis. It appears as an expansile, hypervascular tumor that may contain necrosis, intratumoral hemorrhage, and/or microscopic fat. It is characterized by heterogeneous, strong, and early enhancement on arterial and nephrographic phases after contrast agent administration (Figure 3). On MRI, ccRCCs typically appear hyperintense on T2-WI, and hypo- to isointense on T1-WI[49,74]. Intracellular fat can be detected on opposed-phase chemical shift images as a drop in signal relative to the in-phase sequence of at least 25%, allowing differentiation from other RCC subtypes. However, this feature can also be seen in lipid-poor AML[13,19]. Additionally, ccRCC tends to show a high ADC value, significantly higher than other RCC subtypes[18,23]. A pseudocapsule may be seen as a hypointense rim on T1- and T2-WI, representing compression of adjacent healthy renal tissue. Interruption of the pseudocapsule suggests perirenal fat invasion[49]. It is also important to assess for vascular invasion, as ccRCC has a tendency to extend into vessels, leading to thrombosis, mainly in the renal veins and inferior vena cava[49,74].

Papillary renal cell carcinoma (papRCC)

It appears as a well-defined, homogeneous, peripherally located, hypovascular lesion. This tumor tends to exhibit a mild and progressive enhancement after

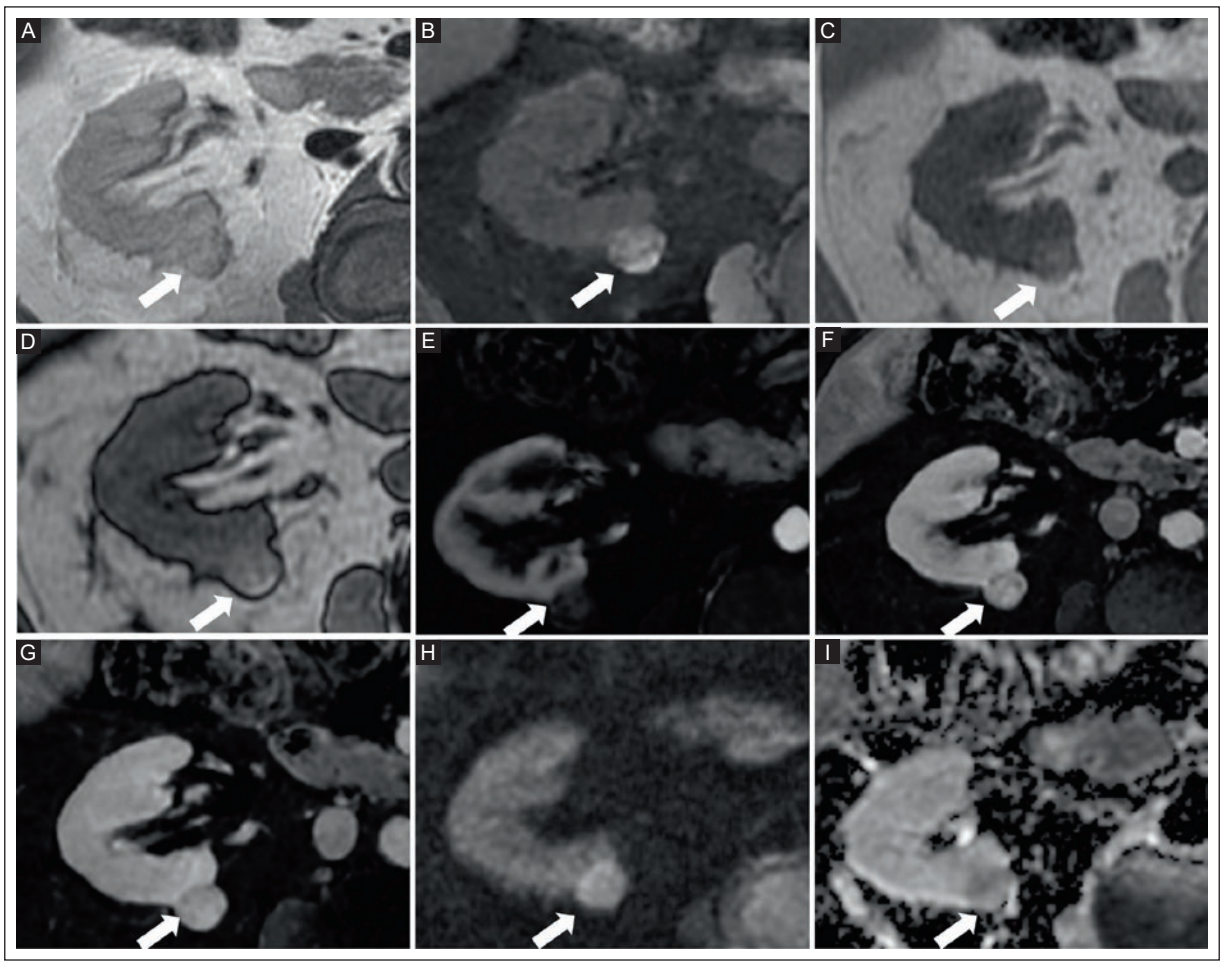

Figure 4. MRI of a 62-year-old man diagnosed with right-kidney papRCC[a]. **A:** well-circumscribed lesion, appearing isointense on T2-WI (arrow). **B:** the lesion appears mildly hyperintense on T1 fat-saturated non-contrast sequence suggesting hemorrhagic content (arrow). **C:** in-phase, and **D:** opposed-phase T1-WI show no signal drop (arrows). **E:** arterial phase subtraction, **F:** venous phase subtraction, and **G:** late phase subtraction show mild and progressive enhancement of the lesion (arrows). **H:** the lesion appears hyperintense on DWI at b-value 800 s/mm^2, and **I:** hypointense on ADC map, corresponding to diffusion restriction (arrows).

[a]On histopathology, this tumor was diagnosed as papillary renal neoplasm with reversed polarity, an emerging variant of papRCC. MRI: magnetic resonance imaging; papRCC: papillary renal cell carcinoma; T2-WI: T2-weighted image; T1-WI: T1-weighted image; DWI: diffusion weighted imaging; ADC: apparent diffusion coefficient.

contrast agent administration (Figure 4). It demonstrates marked T2 hypointensity due to intratumoral hemosiderin content. Necrosis, hemorrhage, and calcifications are rare but may occur in lesions larger than 4 cm[49,74]. Microscopic fat is extremely rare. A fibrous capsule is usually present, appearing hypointense on both T1- and T2-WI[49]. PapRCC tends to have lower ADC values than ccRCC[18]. However, ADC values are not reliable in this context because of the frequent presence of intratumoral hemosiderin.

Chromophobe renal cell carcinoma (chRCC)

It can be associated with the hereditary Birt-Hogg-Dubé (BHD) syndrome. This tumor lacks a pathognomonic radiologic appearance and can be difficult to distinguish from other solid renal masses, particularly oncocytoma. However, some common features have been described for chRCC: a well-circumscribed lesion without a defined capsule, typically confined to the kidney, with local and vascular extension being uncommon, a homogeneous T1 hypointense lesion with variable signal intensity on T2-WI, and absence of macroscopic or microscopic fat or hemorrhage. Necrosis is rare. On MRI, a central scar is seen in about 40% of cases, making it indistinguishable from oncocytoma. Additionally, chRCC is a hypovascular tumor compared to the renal cortex (Figure 5). Therefore, it enhances less than the cortex during all phases of contrast injection and tends to enhance more than

papRCC but less than ccRCC. Compared to lipid-poor AML, chRCC shows a later peak enhancement[49,73,76]. On DWI, chRCC demonstrates significantly lower ADC values than oncocytomas and ccRCC[18,21].

OTHER RARE RCCs

Renal medullary carcinoma (RMC, SMARCB1-deficient renal medullary carcinoma)

This rare neoplasm accounts for 1%-2% of renal cancers and predominantly affects young male adults with sickle cell trait, mainly of African or Mediterranean descent[75,76]. It is aggressive, with a mean survival of 15 months, for which chemotherapy may be recommended[76]. Metastatic disease is usually present at diagnosis, commonly involving regional lymph nodes, lungs, liver, adrenal glands, or the contralateral kidney[75].

On imaging, RMC appears as a centrally located solid mass in the renal medulla, with an average maximum length of 6 cm, often ill-defined with infiltrative borders[76,77]. This tumor frequently extends into the renal sinus, renal cortex, and perinephric fat, while preserving the overall renal bean shape, and is usually associated with calyceal dilatation. Intratumoral hemorrhage and necrosis are commonly observed, resulting in a heterogeneous appearance on CT and possible signal voids on T2-WI. Due to its hypovascular nature, it is hypoenhancing compared to the renal parenchyma[76,78].

Collecting (Bellini) duct carcinoma (CDC)

It has a low incidence, representing 1% of renal cancers, and a poor prognosis, with median overall survival ranging from 7 to 24 months. It is frequently associated with regional and distant metastases at diagnosis (around 40%)[79-81]. Due to their rapid growth, CDCs are usually symptomatic at diagnosis, unlike other renal cancers that may be detected incidentally[79,80]. Imaging findings are not specific for CDC, which may be misdiagnosed as nephritis, such as renal tuberculosis[80], or as other subtypes of renal cancers such as: RMC, RCC with sarcomatoid features, and urothelial carcinoma[79,80,82]. Nonetheless, the following CT and MRI features are common: infiltrative tumor with preserved reniform shape, medullary location, low and heterogeneous enhancement, cortical extension and extension into the renal sinus, areas of necrosis, and cystic components[79-81,83]. It has been reported that the CDC parenchymal component shows a higher density than the surrounding healthy renal tissue on non-contrast CT, and an iso- to hypointense signal on T2- and T1-WI[81,83]. These characteristics can be explained by the highly fibrous and collagenized nature of CDC[81].

Eosinophilic solid and cystic RCC

Eosinophilic RCC is an emerging and rare pathological entity defined in the 2022 WHO classification[42], whose radiological characteristics are not well defined yet. Previously, it used to be diagnosed as an "unclassified renal cell carcinoma"[84,85]. It has been described as an indolent, asymptomatic tumor with female predominance, and is associated with tuberous sclerosis in 10% of cases[85]. It appears as a unique, well-defined heterogeneous mass with solid and cystic components[84,85], characterized by lower and more persistent enhancement than ccRCC[86].

RENAL PELVIC TUMORS

Urothelial cell carcinoma (UCC, previously known as transitional cell carcinoma)

Upper tract UCC has a peak incidence in adults aged 60 to 70 years and affects men twice as often as women. The major risk factors are cigarette smoking and chemical carcinogens[78]. UCC usually appears as a superficial low-grade lesion corresponding to a focal intraluminal mass in the renal collecting system[87]. However, in 15% of cases, it can be more aggressive appearing as an infiltrative mass, characterized by irregular thickening of the upper tract wall, causing obstruction and dilation of the sinus or calyces, with ill-defined extension into the renal parenchyma while preserving its contours (Figure 6). On ultrasound, these tumors typically appear hypoechoic and can be slightly hyperechoic to the renal cortex but more hypoechoic than the renal sinus fat[45]. Given its multicentric nature, a careful assessment of the entire urinary tract is needed. In cases of suspected UCC percutaneous biopsy is avoided due to the high risk of tumor seeding. Findings at presentation may include retroperitoneal spread, regional lymph node involvement, and distant metastases (lungs and bones)[78,87].

Squamous cell carcinoma (SCC)

Renal pelvic SCC is a rare renal neoplasm, that typically appears as an extensive infiltrative mass invading

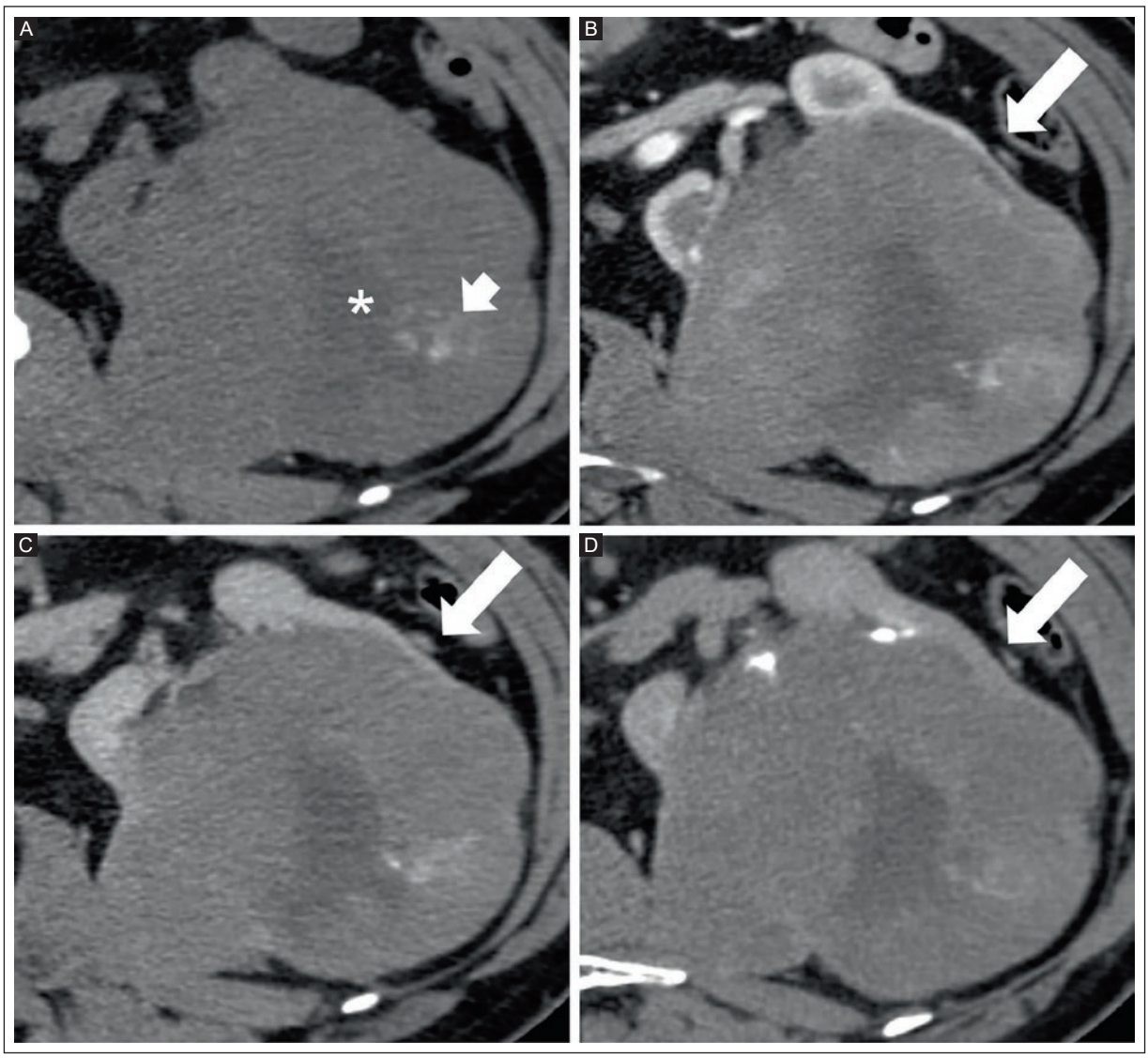

Figure 5. CT of a 74-year-old man diagnosed with a left-kidney chRCC. **A:** non-contrast CT shows an expansile heterogeneous lesion with a necrotic central area (asterisk) and calcifications (arrow). **B:** arterial phase, **C:** nephrographic phase, and **D:** excretory phase show minimal peripheral enhancement explained by its hypovascularity (arrows).

CT: computed tomography; chRCC: chromophobe renal cell carcinoma.

the renal sinus, with marked hydronephrosis, and is associated with lithiasis in half of cases[78]. It can also be associated with the parasitic infection schistosomiasis, as chronic urothelial inflammation results in squamous metaplasia[78,88]. Extraluminal extension is frequent, particularly into the psoas muscle[78].

Renal lymphoma

Renal lymphoma can present with diverse imaging appearances. It may appear as bilateral renal masses with little contrast enhancement on CT or MRI. These tumors can also present as retroperitoneal tumors with direct renal invasion, as bilateral enlargement of the kidneys or as a perirenal soft tissue mass[78].

Metastases

Renal metastases are usually seen in advanced stages of primary malignancies, most commonly lung cancer, followed by gastrointestinal tumors and breast cancer. They typically appear as small, multifocal, bilateral infiltrative lesions with mild enhancement. Strong enhancement may be seen in cases of melanoma and occasionally breast cancer. Rarely, metastases appear as a solitary lesion, making differentiation from a primary renal tumor or RCC challenging[78].

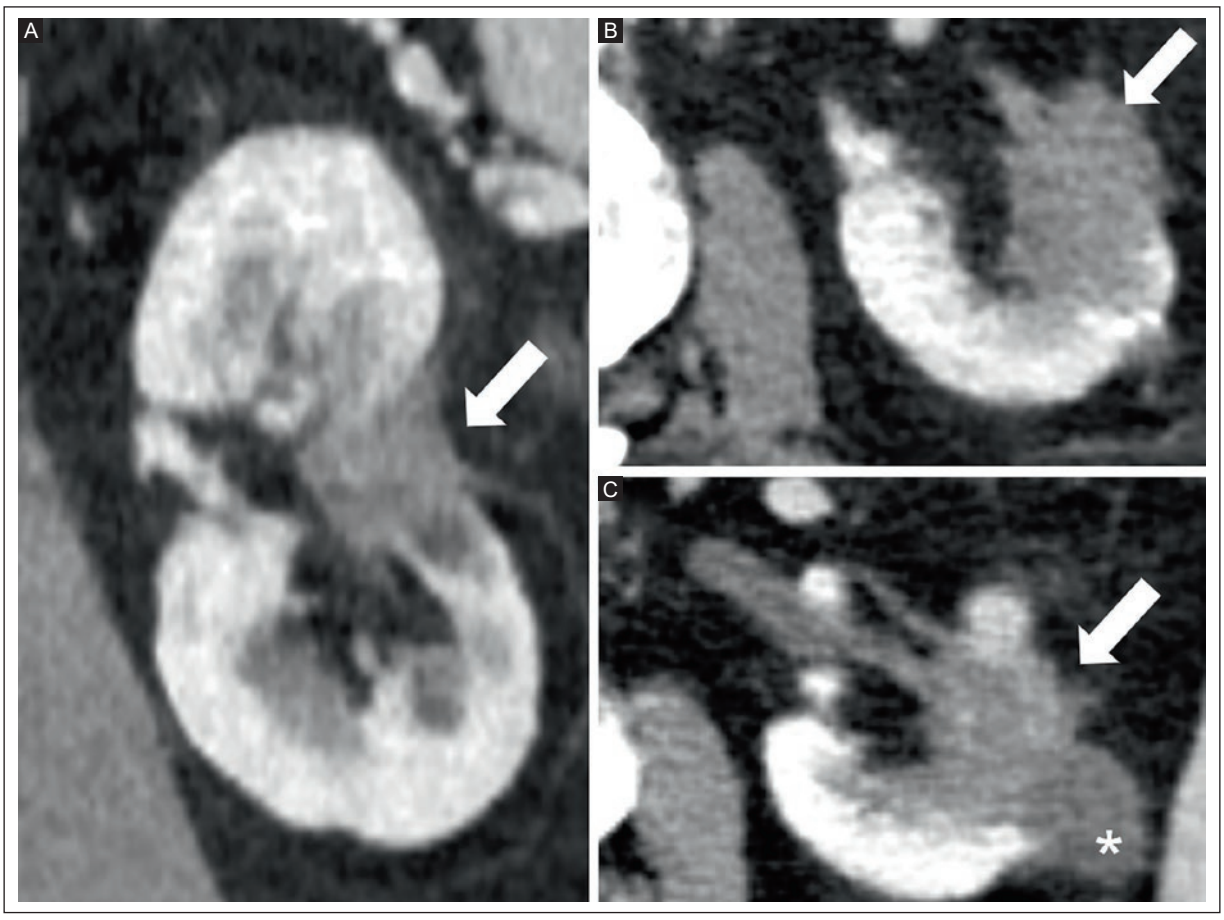

Figure 6. CT of a 78-year-old man diagnosed with metastatic UCC to the bone. **A:** coronal and **B:** axial planes show an infiltrative lesion with an ill-defined border, invading the renal cortex, medulla, renal sinus and calyces on nephrographic phase CT (arrows). **C:** the lesion (arrow) is associated with an adjacent cystic lesion (asterisk).

CT: computed tomography; UCC: urothelial cell carcinoma.

ALGORITHM AND MANAGEMENT

Based on the principal imaging features of the main solid renal lesions, we propose an algorithm for their assessment and diagnosis using multiparametric MRI aiming to guide radiologists (Figure 7). The same enhancement patterns can be applied to CEUS and multiphasic contrast-enhanced CT. Some challenges remain for radiologists. Distinguishing oncocytoma from chromophobe or clear cell RCC may be limited or impossible. However, studies have shown that these entities have significantly different ADC values[20,21]. Further research is needed to determine specific and characteristic absolute ADC values. Another challenge is differentiating lipid-poor AML from papRCC. These lesions have different contrast enhancement profiles: papRCC shows mild, progressive enhancement, while lipid-poor AML demonstrates early intense enhancement followed by rapid washout[14,52,74]. Quantitative measures have been developed to assess enhancement kinetics[14,89,90]. However, they require validation in larger, prospective studies.

In this context, the clear cell likelihood score (ccLS) has been proposed to provide a standardized approach for assessing the probability that a renal mass smaller than 4 cm is a ccRCC on mpMRI[2,91]. It is presented as a 5-point Likert-scale ('very unlikely' to 'very likely') and helps suggest differential diagnoses for ccRCC. The ccLS has demonstrated satisfactory diagnostic performance and appears to avoid unnecessary surgical treatment for benign lesions. However, further studies are recommended for its multi-institutional validation[91].

In addition, the development of radiomics and machine learning techniques may improve the noninvasive characterization of renal lesions and enhance the diagnostic performance of imaging modalities. After the radiological diagnosis of a renal lesion, management should be

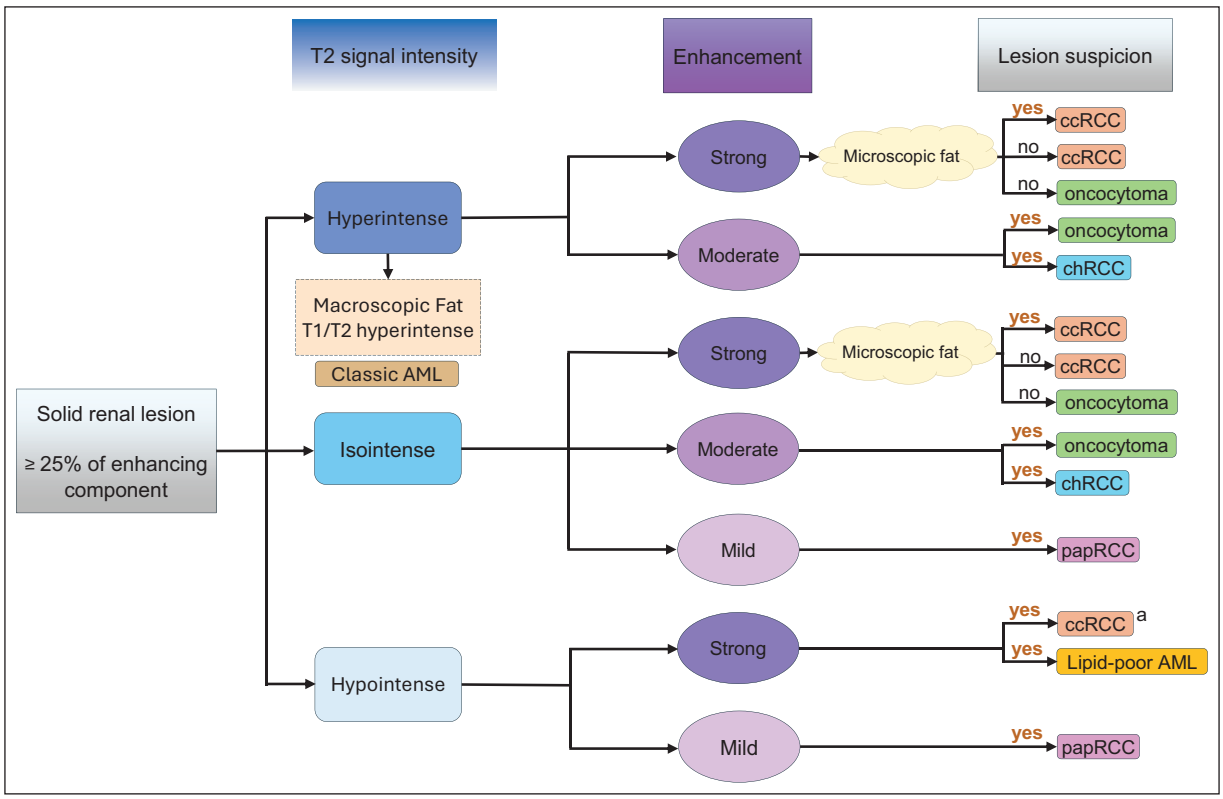

Figure 7. Algorithm for solid renal lesion assessment and diagnosis on multiparametric MRI based on the clear cell likelihood score by Pedrosa et al.[91].

[a]If heterogeneous. MRI: magnetic resonance imaging.

guided by several parameters: age, comorbidities, life expectancy, psychological factors, and lesion extension in the case of a suspicious lesion[2]. A shared multidisciplinary decision-making approach is recommended[2]. Renal biopsy is the cornerstone for diagnosing indeterminate renal lesions. It is indicated before active surveillance, ablative treatment, and in the context of metastatic disease for optimal treatment decisions. Biopsy should be avoided in comorbid patients managed conservatively (watchful waiting) or in fit patients diagnosed with a renal mass requiring surgical treatment given the high diagnostic accuracy of imaging[2].

CONCLUSION

Contrast-enhanced CT and MRI have high diagnostic accuracy in characterizing focal renal lesions and play a key role in guiding further management of renal masses, which are often incidentally detected. In challenging cases, renal biopsy remains the gold standard. The development and validation of quantitative MRI parameters as well as radiomics and machine learning techniques may increase the diagnostic accuracy of noninvasive imaging, leading to optimal management decision.

Funding

The authors declare that they have not received funding.

Conflicts of interest

The authors declare no conflicts of interest.

Ethical considerations

Protection of humans and animals. The authors declare that no experiments involving humans or animals were conducted for this research.

Confidentiality, informed consent, and ethical approval. The study does not involve patient personal data nor requires ethical approval. The SAGER guidelines do not apply.

Declaration on the use of artificial intelligence. The authors declare that no generative artificial intelligence was used in the writing of this manuscript.

REFERENCES

1. Meyer HJ, Pfeil A, Schramm D, Bach AG, Surov A. Renal incidental findings on computed tomography: frequency and distribution in a large non selected cohort. Medicine (Baltimore). 2017;96(26):e7039. doi: 10.1097/MD.0000000000007039.
2. Bex A, Albiges L, Bedke J, Capitanio U, Dabestani M, Hora M, et al. EAU guidelines on renal cell carcinoma. European Association of Urology; 2025.
3. Silverman SG, Pedrosa I, Ellis JH, Hindman NM, Schieda N, Smith AD, et al. Bosniak classification of cystic renal masses, version 2019: an update proposal and needs assessment. Radiology. 2019;292(2):475-488. doi: 10.1148/radiol.2019182646.
4. Zbroja M, Kuczyńska M, Drelich K, Mikos E, Zarajczyk A, Cheda M, et al. Contrast-enhanced ultrasound in the diagnosis of solid renal lesions. J Clin Med. 2024;13(13):3821. doi: 10.3390/jcm13133821.
5. Furrer MA, Spycher SCJ, Büttiker SM, Gross T, Bosshard P, Thalmann GN, et al. Comparison of the diagnostic performance of contrast-enhanced ultrasound with that of contrast-enhanced computed tomography and contrast-enhanced magnetic resonance imaging in the evaluation of renal masses: a systematic review and meta-analysis. Eur Urol Oncol. 2020;3(4):464-473. doi: 10.1016/j.euo.2019.08.013.
6. Vogel C, Ziegelmüller B, Ljungberg B, Bensalah K, Bex A, Canfield S, et al. Imaging in suspected renal-cell carcinoma: systematic review. Clin Genitourin Cancer. 2019;17(2):e345-355. doi: 10.1016/j.clgc.2018.07.024.
7. Shinagare AB, Davenport MS, Park H, Pedrosa I, Remer EM, Chandarana H, et al. Lexicon for renal mass terms at CT and MRI: a consensus of the society of abdominal radiology disease-focused panel on renal cell carcinoma. Abdom Radiol. 2021;46(2):703-722. doi: 10.1007/s00261-020-02644-x.
8. Verma SK, Mitchell DG, Yang R, Roth CG, O'Kane P, Verma M, et al. Exophytic renal masses: angular interface with renal parenchyma for distinguishing benign from malignant lesions at MR imaging. Radiology. 2010;255(2):501-507. doi: 10.1148/radiol.09091109.
9. Herts BR, Silverman SG, Hindman NM, Uzzo RG, Hartman RP, Israel GM, et al. Management of the incidental renal mass on CT: a white paper of the ACR incidental findings committee. J Am Coll Radiol. 2018;15(2):264-273. doi: 10.1016/j.jacr.2017.04.028.
10. Dodelzon K, Mussi TC, Babb JS, Taneja SS, Rosenkrantz AB. Prediction of growth rate of solid renal masses: utility of mr imaging features—preliminary experience. Radiology. 2012;262(3):884-893. doi: 10.1148/radiol.11111074.
11. Chen L-S, Zhu Z-Q, Wang Z-T, Li J, Liang L-F, Jin J-Y, et al. Chemical shift magnetic resonance imaging for distinguishing minimal-fat renal angiomyolipoma from renal cell carcinoma: a meta-analysis. Eur Radiol. 2018;28(5):1854-1861. doi: 10.1007/s00330-017-5141-0.
12. De Silva S, Lockhart K, Aslan P, Nash P, Hutton A, Malouf D, et al. Chemical shift imaging in the identification of those renal tumours that contain microscopic fat and the utility of multiparametric MRI in their differentiation. J Med Imaging Radiat Oncol. 2020;64(6):762-768. doi: 10.1111/1754-9485.13082.
13. Karlo CA, Donati OF, Burger IA, Zheng J, Moskowitz CS, Hricak H, et al. MR imaging of renal cortical tumours: qualitative and quantitative chemical shift imaging parameters. Eur Radiol. 2013;23(6):1738-1744. doi: 10.1007/s00330-012-2758-x.
14. Vargas HA, Chaim J, Lefkowitz RA, Lakhman Y, Zheng J, Moskowitz CS, et al. Renal cortical tumors: use of multiphasic contrast-enhanced MR imaging to differentiate benign and malignant histologic subtypes. Radiology. 2012;264(3):779-788. doi: 10.1148/radiol.12110746.
15. Hötker AM, Mazaheri Y, Wibmer A, Karlo CA, Zheng J, Moskowitz CS, et al. Differentiation of clear cell renal cell carcinoma from other renal cortical tumors by use of a quantitative multiparametric MRI approach. Am J Roentgenol. 2017;208(3):W85-91. doi: 10.2214/AJR.16.16652.
16. Thoeny HC, De Keyzer F. Diffusion-weighted MR imaging of native and transplanted kidneys. Radiology. 2011;259(1):25-38. doi: 10.1148/radiol.10092419.
17. Taouli B, Thakur RK, Mannelli L, Babb JS, Kim S, Hecht EM, et al. Renal lesions: characterization with diffusion-weighted imaging versus contrast-enhanced MR imaging. Radiology. 2009;251(2):398-407. doi: 10.1148/radiol.2512080880.
18. Tordjman M, Mali R, Madelin G, Prabhu V, Kang SK. Diagnostic test accuracy of ADC values for identification of clear cell renal cell carcinoma: systematic review and meta-analysis. Eur Radiol. 2020;30(7):4023-4038. doi: 10.1007/s00330-020-06740-w.
19. Hötker AM, Mazaheri Y, Wibmer A, Zheng J, Moskowitz CS, Tickoo SK, et al. Use of DWI in the differentiation of renal cortical tumors. Am J Roentgenol. 2016;206 (1):100-105. doi: 10.2214/AJR.14.13923.
20. Akinci O, Turkoglu F, Nalbant MO, Inci E. Differentiating renal cell carcinoma and oncocytoma with volumetric MRI histogram analysis. North Clin Istanb. 2023;10(5):636-641. doi: 10.14744/nci.2023.26122.
21. Uchida Y, Yoshida S, Arita Y, Shimoda H, Kimura K, Yamada I, et al. Apparent diffusion coefficient map-based texture analysis for the differentiation of chromophobe renal cell carcinoma from renal oncocytoma. Diagnostics. 2022;12(4):817. doi: 10.3390/diagnostics12040817.
22. Metin M, Aydın H, Karaoğlanoğlu M. Renal cell carcinoma or oncocytoma? The contribution of diffusion-weighted magnetic resonance imaging to the differential diagnosis of renal masses. Medicina (Mex). 2022;58(2):221. doi: 10.3390/medicina58020221.
23. Serter A, Onur MR, Coban G, Yildiz P, Armagan A, Kocakoc E. The role of diffusion-weighted MRI and contrast-enhanced MRI for differentiation between solid renal masses and renal cell carcinoma subtypes. Abdom Radiol. 2021;46(3):1041-1052. doi: 10.1007/s00261-020-02742-w.
24. De Perrot T, Sadjo Zoua C, Glessgen CG, Botsikas D, Berchtold L, Salomir R, et al. Diffusion-weighted MRI in the genitourinary system. J Clin Med. 2022;11(7):1921. doi: 10.3390/jcm11071921.
25. Bellin M-F, Valente C, Bekdache O, Maxwell F, Balasa C, Savignac A, et al. Update on renal cell carcinoma diagnosis with novel imaging approaches. Cancers (Basels). 2024;16(10):1926. doi: 10.3390/cancers16101926.
26. Rockall AG, Allen B, Brown MJ, El-Diasty T, Fletcher J, Gerson RF, et al. Sustainability in Radiology: position paper and call to action. Radiology. 2025;314(3):e250325. doi: 10.1148/radiol.250325.
27. Verstraeten S, Ansems J, Ommen WV, Linden DVD, Looijmans F, Tesselaar E. Comparison of true non-contrast and virtual non-contrast images in the characterization of renal lesions using detector-based spectral CT. Br J Radiol. 2023;96(1149):20220157. doi: 10.1259/bjr.20220157.
28. Xiao JM, Hippe DS, Zecevic M, Zamora DA, Cai LM, Toia GV, et al. Virtual unenhanced dual-energy CT images obtained with a multimaterial decomposition algorithm: diagnostic value for renal mass and urinary stone evaluation. Radiology. 2021;298(3):611-619. doi: 10.1148/radiol.2021192448.
29. Bucolo GM, Ascenti V, Barbera S, Fontana F, Aricò FM, Piacentino F, et al. Virtual non-contrast spectral CT in renal masses: is it time to discard conventional unenhanced phase? J Clin Med. 2023;12(14):4718. doi: 10.3390/jcm12144718.
30. Chandarana H, Megibow AJ, Cohen BA, Srinivasan R, Kim D, Leidecker C, et al. Iodine quantification with dual-energy CT: phantom study and preliminary experience with renal masses. Am J Roentgenol. 2011;196(6):W693-700. doi: 10.2214/AJR.10.5541.
31. Graser A, Johnson TRC, Hecht EM, Becker CR, Leidecker C, Staehler M, et al. Dual-energy CT in patients suspected of having renal masses: can virtual nonenhanced images replace true nonenhanced images? Radiology. 2009;252(2):433-440. doi: 10.1148/radiol.2522080557.
32. Cao J, Lennartz S, Pisuchpen N, Mroueh N, Kongboonvijit S, Parakh A, et al. Renal lesion characterization by dual-layer dual-energy CT: comparison of virtual and true unenhanced images. Am J Roentgenol. 2022;219(4):614-623. doi: 10.2214/AJR.21.27272.
33. Kaza RK, Raff EA, Davenport MS, Khalatbari S. Variability of CT attenuation measurements in virtual unenhanced images generated using multimaterial decomposition from fast kilovoltage-switching dual-energy CT. Acad Radiol. 2017;24(3):365-372. doi: 10.1016/j.acra.2016.09.002.
34. Meyer M, Nelson RC, Vernuccio F, González F, Farjat AE, Patel BN, et al. Virtual unenhanced images at dual-energy CT: influence on renal lesion characterization. Radiology. 2019;291(2):381-390. doi: 10.1148/radiol.2019181100.
35. Lennartz S, Pisuchpen N, Parakh A, Cao J, Baliyan V, Sahani D, et al. Virtual unenhanced images: qualitative and quantitative comparison between different dual-energy CT Scanners in a patient and phantom study. Invest Radiol. 2022;57(1):52. doi: 10.1097/RLI.0000000000000802.
36. Salameh J-P, McInnes MDF, McGrath TA, Salameh G, Schieda N. Diagnostic Accuracy of dual-energy CT for evaluation of renal masses: systematic review and meta-analysis. Am J Roentgenol. 2019;212(4):W100-105. doi: 10.2214/AJR.18.20527.
37. Margono E, Qureshi MM, Gupta A. Iodine density threshold to distinguish between enhancing and nonenhancing renal lesions with dual-layer dual-energy CT. J Comput Assist Tomogr. 2025;49(1):50-56. doi: 10.1097/RCT.0000000000001651.
38. Thiravit S, Moleesaide A, Kaewlai R, Limsakol C, Maneegarn A, Phothisirisakulwong A, et al. Diagnostic accuracy of iodine quantification and material density imaging with rapid Kilovoltage-switching DECT for small hyperattenuating renal lesions. Abdom Radiol. 2025. Epub ahead of print. doi: 10.1007/s00261-025-04964-2.
39. Van Der Star S, De Jong PA, Kok M. Incidental indeterminate renal lesions: distinguishing non-enhancing from potential enhancing renal lesions using iodine quantification on portal venous dual-layer spectral CT. J Pers Med. 2023;13(11):1546. doi: 10.3390/jpm13111546.
40. Zhu Q, Sun J, Zhu W, Chen W, Ye J. Spectral CT imaging versus conventional CT post-processing technique in differentiating malignant and benign renal tumors. Br J Radiol. 2023;96(1151):20230147. doi: 10.1259/bjr.20230147.
41. Wang D, Huang X, Bai L, Zhang X, Wei J, Zhou J. Differential diagnosis of chromophobe renal cell carcinoma and papillary renal cell carcinoma with dual-energy spectral computed tomography. Acta Radiol. 2020;61(11):1562-1569. doi: 10.1177/0284185120903447.
42. Moch H, Amin MB, Berney DM, Compérat EM, Gill AJ, Hartmann A, et al. The 2022 World Health Organization Classification of Tumours of the Urinary System and Male Genital Organs—Part A: renal, penile, and testicular tumours. Eur Urol. 2022;82(5):458-468. doi: 10.1016/j.eururo.2022.06.016.

43. Almazedi B, Stubbs C. Renal angiomyolipoma: from imaging to intervention. Clin Radiol. 2024;79(1):25-32. doi: 10.1ss016/j.crad.2023.09.028.
44. Jinzaki M, Silverman SG, Akita H, Mikami S, Oya M. Diagnosis of renal angiomyolipomas: classic, fat-poor, and epithelioid types. Semin Ultrasound CT MRI. 2017;38(1):37-46. doi: 10.1053/j.sult.2016.11.001.
45. Burgan CM, Sanyal R, Lockhart ME. Ultrasound of renal masses. Radiol Clin North Am. 2019;57(3):585-600. doi: 10.1016/j.rcl.2019.01.009.
46. Woo S, Kim SY, Cho JY, Kim SH, Lee MS. Exophytic renal angiomyolipoma and perirenal liposarcoma: revisiting the role of CT for differential diagnosis. Acta Radiol. 2016;57(2):249-255. doi: 10.1177/0284185115574543.
47. Wang L-J, Wong Y-C, Chen C-J, See L-C. Computerized tomography characteristics that differentiate angiomyolipomas from liposarcomas in the perinephric space. J Urol. 2002;167 (2 Pt 1):490-493. doi: 10.1016/S0022-5347(01)69071-2.
48. Wang Q, Juan Y-H, Li Y, Xie J-J, Liu H, Huang H, et al. Multidetector computed tomography features in differentiating exophytic renal angiomyolipoma from retroperitoneal liposarcoma: a strobe-compliant observational study. Medicine (Baltimore). 2015;94(37):e1521 doi: 10.1097/MD.0000000000001521.
49. Lopes Vendrami C, Parada Villavicencio C, DeJulio TJ, Chatterjee A, Casalino DD, Horowitz JM, et al. Differentiation of solid renal tumors with multiparametric MR imaging. RadioGraphics. 2017;37(7):2026-2042. doi: 10.1148/rg.2017170039.
50. Farrell C, Noyes SL, Tourojman M, Lane BR. Renal Angiomyolipoma: Preoperative identification of atypical fat-poor AML. Curr Urol Rep. 2015;16(3):12. doi: 10.1007/s11934-015-0484-z.
51. Wilson MP, Patel D, Murad MH, McInnes MDF, Katlariwala P, Low G. Diagnostic performance of MRI in the detection of renal lipid-poor angiomyolipomas: a systematic review and meta-analysis. Radiology. 2020;296(3):511-520. doi: 10.1148/radiol.2020192070.
52. Wang D, Gong G, Fu Y, Zhu L, Yin H, Liu L, et al. CT imaging findings of renal epithelioid lipid-poor angiomyolipoma. Eur Radiol. 2022;32(7):4919-4930. doi: 10.1007/s00330-021-08528-y.
53. Ishigami K, Jones AR, Dahmoush L, Leite LV, Pakalniskis MG, Barloon TJ. Imaging spectrum of renal oncocytomas: a pictorial review with pathologic correlation. Insights Imaging. 2015;6(1):53-64. doi: 10.1007/s13244-014-0373-x.
54. Rosenkrantz AB, Hindman N, Fitzgerald EF, Niver BE, Melamed J, Babb JS. MRI features of renal oncocytoma and chromophobe renal cell carcinoma. Am J Roentgenol. 2010;195(6):W421-427. doi: 10.2214/AJR.10.4718.
55. Rosenkrantz AB, Hindman N, Fitzgerald EF, Niver BE, Melamed J, Babb JS. MRI features of renal oncocytoma and chromophobe renal cell carcinoma. Am J Roentgenol. 2010;195(6):W421-427. doi: 10.2214/AJR.10.4718.
56. Qu J, Zhang Q, Song X, Jiang H, Ma H, Li W, et al. CT differentiation of the oncocytoma and renal cell carcinoma based on peripheral tumor parenchyma and central hypodense area characterisation. BMC Med Imaging. 2023;23(1):16. doi: 10.1186/s12880-023-00972-0.
57. Woo S, Cho JY, Kim SH, Kim SY, Lee HJ, Hwang SI, et al. Segmental enhancement inversion of small renal oncocytoma: differences in prevalence according to tumor size. Am J Roentgenol. 2013;200(5):1054-1059. doi: 10.2214/AJR.12.9300.
58. Schieda N, McInnes MDF, Cao L. Diagnostic accuracy of segmental enhancement inversion for diagnosis of renal oncocytoma at biphasic contrast enhanced CT: systematic review. Eur Radiol. 2014;24(6):1421-1429. doi: 10.1007/s00330-014-3147-4.
59. Galmiche C, Bernhard J-C, Yacoub M, Ravaud A, Grenier N, Cornelis F. Is multiparametric MRI Useful for differentiating oncocytomas from chromophobe renal cell carcinomas? Am J Roentgenol. 2017;208(2):343-350. doi: 10.2214/AJR.16.16832.
60. Wang KL, Weinrach DM, Luan C, Han M, Lin F, Teh BT, et al. Renal papillary adenoma—a putative precursor of papillary renal cell carcinoma. Hum Pathol. 2007;38(2):239-246. doi: 10.1016/j.humpath.2006.07.016.
61. Calió A, Warfel KA, Eble JN. Papillary adenomas and other small epithelial tumors in the kidney: an autopsy study. Am J Surg Pathol. 2019;43(2):277-287. doi: 10.1097/PAS.0000000000001189.
62. Prasad SR, Surabhi VR, Menias CO, Raut AA, Chintapalli KN. Benign renal neoplasms in adults: cross-sectional imaging findings. Am J Roentgenol. 2008;190(1):158-164. doi:10.2214/AJR.07.2724.
63. Chou Y-C, Lee W-Y, Huang SK, Wu R-H, Kuo Y-T. Ten-year follow-up of renal adenomatosis with magnetic resonance imaging: a case report. J Med Case Reports. 2022;16(1):168. doi: 10.1186/s13256-022-03394-8.
64. Jiang T, Li W, Lin D, Wang J, Liu F, Ding Z. Imaging features of metanephric adenoma and their pathological correlation. Clin Radiol. 2019;74(5):408.e9-408.e17. doi: 10.1016/j.crad.2019.01.013.
65. Hayes AG, Stowasser M, Umapathysivam MM, Falhammar H, Torpy DJ. Approach to the patient: reninoma. J Clin Endocrinol Metab. 2024;109(2):e809-816. doi: 10.1210/clinem/dgad516.
66. Katabathina VS, Vikram R, Nagar AM, Tamboli P, Menias CO, Prasad SR. Mesenchymal neoplasms of the kidney in adults: imaging spectrum with radiologic-pathologic correlation. RadioGraphics. 2010;30(6):1525-1540. doi: 10.1148/rg.306105517.
67. Wang L, Li M, Jin S, Ouyang Y, Wang F, Lv K, et al. How to identify juxtaglomerular cell tumor by ultrasound: a case series and review of the literature. BMC Med Imaging. 2024;24(1):46. doi: 10.1186/s12880-024-01220-9.
68. Faucon A-L, Bourillon C, Grataloup C, Baron S, Bernadet-Monrozies P, Vidal-Petiot E, et al. Usefulness of magnetic resonance imaging in the diagnosis of juxtaglomerular cell tumors: a report of 10 cases and review of the literature. Am J Kidney Dis. 2019;73(4):566-571. doi: 10.1053/j.ajkd.2018.09.005.
69. Bazzi WM, Huang H, Al-Ahmadie H, Russo P. Clinicopathologic features of renomedullary interstitial cell tumor presenting as the main solid renal mass. Urology. 2014;83(5):1104-1106. doi: 10.1016/j.urology.2014.01.008.
70. Lu Z, Al-Obaidy K, Cheng L, Perry KD, Grignon DJ, Williamson SR. Immunohistochemical characteristics of renomedullary interstitial cell tumor: a study of 41 tumors with emphasis on differential diagnosis of mesenchymal neoplasms. Hum Pathol. 2018;82:46-50. doi: 10.1016/j.humpath.2018.07.010.
71. Yamamoto K, Kawabata S, Kurisu Y, Inamoto T, Yamamoto K, Osuga K. A case of renomedullary interstitial cell tumor: radiologic-pathologic correlation. Radiol Case Rep. 2023;18(12):4574-4579. doi: 10.1016/j.radcr.2023.09.072.
72. Derchi LE, Grenier N, Heinz-Peer G, Dogra V, Franco F, Rollandi GA, et al. Imaging of renal leiomyomas. Acta Radiol. 2008;49(7):833-838. doi: 10.1080/02841850802087228.
73. Marko J, Craig R, Nguyen A, Udager AM, Wolfman DJ. Chromophobe Renal cell carcinoma with radiologic-pathologic correlation. RadioGraphics. 2021;41(5):1408-1419. doi: 10.1148/rg.2021200206.
74. Muglia VF, Prando A. Renal cell carcinoma: histological classification and correlation with imaging findings. Radiol Bras. 2015;48(3):166-174. doi: 10.1590/0100-3984.2013.1927.
75. Iacovelli R, Modica D, Palazzo A, Trenta P, Piesco G, Cortesi E. Clinical outcome and prognostic factors in renal medullary carcinoma. A pooled analysis from 18 years of medical literature. Can Urol Assoc J. 2015;9(3-4):E172-177. doi: 10.5489/cuaj.2373.
76. Greco F, Faiella E, Santucci D, Augusto Mallio C, Nezzo M, Quattrocchi CC, et al. Imaging of renal medullary carcinoma. J Kidney Cancer VHL. 2017;4(1):1-7. doi: 10.15586/jkcvhl.2017.62.
77. Blitman NM, Berkenblit RG, Rozenblit AM, Levin TL. Renal medullary carcinoma: CT and MRI features. Am J Roentgenol. 2005;185(1):268-272. doi: 10.2214/ajr.185.1.01850268.
78. Sweet DE, Ward RD, Wang Y, Tanaka H, Campbell SC, Remer EM. Infiltrative renal malignancies: imaging features, prognostic implications, and mimics. RadioGraphics. 2021;41(2):487-508. doi: 10.1148/rg.2021200123.
79. Ciszewski S, Jakimów A, Smolska-Ciszewska B. Collecting (Bellini) duct carcinoma: a clinical study of a rare tumour and review of the literature. Can Urol Assoc J. 2015;9(9-10):e589-593. doi: 10.5489/cuaj.2932.
80. Chen J, Cai D, Gong K, Zhu S. Collecting duct carcinoma of the kidney: analysis of 74 cases from multiple centers. Urology. 2022;164:163-168. doi: 10.1016/j.urology.2022.01.032.
81. Suarez C, Marmolejo D, Valdivia A, Morales-Barrera R, Gonzalez M, Mateo J, et al. Update in collecting duct carcinoma: current aspects of the clinical and molecular characterization of an orphan disease. Front Oncol. 2022;12:970199. doi: 10.3389/fonc.2022.970199.
82. Young JR, Young JA, Margolis DJA, Sauk S, Sayre J, Pantuck AJ, et al. Sarcomatoid renal cell carcinoma and collecting duct carcinoma. Acad Radiol. 2017;24(10):1226-1232. doi: 10.1016/j.acra.2017.03.017.
83. Lyu Z, Liu L, Li H, Wang H, Liu Q, Chen T, et al. Imaging analysis of 13 rare cases of renal collecting (Bellini) duct carcinoma in northern China: a case series and literature review. BMC Med Imaging. 2021;21(1):42. doi: 10.1186/s12880-021-00574-8.
84. Fenelon SS, Santos JMMM, Faraj SF, Mattedi RL, Trpkov K, Nahas WC, et al. Eosinophilic Solid and Cystic Renal Cell Carcinoma: Imaging Features of a Novel neoplasm. Urology. 2018;114:e9-e10. doi: 10.1016/j.urology.2018. 01.020.
85. Yu H, Xiang H, Zhang W, Wang S. Eosinophilic solid and cystic renal cell carcinoma: a case report of a novel type neoplasm. Discov Med. 2025;2(1):41. doi: 10.1007/s44337-025-00215-x.
86. Fu S, Chen D, Zhang Y, Wei Y, Pan Y. CT-based scoring system for diagnosing eosinophilic solid and cystic renal cell carcinoma versus clear cell renal cell carcinoma. Sci Rep. 2025;15(1):2736. doi: 10.1038/s41598-025-86932-w.
87. Browne RFJ, Meehan CP, Colville J, Power R, Torreggiani WC. Transitional Cell carcinoma of the upper urinary tract: spectrum of imaging findings. RadioGraphics. 2005;25(6):1609-1627. doi: 10.1148/rg.256045517.
88. Liang K, Yuan Y, Lv B, Ke Z. Primary squamous cell carcinoma of renal parenchyma: a case report and literature review. Front Oncol. 2023;13:1037156. doi: 10.3389/fonc.2023.1037156.
89. Hötker AM, Mazaheri Y, Wibmer A, Karlo CA, Zheng J, Moskowitz CS, et al. Differentiation of clear cell renal cell carcinoma from other renal cortical tumors by use of a quantitative multiparametric MRI approach. Am J Roentgenol. 2017;208(3):W85-91. doi: 10.2214/AJR.16.16652.
90. Sasiwimonphan K, Takahashi N, Leibovich BC, Carter RE, Atwell TD, Kawashima A. Small (< 4 cm) renal mass: differentiation of angiomyolipoma without visible fat from renal cell carcinoma utilizing MR imaging. Radiology. 2012;263(1):160-168. doi:10.1148/radiol.12111205. Erratum in: Radiology. 2016;280(2):653. doi: 10.1148/radiol.2016164024.
91. Pedrosa I, Cadeddu JA. How we do it: managing the indeterminate renal mass with the MRI clear cell likelihood score. Radiology. 2022;302(2):256-269. doi: 10.1148/radiol.210034.

JMeXFRI

Journal of the Mexican Federation of Radiology and Imaging

Check for updates

FULL RESEARCH ARTICLE

Standing knee US versus knee MRI for evaluating medial meniscal extrusion

*I.F. Alejandro Lopez-Beltran and Osiris G. Salazar-Lopez**

Department of Radiology and Imaging, Hospital de Especialidades Num. 2, Unidad Medica de Alta Especialidad, Centro Medico Nacional del Noroeste "Lic. Luis Donaldo Colosio Murrieta", Instituto Mexicano del Seguro Social, Ciudad Obregon, Sonora, Mexico

ABSTRACT

Introduction: *A weight-bearing (WB) knee ultrasound (US) represents a conceptual shift from static morphological to functional assessment. This study aimed to compare the ability of magnetic resonance imaging (MRI), non-weight-bearing US (NWB-US), and WB-US for diagnosing medial meniscal extrusion and to determine the prevalence of minor and major extrusion grades.* **Material and methods:** *Findings were categorized as normal medial meniscus, minor, and major medial meniscal extrusion. Cochran's Q test and McNemar's test with Holm-Bonferroni correction were used for statistical analyses.* **Results:** *This study included 50 adult patients (14 women and 36 men, mean age 37.8 ± 10.1 years) with knee pain. MRI classified more knees as normal (n = 40, 80.0%) compared to NWB-US (n = 20, 40.0%) and WB-US (n = 7, 14.0%) (p < 0.001). WB-US identified minor (n = 20, 40.0%) and major (n = 23, 46.0%, p < 0.001) medial meniscal extrusion more frequently. NWB-US identified 17 (34.0%) minor and 13 (26.0%) major cases. MRI identified 4 (8.0%) and 6 (12.0%) minor and major medial cases, respectively. There was a trend toward greater medial meniscal extrusion with increasing patient age across all three imaging methods. The effect of BMI depended on the imaging modality: extrusion frequency increased with MRI and WB-US as BMI increased, while medial meniscal extrusion decreased with increasing BMI in NWB-US.* **Conclusion:** *WB-US was more useful than MRI and NWB-US for diagnosing minor and major grades of medial meniscal extrusion. Increasing age was the most significant factor, with BMI affecting results depending on the imaging modality used.*

Keywords: *Meniscal. Weight-bearing. Ultrasound. Magnetic Resonance Imaging.*

INTRODUCTION

Meniscal extrusion has recently been recognized as a hallmark of meniscus dysfunction. The medial meniscus covers 50-75% of the medial tibial plateau and is attached circumferentially to the capsule[1]. Meniscal extrusion compromises the weight-bearing surface area and predisposes the knee to injury. It can manifest as osteoarthritis, osteophytosis, chondral lesions, further meniscal tearing, and cartilage loss[1]. Meniscal extrusion is the displacement of the meniscus, ranging from a minimal physiologic extrusion to more than 10 mm^2. Knee magnetic resonance imaging (MRI) focuses predominantly on structural anatomy at rest[1,3]. However, its accuracy in detecting medial meniscal extrusion under static, non-weight-bearing conditions is limited[4-6] due to the dynamic nature of meniscal biomechanics, which are subject to axial and rotational forces during weight-bearing[4-8].

Ultrasound (US) is a modality that allows multiplanar and dynamic imaging of the meniscus and other knee structures. It has excellent sensitivity and specificity in detecting extrusion, along with reliable quantitative

***Corresponding author:**
Osiris G. Salazar-Lopez
E-mail: osiris.salazar@gmail.com

Received for publication: 13-07-2025
Accepted for publication: 18-09-2025
DOI: 10.24875/JMEXFRI.M25000115

Available online: 15-01-2026
J Mex Fed Radiol Imaging. 2025;4(4):233-242
www.JMeXFRI.com

extrusion assessment[5,9] US evaluation can be performed in two ways: non-weight-bearing (NWB-US) with the patient supine or weight-bearing (WB-US) with the patient standing, allowing evaluation under axial loading on the examined extremity[10].

Medial meniscal extrusion is a marker of biomechanical alteration in the knee, with prognostic implications and potential utility in identifying patients at risk of developing or progressing to osteoarthritis[8]. Meniscal extrusion, a radial displacement of the meniscus greater than 3 mm, leads to altered knee biomechanics and accelerated knee joint degeneration[1]. It is graded as minor (2-3 mm) or major (> 3 mm), but reference values have not been standardized[3,7]. Static assessment in the supine position does not adequately reflect the magnitude of medial meniscal extrusion[6], and the usefulness of WB-US has not been sufficiently studied[5,8-13]. This study compared the ability of MRI, NWB-US, and WB-US to diagnose medial meniscal extrusion and determined the prevalence of minor and major medial meniscal extrusion.

MATERIAL AND METHODS

This cross-sectional study was conducted from June 2024 to January 2025 at the Department of Radiology and Imaging, Hospital de Especialidades No. 2, "Lic. Luis Donaldo Colosio Murrieta," Centro Medico Nacional del Noroeste del Instituto Mexicano del Seguro Social in Ciudad Obregon, Sonora, Mexico. Adult patients aged 18 years or older with knee pain referred by orthopedic physicians were consecutively enrolled. Patients were excluded if they had limitations for dynamic assessment in the standing position, a history of knee surgery, knee fractures, knee soft-tissue infections, obesity that prevented the use of the knee coil, or incomplete MRI examination. All participants provided informed consent. The research ethics committee and the research committee approved the study protocol.

Study design and variables

Age, sex, weight, height, body mass index (BMI), and the presence of posterior root tear were recorded. Patients were grouped based on MRI, NWB-US, and WB-US findings into normal medial meniscus examination, minor medial meniscal extrusion, and major medial meniscal extrusion according to Costa et al.[3]

Definitions

NWB-US[10]: imaging modality that evaluates knee structures with the patient supine with complete knee extension.

WB-US[10]: imaging modality that evaluates knee structures with the patient in a standing weight-bearing position with axial loading.

Medial meniscal extrusion: partial or complete displacement of the meniscus beyond the medial tibial plateau.

Minor medial meniscal extrusion[3]: partial or complete displacement of the meniscus beyond the medial tibial plateau greater than 2 mm but less than 3 mm.

Major medial meniscal extrusion[3]: partial or complete displacement of the meniscus greater than 3 mm.

Posterior root tear[13]: avulsion injury or radial tear occurring 10 mm of the posterior meniscal root bony attachment.

Imaging acquisition and analysis protocol

Knee MRI

MRI was performed on a Skyra 3.0T scanner (Siemens Healthineers, Erlangen, Germany) with high-resolution images. The imaging protocol used the Siemens Quiet Suite[14] in the axial, coronal, and sagittal planes. It included the following turbo spin-echo (TSE) sequences: proton density (PD)-weighted time repetition (TR)/time echo (TE) (3600/39 ms), fat-saturated PD-weighted (TR/TE, 4150/29 ms), and fat-saturated T2-weighted (TR/TE, 4200/63 ms).

Medial meniscal extrusion was measured as the distance from a horizontal line, extending from the outer margin of the medial meniscus to its intersection with a vertical line. Measurements were performed by drawing a vertical line through the peripheral margin of the medial tibial plateau and the medial femoral condyle. Osteophytes were not considered in determining the medial femoral or tibial cortical margin[3]. A radiologist with 15 years of experience (OSL) analyzed the MRI images.

Knee NWB-US and knee WB-US

Real-time grayscale US was performed with a GE LOGIQ F6 (General Electric HealthCare, Chicago, IL, USA) using a 7-13 MHz linear transducer.

NWB-US: involved scanning the medial meniscus with the patient supine and the knee joint fully extended, using the medial collateral ligament as an anatomical landmark.

WB-US: involved scanning the medial meniscus in the standing position with the knee fully extended, placing the transducer over the medial femoral and tibial

cortical contours, using the medial collateral ligament as an anatomical reference[10].

A fourth-year radiology resident performed imaging examinations under the supervision of a radiologist (OSL) with 15 years of experience.

Statistical analysis

Univariate analysis with measures of central tendency and dispersion was performed for quantitative variables. Frequencies and percentages were evaluated for qualitative variables. Because medial meniscal extrusion measurements did not follow a normal distribution, the Friedman test was used. The Nemenyi post hot test was applied to statistically significant results[15]. The Friedman test was used to compare the three imaging modalities in three categories (normal meniscus, minor medial meniscal extrusion, or major medial meniscal extrusion). The Wilcoxon test with the Holm-Bonferroni correction was used to identify statistically significant differences. To compare normal medial meniscus findings with minor and major extrusion across imaging methods, Cochran's Q test was used. McNemar's test with Holm-Bonferroni correction was used for statistically significant comparisons[16-18]. Confounding variables were identified using linear mixed models. The correlation between medial meniscal extrusion with posterior root tear was assessed with Kendall's tau test. Analyses were performed using the statistical platform R (R Core Team, 2023, Vienna, Austria) and RStudio (Posit Team, 2023, Boston, MA, USA).

RESULTS

Fifty-four patients with knee pain were evaluated. One patient with a history of knee surgery, one obese patient with limitations preventing use of the knee antenna, and two patients with incomplete MRI studies were excluded. Fifty knees in 50 patients, including 14 women and 36 men with a mean age of 37.8 ± 10.1 years (range, 25-62), were assessed (Table 1). Posterior root tear was an infrequent finding, identified in only 4 (8.0%) of 50 patients.

Medial meniscal extrusion measurements by MRI, NWB-US, and WB-US

Figure 1 shows a box plot comparing MRI, NWB-US, and WB-US measurements of medial meniscal extrusion. Medial meniscal extrusion by WB-US exhibited higher values (median 2.9 mm; interquartile range – IQR, 2.2-3.6 mm) compared to NWB-US (median 2.1 mm; IQR 1.2-3 mm), and MRI (median 1.0 mm; IQR 0.0-1.8 mm).

Table 1. Patient characteristics in the assessment of medial meniscal extrusion with and without posterior root tear

Description	(n = 50)
Age, years, mean ± SD (min-max)	37.8 ± 10.1 (25.0-62.0)
Sex, n (%)	
Women	14 (28.0)
Men	36 (72.0)
Weight (kg), mean ± SD (min-max)	89.4 ± 20.4 (52.0-160.0)
BMI, mean ± SD (min-max)	29.1 ± 4.8 (17.9-39.7)
Posterior root tear, n (%)	
Yes	4 (8.0)
No	46 (92.0)

BMI: body mass index; SD: standard deviation.

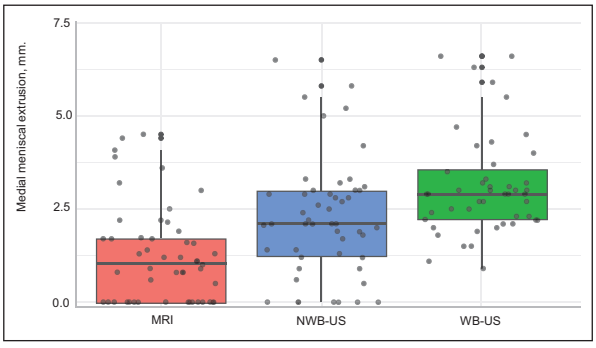

Figure 1. Box plot comparing medial meniscal extrusion measurements obtained by MRI, NWB-US, and WB-US. Medial meniscal extrusion measured by WB-US was significantly higher (median 2.9 mm; IQR 2.2-3.6 mm) compared to NWB-US (median 2.1 mm; IQR 1.2-3 mm) and MRI (median 1.0 mm; IQR 0.0-1.8 mm). Two 9.4 mm outliers, both assessed by WB-US, are not shown.

MRI: magnetic resonance imaging; NWB-US: non-weight-bearing ultrasound; WB-US: weight-bearing ultrasound; IQR: interquartile range.

Statistically significant differences were identified among the three medial meniscal extrusion ($p < 0.001$) measuring methods (Table 2). Medial meniscal extrusion was higher when assessed using WB-US than NWB-US or MRI. Post-hoc analysis showed that all pairwise comparisons between the imaging methods were significant. Comparisons involving WB-US versus NWB-US and versus MRI had greater statistical significance.

Comparison of MRI, NWB-US, and WB-US findings with normal medial meniscus and minor and major medial meniscal extrusion

MRI classified more knees as normal medial meniscus (n = 40, 80.0%) than NWB-US (n = 20, 40.0%) and

Table 2. Comparison of medial meniscal extrusion between MRI, NWB-US, and WB-US

Description	Nemenyi statistic	p
NWB-US vs. MRI	4.8	0.002
WB-US vs. MRI	12.79	< 0.001
WB-US vs. NWB-US	7.99	< 0.001

MRI: magnetic resonance imaging; NWB-US: non-weight-bearing ultrasound; WB-US: weight-bearing ultrasound.

WB-US (n = 7, 14.0%) (p < 0.001) (Table 3). WB-US identified minor and major medial meniscal extrusion more frequently (n = 20, 40.0%: p = 0.495 and n = 23, 46.0%: p < 0.001, respectively), while NWB-US identified 17 (34.0%) and 13 (26.0%) minor and major cases, respectively. MRI identified minor and major medial meniscal extrusion in 4 (8.0%) and 6 (12.0%) cases, respectively.

Pairwise comparison of medial meniscal extrusion grading

The pairwise comparison showed that MRI identified more patients with a normal medial meniscus than NWB-US (10/1) (p < 0.032) and WB-US (16/0) (p < 0.001) (Table 4). NWB-US also detected more normal knee examinations than WB-US (7/0) (p < 0.032). Statistically significant differences in major medial meniscal extrusion were observed among the three imaging methods. NWB-US and WB-US identified more cases of major medial meniscal extrusion than MRI (0/4) (p = 0.134) and 0/13 (p < 0.001), respectively. In contrast, minor meniscal extrusion showed concordance among the three imaging methods.

Analysis of variance of confounding variables and their interaction with imaging modality

Age was significantly associated with medial meniscal extrusion (Table 5). There was a trend toward greater medial meniscal extrusion with increasing patient age across all three imaging methods (Figure 2A). BMI had significantly more interaction depending on the imaging modality used. Extrusion increased with MRI and WB-US as BMI increased. In contrast, medial meniscal extrusion decreased with increasing BMI in NWB-US (Figure 2B). There was no significant association with sex, weight, or height.

Figure 3 shows images of a 39-year-old woman with normal weight and knee pain. MRI with fat suppression shows a 2.0 mm minor medial meniscal extrusion, and NWB-US a 2.6 mm minor medial meniscal extrusion. In contrast, WB-US shows a major 3.3 mm medial meniscal extrusion. Figure 4 shows images of a 58-year-old obese man with right knee pain. MRI with fat suppression shows a minor 2.8 mm medial meniscal extrusion, and NWB-US shows a major 3.7 mm medial meniscal extrusion. In contrast, WB-US shows a 4.6 mm major medial meniscal extrusion.

Figure 5 shows images of an obese woman with knee pain. MRI with fat suppression shows a 2.8 mm minor medial meniscal extrusion, NWB-US a 3.3 mm major medial meniscal extrusion, and WB-US a 4.5 mm major medial meniscal extrusion. Figure 6 shows images of a 48-year-old obese man with knee pain. MRI with fat suppression shows a 3.5 mm major medial meniscal extrusion, and NWB-US a 4.1 mm major medial meniscal extrusion. In contrast, WB-US shows a 4.6 mm major medial meniscal extrusion.

These cases illustrate that WB-US shows greater medial meniscal extrusion than MRI or NWB-US, underscoring the importance of mechanical loading conditions for more accurate evaluation of medial meniscal extrusion.

DISCUSSION

Our study showed that WB-US detects medial meniscal extrusion at both minor and major grades more frequently than NWB-US and MRI. WB-US is useful for real-time dynamic assessment and more accurately assesses meniscal biomechanics under physiological loading conditions.

Medial meniscal extrusion increases significantly under weight-bearing conditions[2]. Therefore, static evaluation may underestimate the diagnosis of medial meniscal extrusion[19]. WB-US is a useful tool for detecting medial meniscal extrusion under load[1,5,20]. The review by Papalia et al.[6] synthesizes evidence from multiple studies using various imaging modalities, such as MRI and dynamic WB-US, and introduces the key concept of “dynamic extrusion.” They concluded that US allows an accurate dynamic assessment of meniscal extrusion. Boksh et al.[10], in a systematic review of 31 studies assessing 3,747 knees, compared NWB-US and WB-US with MRI as the reference standard for measuring medial meniscal extrusion. WB-US consistently and significantly detected more knees with meniscal extrusion compared to NWB-US. WB-US identified medial

Table 3. Comparison of MRI, NWB-US, and WB-US findings for normal medial meniscus, minor, and major medial meniscal extrusion

Description	MRI (n = 50)	NWB-US (n = 50)	WB-US (n = 50)	p
Normal, n (%)	40 (80.0)	20 (40.0)	7 (14.0)	< 0.001
Minor medial meniscal extrusion, n (%)	4 (8.0)	17 (34.0)	20 (40.0)	0.495
Major medial meniscal extrusion, n (%)	6 (12.0)	13 (26.0)	23 (46.0)	< 0.001

MRI: magnetic resonance imaging; NWB-US: non-weight-bearing ultrasound; WB-US: weight-bearing ultrasound.

Table 4. Pairwise comparison of medial meniscal extrusion grading between MRI, NWB-US, and WB-US

Description	Comparison	Discordant pairs[a] (A = 1, B = 0/A = 0, B = 1)	p	Holm-adjusted p
Normal examination	Global test (Cochran's Q)	-	< 0.001	-
	MRI vs NWB-US[b], n	10/1	0.016	0.032
	MRI vs WB-US[b], n	16/0	< 0.001	< 0.001
	NWB-US vs WB-US[b], n	7/0	0.023	0.032
Minor meniscal extrusion	Global test (Cochran's Q)	-	0.495	-
Major meniscal extrusion	Global test (Cochran's Q)	-	< 0.001	-
	MRI vs NWB-US[b], n	0/4	0.134	0.134
	MRI vs WB-US[b], n	0/13	< 0.001	0.003
	NWB-US vs WB-US[b], n	0/9	0.008	0.015

[a]Discordant pairs are shown as (A = 1, B = 0/A = 0, B = 1) where A and B are the first and second image measurement methods named in the comparison; [b]pairwise tests are McNemar with continuity correction; Holm adjustment was applied within each category. MRI: magnetic resonance imaging; NWB-US: non-weight-bearing ultrasound; WB-US: weight-bearing ultrasound.

Table 5. Analysis of variance of confounding variables and their interaction with each imaging modality in patients with medial meniscal extrusion

Description	Degrees of freedom[a,b]	p	Significance
Age	1,44	< 0.001	Highly significant
Sex	1,44	0.759	Not significant
Weight	1,44	0.492	Not significant
Height	1,44	0.127	Not significant
BMI	1,44	0.630	Not significant
MRI, NWB-US, WB-US × Age	2,88	0.151	Not significant
MRI, NWB-US, WB-US × Sex	2,88	0.089	Trend toward significance
MRI, NWB-US, WB-US × Weight	2,88	0.059	Trend toward significance
MRI, NWB-US, WB-US × Height	2,88	0.366	Not significant
MRI, NWB-US, WB-US × BMI	2,88	0.011	Significant

[a]Numerator degrees of freedom. [b]Denominator degrees of freedom. MRI: magnetic resonance imaging; NWB-US: non-weight-bearing ultrasound; WB-US: weight-bearing ultrasound; BMI: body mass index.

meniscal extrusion when conventional supine MRI did not. In an experimental study in human cadavers, pressure sensors on a 3D scanning system were used in 10 knees with and without an axial force of 1,000 Newtons. Tibiofemoral contact mechanics and medial meniscal extrusion were quantified. The magnitude of meniscal extrusion significantly increased when the knee was flexed to 90° and loaded, compared with conventional measurements with the knee extended and unloaded[19]. Patel et al.[2] in a study of 143 subjects performed MRI with no load (supine) and with an axial load (simulating standing) and demonstrated that medial meniscal

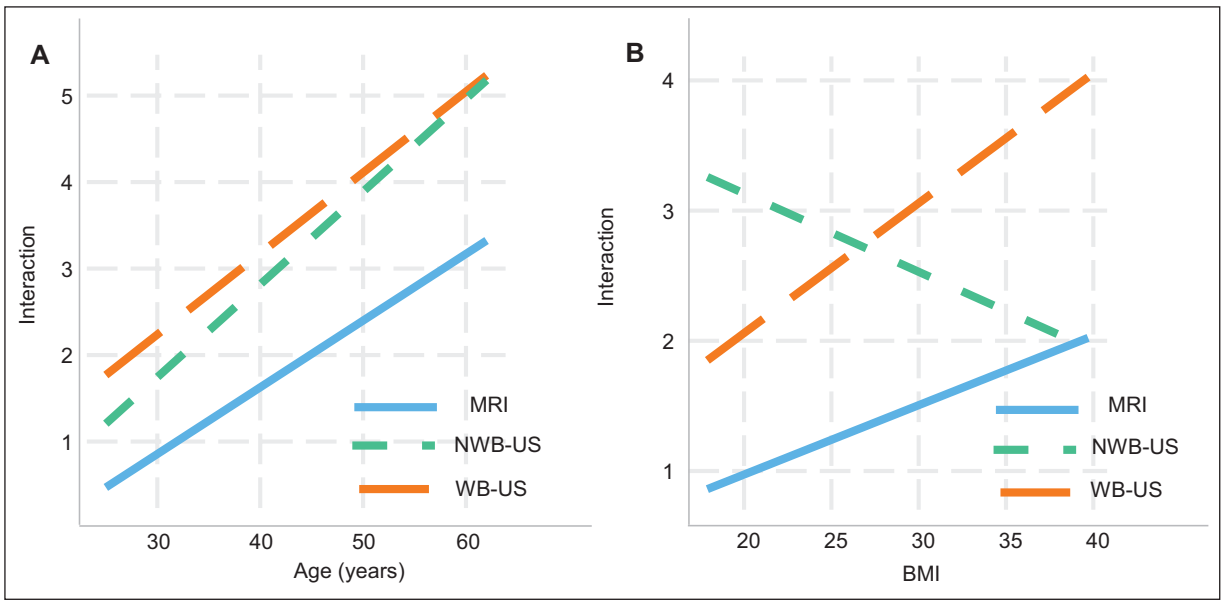

Figure 2. Interaction between imaging modalities and age and BMI. **A:** there is a trend toward greater medial meniscal extrusion as patient age increases with all three methods. **B:** extrusion increases with MRI and WB-US as BMI increases. In contrast, extrusion decreases with increasing BMI in NWB-US.

MRI: magnetic resonance imaging; NWB-US: non-weight-bearing ultrasound; WB-US: weight-bearing ultrasound.

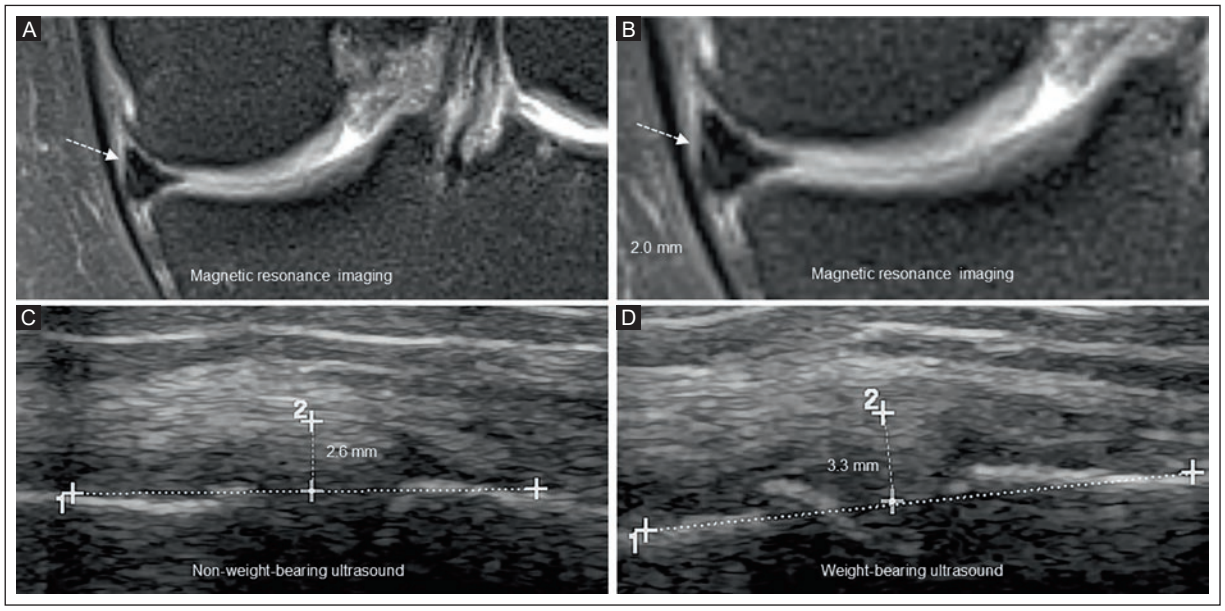

Figure 3. Comparison between imaging modalities in detecting medial meniscal extrusion in a 39-year-old woman with normal weight (BMI 24.2 kg/m²) and knee pain. **A-B:** coronal proton density-weighted MRI with fat suppression shows minor medial meniscal extrusion of 2.0 mm (arrows). **C:** NWB-US shows minor medial meniscal extrusion of 2.6 mm. **D:** WB-US shows major medial meniscal extrusion of 3.3 mm. WB-US highlights the ability to assess meniscal biomechanical responses to loading.

MRI: magnetic resonance imaging; NWB-US: non-weight-bearing ultrasound; WB-US: weight-bearing ultrasound.

extrusion increased significantly with a load (from 1.0 mm to 1.8 mm on average; $p < 0.001$). In our study, medial meniscal extrusion by WB-US showed higher values (median 2.9 mm; IQR 2.2-3.6 mm) than NWB-US (median 2.1 mm; IQR 1.2- 3 mm) and MRI (median 1.0 mm; IQR 0.0-1.8 mm). Our WB-US findings assess

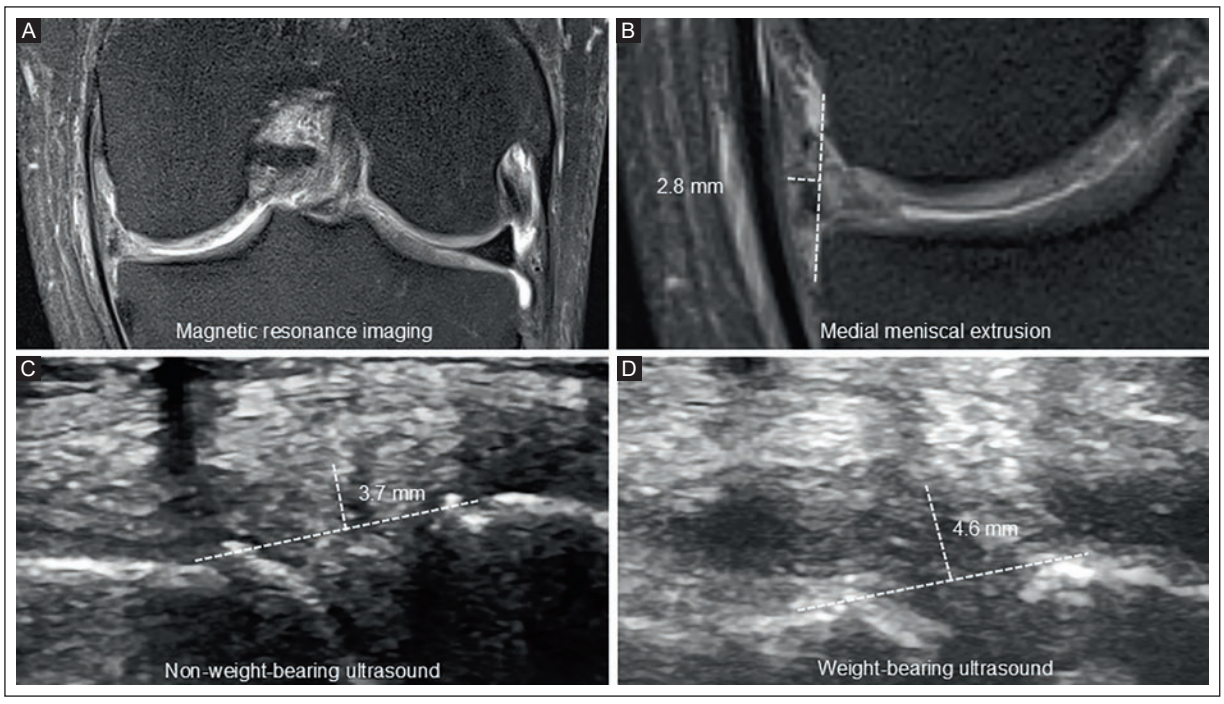

Figure 4. Comparison of imaging modalities of the medial meniscus in a 58-year-old obese man (BMI 31.5 kg/m²) with right knee pain. **A-B:** coronal proton density-weighted MRI with fat suppression shows minor medial meniscal extrusion of 2.8 mm. **C:** NWB-US shows a major 3.7 mm medial meniscal extrusion. **D:** WB-US shows a major 4.6 mm medial meniscal extrusion.
MRI: magnetic resonance imaging; NWB-US: non-weight-bearing ultrasound; WB-US: weight-bearing ultrasound.

meniscal biomechanics under load, thereby increasing the detection of medial meniscal extrusion.

Traditionally, medial meniscal extrusion assessment is performed using unloaded supine MRI[8], focusing predominantly on structural anatomy at rest[1,3]. In our study, WB-US detected 20 (40.0%) cases of minor meniscal extrusion versus 17 (34.0%) cases with NWB-US while 23 (46.0%) cases had major meniscal extrusion compared to only 13 (26.0%) by NWB-US, and 4 (8.0%) minor and 6 (12.0%) major meniscal extrusion cases by MRI, outperforming both techniques in identifying medial meniscal extrusion. Minor extrusion in the supine position may represent functionally relevant instability under load, detectable by WB-US[6,21]. WB-US provides a functional assessment of meniscal competence. By identifying more cases across the full spectrum of severity, this technique enables earlier diagnosis and more accurate characterization of meniscal instability, supporting a dynamic, functional assessment of meniscal pathology. WB-US identified more cases with minor and major medial meniscal extrusion than NWB-US and MRI. The dynamic nature of extrusion explains the disparities with static values and underscores WB-US's ability to identify early meniscal instability.

Older age and elevated BMI are significant risk factors for increased medial meniscal extrusion. The prospective study by Achtnich et al.[22] in 75 healthy volunteers showed a significant correlation between age and extrusion detected by NWB-US and WB-US ($p < 0.001$). Increased BMI was also significantly associated with meniscal extrusion under a load ($p = 0.002$). These researchers concluded that medial meniscal extrusion is an age- and BMI-dependent phenomenon, even in asymptomatic knees. In a study of 104 volunteers, Gregio-Junior et al.[9] evaluated medial meniscal extrusion using NWB-US and WB-US. Age had a significant impact on the increase in meniscal extrusion ($p = 0.001$). The study also showed significant variation in extrusion measurements between NWB-US and WB-US ($p = 0.0002$), suggesting that the loading condition is a critical factor. The authors concluded that age is a determining factor in meniscal extrusion and that differences in measurements across techniques underscore the complexity of its evaluation, in which the influence of other variables, such as BMI, may vary depending on the imaging method. The multicenter study by Crema et al.[4] analyzing a cohort of 1,527 subjects found a significant interaction between higher BMI and the imaging modality,

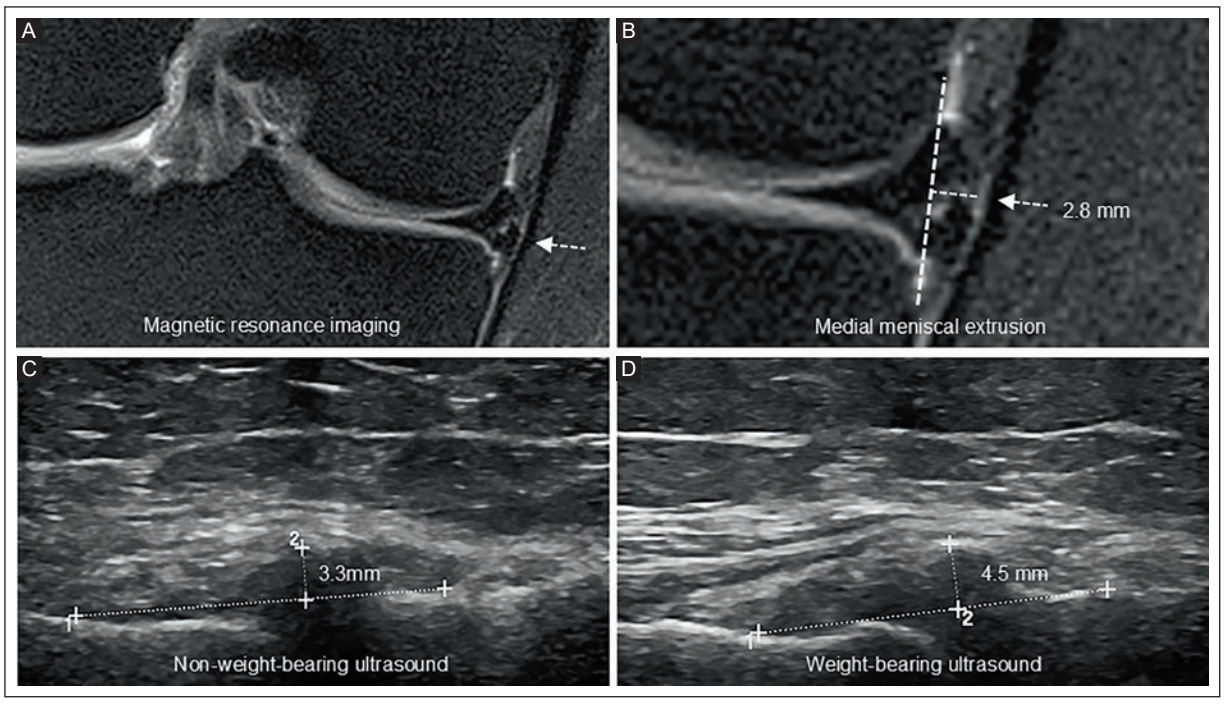

Figure 5. Comparison of imaging modalities of medial meniscal extrusion in a 41-year-old obese woman (BMI 39.7 kg/m^2) with knee pain. **A-B:** coronal proton density-weighted MRI with fat suppression shows minor medial meniscal extrusion of 2.8 mm (arrows). **C:** NWB-US shows major 3.3 mm medial meniscal extrusion. **D:** WB-US shows major 4.5 mm medial meniscal extrusion.

MRI: magnetic resonance imaging; NWB-US: non-weight-bearing ultrasound; WB-US: weight-bearing ultrasound.

suggesting that its influence on extrusion measurement may not be apparent on supine MRI but does manifest significantly under dynamic loading conditions such as WB-US, where joint forces are amplified. These findings support our results regarding age. The variation observed between NWB-US and WB-US suggests that the influence of BMI may be modulated by the imaging modality, an interaction our results demonstrate. The magnitude of extrusion depends on individual factors such as age, BMI, and loading conditions during assessment, linking the measurement to the imaging method used. The interpretation of medial meniscal extrusion should be contextualized by the patient's anthropometric profile and the imaging modality used, especially under functional loading conditions.

The most common finding associated with meniscal extrusion is a posterior meniscal root tear; isolated meniscal extrusion can also be observed[1]. The study by Gregio-Junior et al.[9] found that medial meniscal extrusion was associated with meniscal root tear in a small number of patients. They showed that knees with an extrusion ≥ 3 mm under load had MRI-confirmed tears, suggesting that extrusion severity may be an indirect indicator of structural damage and may present as an isolated finding in some cases. Krych et al.[23] examined 63 serial MRIs in patients with medial knee pain and noted that extruded menisci with intact roots progressed to develop a posterior root tear. Therefore, the extruded meniscus may increase biomechanical forces on the root attachment, leading to a complete root tear with minimal trauma. Chiba et al.[13] using fat-suppressed T2 MRI demonstrated that medial meniscal extrusion greater than 5 mm may be a risk factor for posterior root tear. This finding likely did not show a strong association in our study because the median medial meniscal extrusion was 2.9 mm (IQR 2.2-3.6 mm). WB-US may indicate meniscal instability even without a meniscal tear.

The main strength of this study is the direct comparison of imaging modalities for medial meniscal extrusion, including evaluation under actual axial loading – a rarely explored aspect. The appropriate use of non-parametric tests based on data distribution, corrections for multiple comparisons to reduce error risk, and the combined application of global and post hoc analyses to identify specific differences are also strengths. Additionally, the inclusion of robust tests for categorical variables, the consideration of potential confounding

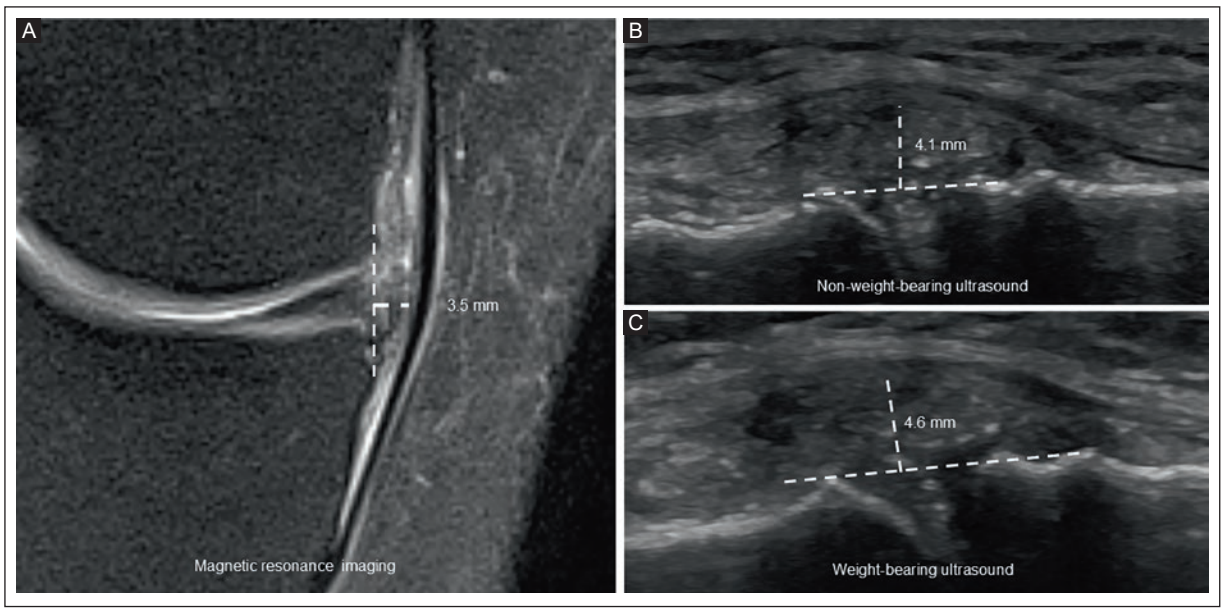

Figure 6. Comparison of imaging modalities for the medial meniscus of a 48-year-old obese man (BMI 31.2 kg/m²) with knee pain. **A:** coronal proton density-weighted MRI with fat suppression shows major 3.5 mm medial meniscal extrusion. **B:** NWB-US shows a major 4.1 mm medial meniscal extrusion. **C:** WB-US shows a major 4.6 mm medial meniscal extrusion.

MRI: magnetic resonance imaging; NWB-US: non-weight-bearing ultrasound; WB-US: weight-bearing ultrasound.

factors using linear mixed models, and the evaluation of correlations with appropriate methods further strengthen the study. As limitations, we acknowledge the cross-sectional design and small sample size, the operator-dependent nature of US, the potential influence of the patient's ability to stand. Interobserver and intraobserver concordance was not evaluated, although excellent intra- and interobserver agreement has been reported (ICC 0.95, 95% CI: 0.92-0.97)[10].

CONCLUSION

Our study provides evidence that WB-US has a greater ability than MRI and NWB-US to detect medial meniscal extrusion, supporting its value as a functional, accessible, and rapid diagnostic tool. Medial meniscal extrusion evaluated by WB-US should be considered a complementary functional assessment, not a replacement for the structural diagnosis provided by knee MRI. In clinical practice, a multimodal diagnosis of extrusion using ultrasound and MRI is ideal. WB-US can be used for screening and primary diagnostics, while MRI can confirm medial meniscal extrusion and assess associated pathology such as bone marrow edema, articular cartilage status, and meniscus integrity[1]. Incorporating WB-US as a first-line modality into diagnostic algorithms is recommended, along with the development of standardized protocols that account for loading conditions and individual patient characteristics. Future longitudinal studies with larger samples will be essential to validate the prognostic impact of these findings on the progression of meniscal pathology.

Acknowledgments

The authors thank Professor Ana M. Contreras-Navarro for her guidance in preparing and writing this scientific paper. The authors express their sincere gratitude to the Instituto Mexicano del Seguro Social for granting access to its facilities, equipment, and personnel, and especially for enabling patient recruitment and data collection. This original research in the Radiology Specialty field was an awarded thesis at the Tercera Convocatoria Nacional 2024-2025 "Las Mejores Tesis para Publicar en el JMeXFRI".

Funding

The authors declare that they have not received funding.

Conflicts of interest

The authors declare no conflicts of interest.

Ethical considerations

Protection of humans and animals. This study complied with the Declaration of Helsinki (1964) and subsequent amendments.

Confidentiality, informed consent, and ethical approval. The authors declare they followed their center's protocol for sharing patient data. Written informed consent was obtained from all study participants.

Declaration on the use of artificial intelligence. The authors did not use generative artificial intelligence to prepare this manuscript and/or create tables, figures, or figure legends.

REFERENCES

1. Langhans MT, Lamba A, Saris DBF, Smith P, Krych AJ. Meniscal extrusion: diagnosis, etiology, and treatment options. Curr Rev Musculoskelet Med. 2023;16(7):316-327. doi: 10.1007/s12178-023-09840-4.
2. Patel R, Eltgroth M, Souza R, Zhang CA, Majumdar S, Link TM. Loaded versus unloaded magnetic resonance imaging (MRI) of the knee: effect on meniscus extrusion in healthy volunteers and patients with osteoarthritis. Eur J Radiol Open. 2016;3: 100-107. doi: 10.1016/j.ejro.2016.05.002.
3. Costa CR, Morrison WB, Carrino JA. Medial meniscus extrusion on knee MRI: is extent associated with severity of degeneration or type of tear? AJR Am J Roentgenol. 2004;183(1):17-23. doi:10.2214/ajr.183.1.1830017.
4. Crema MD, Roemer FW, Felson DT, Englund M, Wang K, Jarraya M, et al. Factors associated with meniscal extrusion in knees with or at risk for osteoarthritis: the multicenter osteoarthritis study. Radiology. 2012; 264(2):494-503. doi:10.1148/radiol.12110986.
5. Nogueira-Barbosa MH, Gregio-Junior E, Lorenzato MM, Guermazi A, Roemer FW, Chagas-Neto FA, et al. Ultrasound assessment of medial meniscal extrusion: a validation study using MRI as reference standard. AJR Am J Roentgenol. 2015;204(3):584-588. doi:10.2214/AJR.14.12522.
6. Papalia GF, Za P, Saccone L, Franceschetti E, Zampogna B, Vasta S. Meniscal extrusion: risk factors and diagnostic tools to predict early osteoarthritis, Orthop Rev (Pavía). 2023;15:74881. doi:10.52965/001c.74881.
7. Gajjar SM, Solanki KP, Shanmugasundaram S, Kambhampati SBS. Meniscal extrusion: a narrative review. Orthop J Sports Med. 2021;9(11): 23259671211043797. doi:10.1177/23259671211043797.
8. Swamy N, Wadhwa V, Bajaj G, Chhabra A, Pandey T. Medial meniscal extrusion: detection, evaluation and clinical implications. Eur J Radiol. 2018;102:115-124. doi: 10.1016/j.ejrad.2018.03.007.
9. Gregio-Junior E. Taneja AK, Crema MD, Meneses-Reis R, Müller-Lorenzato M, Chagas-Neto FA. Effect of weightbearing on medial meniscal extrusion: dynamic ultrasound with MRI correlation. Acta Radiol. 2025;66(9): 982-990. doi:10.1177/02841851251339007.
10. Boksh K, Shepherd DET, Espino DM, Shepherd J, Ghosh A, Aujla R. Assessment of meniscal extrusion with ultrasonography: a systematic review and meta-analysis. Knee Surg Relat Res. 2024;36(1):33. doi: 10.1186/s43019-024-00236-3.
11. Cho JC, Tollefson L, Reckelhoff K. Sonographic evaluation of the degree of medial meniscal extrusion during Thessaly test in healthy knees. Chiropr Man Therap. 2021;29(1):31. doi:10.1186/s12998-021-00390-5.
12. Razek AA, Fouda NS, Elmetwaley N, Elbogdady E. Sonography of the knee joint. J Ultrasound. 2009;12(2):53-60. doi:10.1016/j.jus.2009.03.002.
13. Chiba D, Sasaki T, Ishibashi Y. Greater medial meniscus extrusion seen on ultrasonography indicates the risk of MRI-detected complete medial meniscus posterior root tear in a Japanese population with knee pain. Sci Rep. 2022; 12(1): 4756. doi: 10.1038/s41598-022-08604-3.
14. Heismann B, Ott M, Grodzki D. Sequence-based acoustic noise reduction of clinical MRI scans. Magn Reson Med. 2015;73(3):1104-1109. doi: 10.1002/mrm.25229.
15. Nemenyi PB. Distribution-free multiple comparisons: Princeton University; 1963.
16. Cochran WG. The comparison of percentages in matched samples. Biometrika. 1950;37(3-4):256-266. doi: 10.1093/biomet/37.3-4.256.
17. McNemar Q. Note on the sampling error of the difference between correlated proportions or percentages. Psychometrika. 1947;12(2): 153-157. doi: 10.1007/BF02295996.
18. Holm S. A simple sequentially rejective multiple test procedure. Scan J Statistics. 1979;6(2):65-70.
19. Daney BT, Aman ZS, Krob JJ, Storaci HW, Brady AW, Nakama G. Utilization of transtibial centralization suture best minimizes extrusion and restores tibiofemoral contact mechanics for anatomic medial meniscal root repairs in a cadaveric model. Am J Sports Med. 2019;47(7): 1591-1600. doi: 10.1177/0363546519844250.
20. Falkowski AL, Jacobson JA, Cresswell M, Bedi A, Kalia V, Zhang B. Medial meniscal extrusion evaluation with weight-bearing ultrasound: correlation with MR imaging findings and reported symptoms. J Ultrasound Med. 2022; 18(41):2867-2875. doi:10.1002/jum.15975.
21. Muzaffar N, Kirmani O, Ahsan M, Ahmad S. Meniscal extrusion in the knee: should only 3 mm be considered significant? Malays Orthop J. 2015;9(2):17-20. doi:10.5704/MOJ.1507.013.
22. Achtnich A, Petersen W, Willinger L, Sauter A, Rasper M, Wörtler K, et al. Medial meniscus extrusion increases with age and BMI and is depending on different loading conditions. Knee Surg, Sports Traumatol, Arthrosc. 2018;26(8):2282-2288. doi.org/10.1007/s00167-018-4885-7.
23. Krych AJ, LaPrade MD, Hevesi M, Rhodes NG, Johnson AC, Camp CL, et al. Investigating the chronology of meniscus root tears: do medial meniscus posterior root tears cause extrusion or the other way around? Orthop J Sports Med. 2020;8(11):2325967120961368. doi: 10.1177/2325967120961368.

JMeXFRI

Journal of the Mexican Federation of Radiology and Imaging

Check for updates

FULL RESEARCH ARTICLE

High sensitivity of O-RADS ultrasound for predicting malignant ovarian lesions in female pediatric patients: a 10-year review

Diana Nuñez-Garcia[1], *Sara A. Solorzano-Morales*[1]*, *Alfonso G. Ramirez-Ristori*[2] and *Emma Segura-Solis*[2]

[1]*Department of Radiology and Imaging;* [2]*Department of Pediatric Pathology. Instituto Nacional de Pediatria, Secretaria de Salud, Mexico City, Mexico*

ABSTRACT

Introduction: *The Ovarian-Adnexal Reporting and Data System (O-RADS) has been useful for risk stratification of malignancy in adult women. However, reports in female pediatric patients are scarce. This study evaluated the diagnostic performance of O-RADS ultrasound (US) in predicting malignant ovarian lesions in female pediatric patients.* **Material and methods:** *This cross-sectional study included female pediatric patients aged 0 to 17 years with ovarian lesions evaluated by US and histopathology. The O-RADS category, Color score, tumor markers, tumor size, and histological diagnosis were recorded. The diagnostic performance of O-RADS US was analyzed.* **Results:** *Seventy ovarian lesions in 66 female pediatric patients with a mean age of 12.6 ± 3.5 years were included. Most ovarian lesions were benign (n = 53, 75.7%) while 17 (24.3%) were malignant. O-RADS categories ≥ 3 showed a sensitivity of 94.1% (95% CI, 71.3-99.8) and negative predictive value of 96.0% (95% CI, 78.0-99.4) for detecting malignant lesions. The Doppler Color score ≥ 2 achieved a sensitivity of 100% (95% CI, 80.4-100) and a negative predictive value of 100% (95% CI, 92.2-100) for detecting malignancy. One (5.9%) O-RADS category 3, three (17.6%) category 4, and twelve (70.6%) category 5 lesions were malignant. Among 21 category 4 lesions, three (37.5%) malignant ovarian lesions were subcategory 4B, while none were subcategory 4A. In contrast, among benign ovarian lesions, 13 (100%) were classified as O-RADS subcategory 4A and 5 (62.5%) as 4B.* **Conclusion:** *O-RADS US categories ≥ 3 as well as Doppler Color scores ≥ 2 showed high sensitivity for differentiating malignant from benign ovarian lesions in female pediatric patients.*

Keywords: *Ovarian-Adnexal Reporting and Data System. Ovarian neoplasms. Female. Pediatric. Doppler Color. Ultrasound.*

INTRODUCTION

Ovarian lesions are rare in the pediatric population, with an estimated incidence of 2.6 cases per 100,000 per year[1,2]. Although most lesions are benign (75% to 90%), early diagnosis is essential to ensure timely management of malignant cases (10% to 25%)[3]. Symptoms, such as abdominal pain, abdominal distension, and a palpable mass, are usually nonspecific[4]. Ultrasound (US) is the initial imaging modality of choice due to its accessibility, the absence of ionizing radiation, and excellent resolution for pelvic structures, especially in children[5]. Color and spectral Doppler US provide additional information about vascularization, helping differentiate benign and malignant lesions[6]. Modalities such as computed tomography and magnetic resonance imaging are reserved for further characterization or staging of ovarian lesions[7].

Ovarian-Adnexal Reporting and Data System (O-RADS) US[8] has become a widely validated risk stratification tool for ovarian lesions in adult women[9-11].

***Corresponding author:**
Sara A. Solorzano-Morales
E-mail: dras.solorzano@yahoo.com.mx

Received for publication: 13-08-2025
Accepted for publication: 10-09-2025
DOI: 10.24875/JMEXFRI.M25000119

Available online: 15-01-2026
J Mex Fed Radiol Imaging. 2025;4(4):243-253
www.JMeXFRI.com

In a clinical decision analysis, O-RADS provided significant benefits for identifying high-risk lesions. Additionally, O-RADS shows a high level of inter-reader agreement (κ = 0.77-0.83), regardless of radiologists' training level or practical experience[9,12-14]. Reports regarding the diagnostic performance of O-RADS US in female pediatric patients are scarce[15,16]. The sensitivity of O-RADS categories 4 and 5 for predicting malignant ovarian lesions has been reported at 94.4%, suggesting that O-RADS is a good tool for differentiating benign from malignant lesions in female pediatric patients[15,16]. This study evaluated the diagnostic performance of O-RADS US in predicting malignancy in ovarian lesions confirmed histopathologically in female pediatric patients.

MATERIAL AND METHODS

This cross-sectional, retrospective study was conducted from January 2013 to December 2023 in the Department of Radiology and Imaging at the Instituto Nacional de Pediatria, a referral center in Mexico City, Mexico. Female pediatric patients (0-17 years) who underwent US examination with a confirmed diagnosis of ovarian lesion by histopathology were included. Patients with prior pelvic surgery, chemotherapy, radiotherapy, a poor-quality US examination, or incomplete clinical records were excluded. Informed consent was not required, as this was an observational study using information obtained from routine clinical practice. The study was approved by the Institutional Research and Ethics Committees.

Study development and variables

The variables obtained from clinical records included age, and signs and symptoms such as abdominal pain, abdominal distention, heavy menstrual bleeding, and constipation. Laterality, size, and volume of the ovarian lesion; tumor markers, including lactate dehydrogenase (LDH), alpha-fetoprotein (AFP), and the beta subunit of human chorionic gonadotropin (β-hCG), and the surgical specimen pathology result were recorded. US findings were reported according to O-RADS categories and Color score[8]. Histopathologic diagnoses were also reported.

Imaging acquisition and analysis protocol

Pelvic US examination was performed using Philips EPIQ 7G (Philips Healthcare, Amsterdam. The Netherlands) or General Electric LOGIQ (GE, Milwaukee, WI. USA) scanners with a 3-6 MHz convex transducer following grayscale and color Doppler protocols[17,18]. Ovarian lesions were classified according to the characteristics defined by the O-RADS US lexicon[8]: categories 3, 4, and 5 were grouped as categories ≥ 3 to differentiate malignant from benign ovarian lesions. Vascularization of the lesion was classified using a qualitative O-RADS Color score as follows: 1, no flow; 2, minimal flow; 3, moderate flow; and 4, abundant or marked flow. Color scores 2, 3, and 4 were grouped as categories ≥ 2 to differentiate malignant from benign ovarian lesions. US images were retrospectively reviewed by a pediatric radiologist (SSM) with 20 years of experience and, under supervision, a specialist pediatric radiology resident (DNG) with 4 years of experience.

Ovarian tumor markers

LDH, AFP, and β-hCG determinations were performed in blood. The procedures were carried out according to the manufacturer's recommendations and the standardized protocols of the institution's laboratory.

Histopathologic analysis

The pathology records were reviewed to identify ovarian lesions in female pediatric patients and to determine the diagnosis according to the WHO classification[19]. Pathologic examination was performed by a pediatric pathologist (ARR) with 7 years of experience.

Statistical analysis

Descriptive statistics summarized quantitative variables using measures of central tendency. Qualitative variables were reported as frequency and percentage. Sensitivity, specificity, positive predictive value, negative predictive value, and accuracy of O-RADS US categories ≥ 3 and the Color score ≥ 2 for predicting malignant ovarian lesions, were calculated. Statistical analysis was performed using SPSS version 25 (IBM Corp., Armonk, NY, USA).

RESULTS

Seventy ovarian lesions in 66 female pediatric patients with a mean age of 12.6 ± 3.5 years (range, 1 to 17) were included (Table 1). The presenting signs and symptoms were abdominal pain in 66.6% (n = 44),

Table 1. Characteristics of 66 female pediatric patients with ovarian lesions

Description	Parameter
Age, years, mean ± SD (min-max)	12.6 ± 3.5 (1-17)
Signs and symptoms, n (%)	
Abdominal pain	44 (66.6)
Hypermenorrhea	10 (15.2)
Abdominal distention	10 (15.2)
Constipation	2 (3.0)
Laterality of ovarian lesion, n (%)	
Right	38 (57.5)
Left	24 (36.3)
Bilateral	4 (6.2)
Tumor markers, n (%)	
Positive	9 (13.6)
Negative	57 (86.4)
Surgical specimen pathology result, n (%)	
Ovary	57 (81.4)
Cyst	12 (17.2)
Capsule cyst	1 (1.4)
Diameter (cm), mean ± SD	
Benign ovarian lesion	n = 53
Longitudinal	10.9 ± 5.8
Anteroposterior	6.7 ± 4.0
Transverse	7.2 ± 3.2
Malignant ovarian lesion	n = 17
Longitudinal	14.2 ± 5.3
Anteroposterior	10.9 ± 2.5
Transverse	9.1 ± 4.2
Ovarian lesion volume (cc), mean ± SD	
Benign lesion	465 ± 836
Malignant lesion	899 ± 694.1

SD: standard deviation; cm: centimeter; cc: cubic centimeter.

hypermenorrhea and abdominal distension in 15.2% (n = 10) each, and constipation in 3.0% (n = 2). The lesion was most commonly located on the right in 57.5% (n = 38), on the left in 36.3% (n = 24), and bilateral in 6.2% (n = 4) of cases. Tumor markers were positive in 13.6% (n = 9) of cases. The surgical specimen was the ovary in 81.4% (n = 57) of cases, followed by cysts in 17.2% (n = 12), and the cyst capsule in 1.4% (n = 1). Among the histopathologic results, 75.7% (n = 53) were benign, and 24.3% (n = 17) were malignant ovarian tumors. The mean diameter of benign ovarian lesions was 10.9 ± 5.8 cm in the longitudinal axis, 6.7 ± 4.0 cm in the anteroposterior axis, and 7.2 ± 3.2 cm in the transverse axis. In contrast, malignant ovarian lesions measured 14.2 ± 5.3 cm in the longitudinal axis, 10.9 ± 2.5 cm in the anteroposterior axis, and 9.1 ± 4.2 cm in the transverse axis. Both the transverse and anteroposterior diameters were significantly associated with malignancy (p = 0.001 and p = 0.003, respectively). The mean volume of benign lesions was 465 ± 836 cc, and 899 ± 694 cc for malignant lesions.

Comparison of O-RADS US findings between benign and malignant ovarian lesions

Benign lesions (n = 53) by O-RADS were most commonly, a unilocular cyst, solid component (n = 18, 34.0%), followed by a multilocular cyst, no solid component (n = 12, 22.6%), and a typical dermoid cyst (n = 12, 22.6%) (Table 2); a multilocular cyst with a solid component, unilocular cyst with a solid component, and endometriomas were less frequent. In contrast, malignant ovarian lesions (n = 17) were most commonly solid or solid-appearing (n = 14, 82.3%), followed by multilocular cyst with a solid component (n = 2, 11.8%) and a multilocular cyst, no solid component (n = 1, 5.9%).

Benign ovarian lesions showed no differences between lesions ≤ 10 cm and those > 10 cm in diameter (n = 26 and n = 27, respectively). In contrast, malignant ovarian lesions (n = 10, 58.8%) commonly had a greater diameter (> 10 cm). The external contour was smooth in all benign ovarian lesions (n = 53, 100%). In contrast, most malignant ovarian lesions had an irregular external contour (n = 12, 70.6%). The color Doppler flow showed that most benign ovarian lesions were Color score 1 (n = 46, 86.8%), whereas none of the malignant ovarian lesions were classified as Color score 1. In contrast, malignant ovarian lesions were classified as Color score 2 (n = 4, 23.5%), Color score 3 (n = 9, 53.0%), or Color score 4 (n = 4, 23.5%). Among the extraovarian findings, fluid was present in 3 (17.6%) of 17 malignant ovarian lesions. No patient had peritoneal thickening or nodules.

Benign or malignant histopathologic diagnoses of 70 ovarian lesions in relation to O-RADS US categories and tumoral markers

The histopathologic diagnoses of benign ovarian lesions were mature teratoma (n = 20), serous

Table 2. Comparison of O-RADS US findings of benign and malignant ovarian lesions

Description	Total, n	Benign lesions, (n = 53)	Malignant lesions, (n = 17)
Lesion category, n (%)			
Unilocular cyst, no solid components	18	18 (34.0)	-
Unilocular cyst with solid component(s)	4	4 (7.5)	-
Multilocular cyst, no solid component(s)	13	12 (22.6)	1 (5.9)
Multilocular cyst with solid component(s)	5	3 (5.7)	2 (11.8)
Solid or solid-appearing (≥ 80%)	15	1 (1.9)	14 (82.3)
Typical dermoid cyst	12	12 (22.6)	-
Typical endometrioma	3	3 (5.7)	-
Diameter, n (%)			
≤ 10 cm	33	26 (49.1)	7 (41.2)
> 10 cm	37	27 (50.9)	10 (58.8)
External contour, n (%)			
Smooth	58	53 (100)	5 (29.4)
Irregular	12	-	12 (70.6)
Color score, n (%)			
1	46	46 (86.8)	-
2	11	7 (13.2)	4 (23.5)
3	9	-	9 (53.0)
4	4	-	4 (23.5)
Extra ovarian findings, n (%)			
Fluid	3	-	3 (17.6)

No female pediatric patient with peritoneal thickening or nodules. O-RADS: Ovarian Reporting and Data System; US: ultrasound.

cystadenoma (n = 18), cystadenofibroma (n = 7), mucinous cystadenoma (n = 5), endometrioma (n = 1), dermoid cyst (n = 1), and necrosis (n = 1) (Table 3). Figures 1 and 2 show benign ovarian lesions. The histopathologic diagnoses of malignant ovarian lesions were dysgerminoma (n = 6), yolk sac tumor (n = 4), mixed germ cell tumor (n = 2), mature and immature teratoma (n = 1), juvenile granulosa cell tumor (n = 2), and leukemic infiltration (n = 2). Figures 3 and 4 show malignant ovarian lesions.

Twenty-four lesions (96.0%) of 25 O-RADS category 2 and 11 lesions (91.6%) of 12 O-RADS category 3 were benign ovarian lesions, whereas only 1 (4.0%) of 21 O-RADS category 4 was benign. In contrast, malignant ovarian lesions were commonly O-RADS categories 4 (n = 3, 17.6%) and 5 (n = 12, 70.6%). All O-RADS category 5 lesions were malignant (n = 12). Tumor markers were negative in all benign ovarian cases and positive in 5 malignant cases.

O-RADS 4 subcategories in relation to benign and malignant ovarian lesions

Twenty-one (30.0%) of 70 ovarian lesions were classified as O-RADS category 4 (Table 4). Three (37.5%) malignant ovarian lesions were in subcategory 4B, while none were in subcategory 4A. In contrast, among benign ovarian lesions, 13 (100%) were classified as O-RADS subcategory 4A and 5 (62.5%) as 4B.

Diagnostic performance of O-RADS US categories and Color score for predicting malignant lesions

The O-RADS categories ≥ 3 showed high sensitivity at 94.1% (95% CI, 71.3-99.8) and a negative predictive value of 96.0% (95% CI, 78.0-99.4) for predicting malignant ovarian lesions (Table 5). However, specificity (45.3%, 95% CI, 31.5-59.5) and positive predictive

Table 3. Benign or malignant histopathologic diagnosis of 70 ovarian lesions in relation to O-RADS US categories and tumor markers

Description	n	O-RADS category				Tumor markers
		2	3	4	5	
Benign ovarian lesions, n						
Mature teratoma	20	12	1	7	-	Negative
Serous cystadenoma	18	8	6	4	-	Negative
Cystadenofibroma	7	1	4	2	-	Negative
Mucinous cystadenoma	5	1	-	4	-	Negative
Endometrioma	1	1	-	-	-	Negative
Dermoid cyst	1	1	-	-	-	Negative
Necrosis	1	-	-	1	-	Negative
Subtotal, n (%)	53	24	11	18	-	
Malignant ovarian lesions, n						
Dysgerminoma	6	-	-	-	4	Positive
		-	-	-	2	Negative
Yolk sac tumor	4	-	1	-	3	Positive
		-	-	-	-	Negative
Mixed germinal tumor	2	-	-	1	-	Positive
		-	-	-	1	Negative
Mature and immature teratoma	1	-	-	-	1	Positive
		-	-	-	-	Negative
Juvenile granulosa cell tumor	2	-	-	-	-	Positive
		1	-	-	1	Negative
Leukemic infiltration	2	-	-	2	-	Positive
		-	-	-	-	Negative
Subtotal, n (%)	17	1	1	3	12	
Total, n (%)	70	25	12	21	12	

O-RADS: Ovarian Reporting and Data System; US: ultrasound.

value (35.2%, 95% CI, 29.2-41.6) were lower. There were 16 true positives for malignant lesions and 24 true negatives. In contrast, there were 29 false positives and only one false negative ovarian lesion.

The Color score ≥ 2 showed better diagnostic performance for all evaluated parameters, with a sensitivity of 100% (95% CI, 80.4-100) and a negative predictive value of 100% (95% CI, 92.2-100). The specificity was 86.8% (95% CI, 74.6-94.5) and the positive predictive value was 70.5% (95% CI, 54.5-82.6). There were 17 true positive results for malignant lesions and 46 true negatives. In contrast, there were 7 false positives and no cases with a false negative result.

DISCUSSION

Our study showed that O-RADS categories ≥ 3 and Color scores ≥ 2 were useful for risk stratification of ovarian lesions in female pediatric patients, with high sensitivity for predicting malignant ovarian lesions. This is the first study in Mexico to evaluate the diagnostic performance of O-RADS and demonstrate that it is a useful tool for predicting malignant ovarian lesions in female pediatric patients.

Knowledge of ovarian lesion characterization has historically been based on studies in adult populations, where O-RADS has proven to be a reliable diagnostic tool for malignancy risk stratification. Recently, Wang et al.[15] retrospectively examined 163 histopathologically confirmed ovarian lesions from 159 female pediatric patients in China. Of these lesions, 89% (n = 145) were benign, and 11% (n = 18) were malignant. In O-RADS categories 4 and 5, the malignancy rates were 23.1% and 62.5%, respectively. O-RADS category > 3 had a sensitivity of 94.4% and specificity of 86.2% for

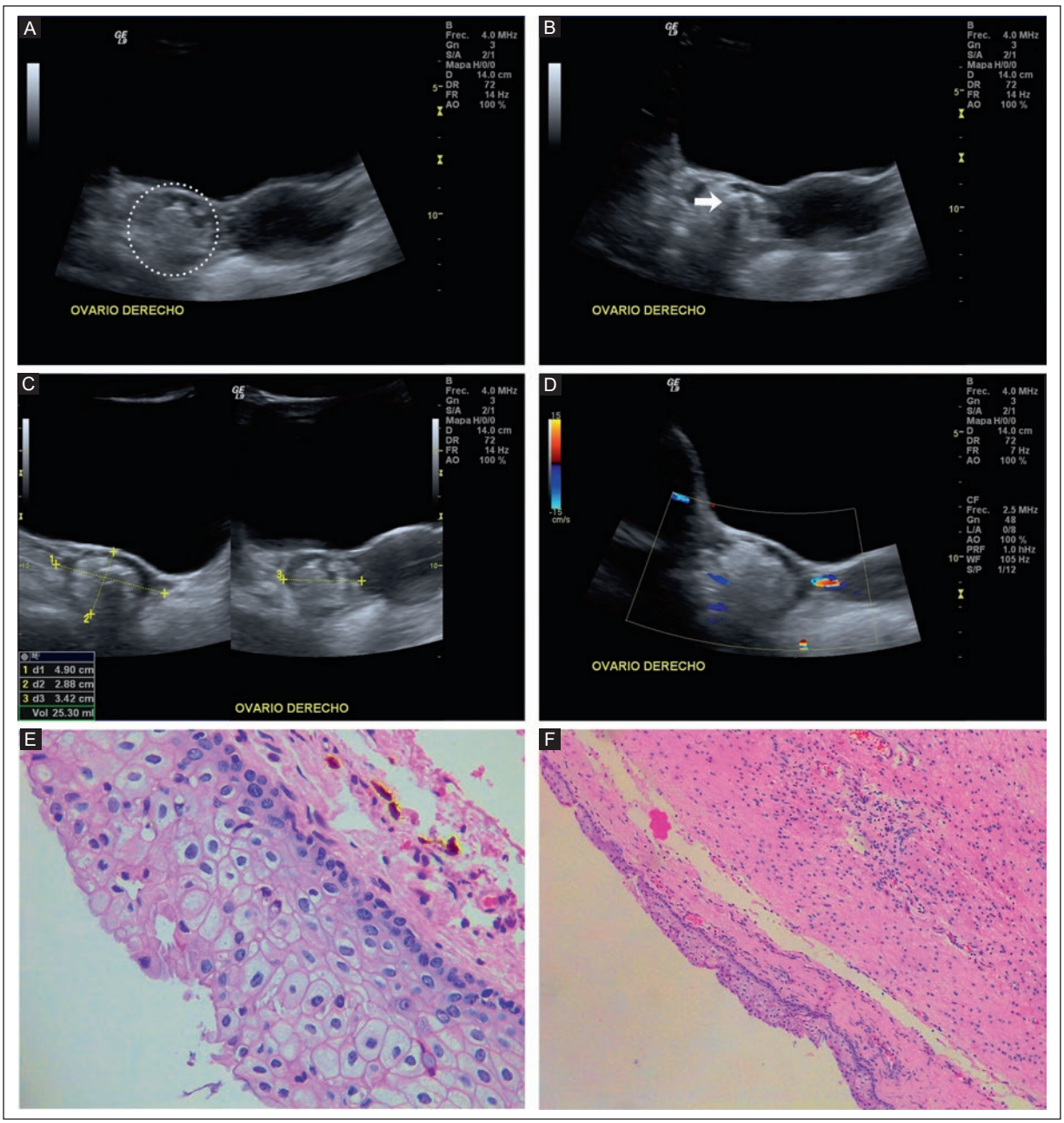

Figure 1. Pelvic US from a 16-year-old girl with hypermenorrhea. **A:** transverse view shows an ovoid, heterogeneous lesion with a hyperechoic center toward the right ovary (dotted circle). **B:** transverse view shows hyperechoic component with acoustic shadowing (arrow). **C:** the longitudinal axis measures 4.9 cm, the transverse axis 3.4 cm, and the anteroposterior axis 2.8 cm. Ovarian lesion volume is 25.3 c.c. **D:** Doppler US shows no vascularity. Color score 1, O-RADS category 2. **E:** H&E stain (40x). Monodermal squamous epithelium without atypia or somatic (malignant) transformation. Some hemosiderin is observed in the underlying stroma. **F:** H&E stain (4x). Cystic wall layered beneath by stratified squamous epithelium; glial tissue, smooth muscle, and an inflammatory infiltrate are identified. The histopathologic diagnosis was mature teratoma.

US: ultrasound; H&E: hematoxylin and eosin.

predicting malignancy. Wu et al.[16] analyzed 375 ovarian lesions in 364 female pediatric patients (≤ 17 years) in China and found a malignancy rate of 2.1% (n = 8). The O-RADS system achieved an AUC of 0.989, with 100% sensitivity and 96.5% specificity for lesions in category ≥ 4, and specificity ranging from 92% to 100%. In our study, the malignancy rates were 5.9% for O-RADS category 3, 17.6% for category 4, and 70.6% for category 5. O-RADS categories ≥ 3 showed high sensitivity (94.1%) for predicting malignant ovarian lesions.

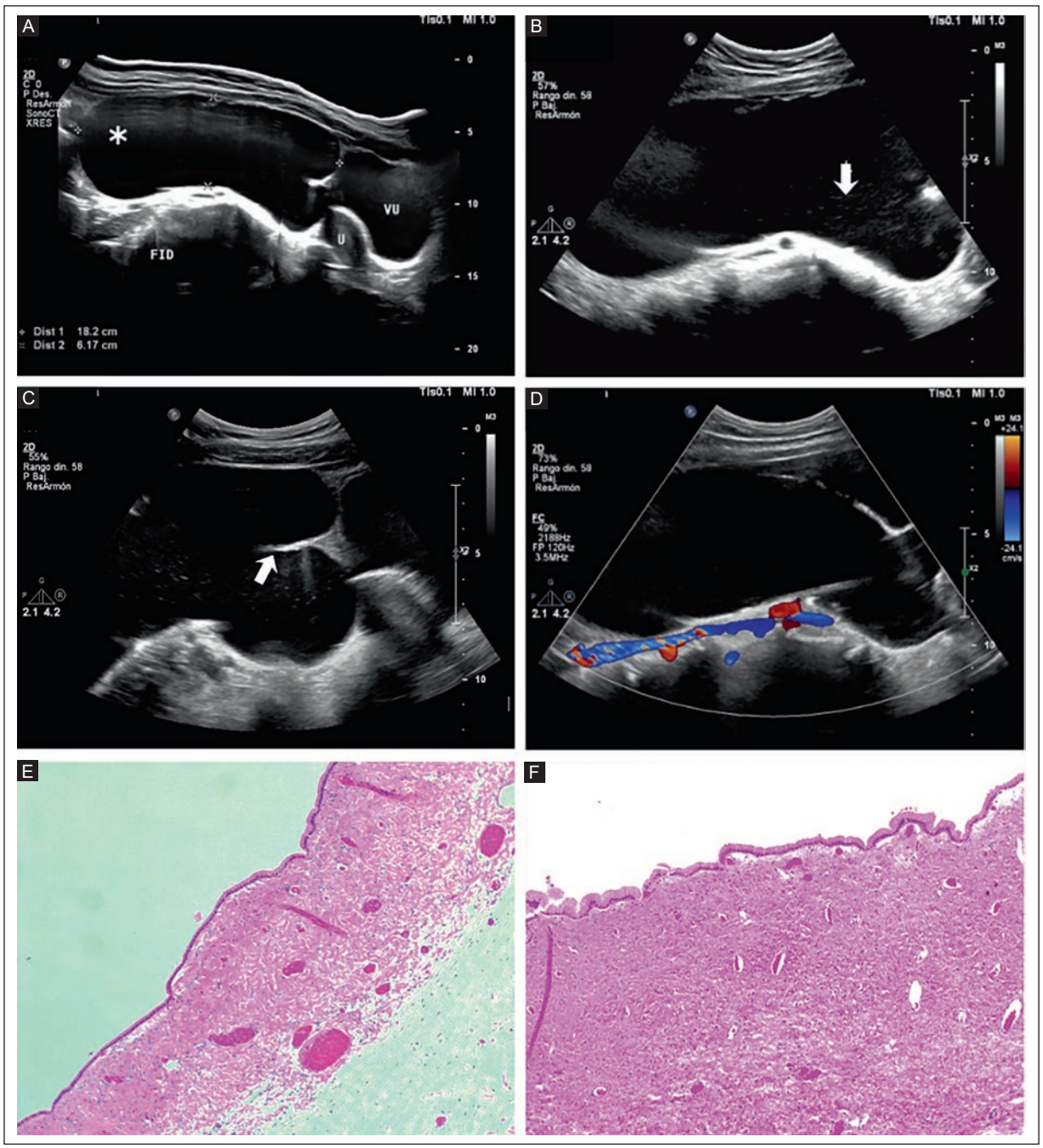

Figure 2. Pelvic US of an 11-year-old girl with hypermenorrhea. **A:** panoramic grayscale US of the right iliac fossa shows a cystic-appearing lesion at the anatomical site of the right ovary (star), measuring 18.2 cm (longitudinal axis), 15.9 cm (transverse axis, not shown), and 6.1 cm (anteroposterior axis). Ovarian lesion volume is 923 cc. **B:** a predominantly anechoic ovarian tumor in transverse view with a few internal floating spots (arrow). **C:** transverse view of a non-simple unilocular cyst shows incomplete septa (arrow), but no solid component. **D:** color Doppler US shows no vascularity. Color score 1, O-RADS category 3. **E:** H&E stain (10x). A cyst wall of fibrovascular tissue lined by simple epithelium. **F:** H&E stain (40x). The cyst inner lining consists of simple columnar epithelium with apical vacuoles. The histopathologic diagnosis was serous cystadenoma.

US: ultrasound; H&E: hematoxylin and eosin.

These results are comparable with previous reports[15,16]. In our study the addition of Color score showed higher diagnostic performance in all parameters for predicting malignant ovarian lesions. However, the specificity of O-RADS categories ≥ 3 was low (45.3%), with 29 (41.4%) false positives, possibly due to the inclusion of category 3 cases which had a lower frequency of malignancy (5.9%). In contrast, the studies by Wang[15] and

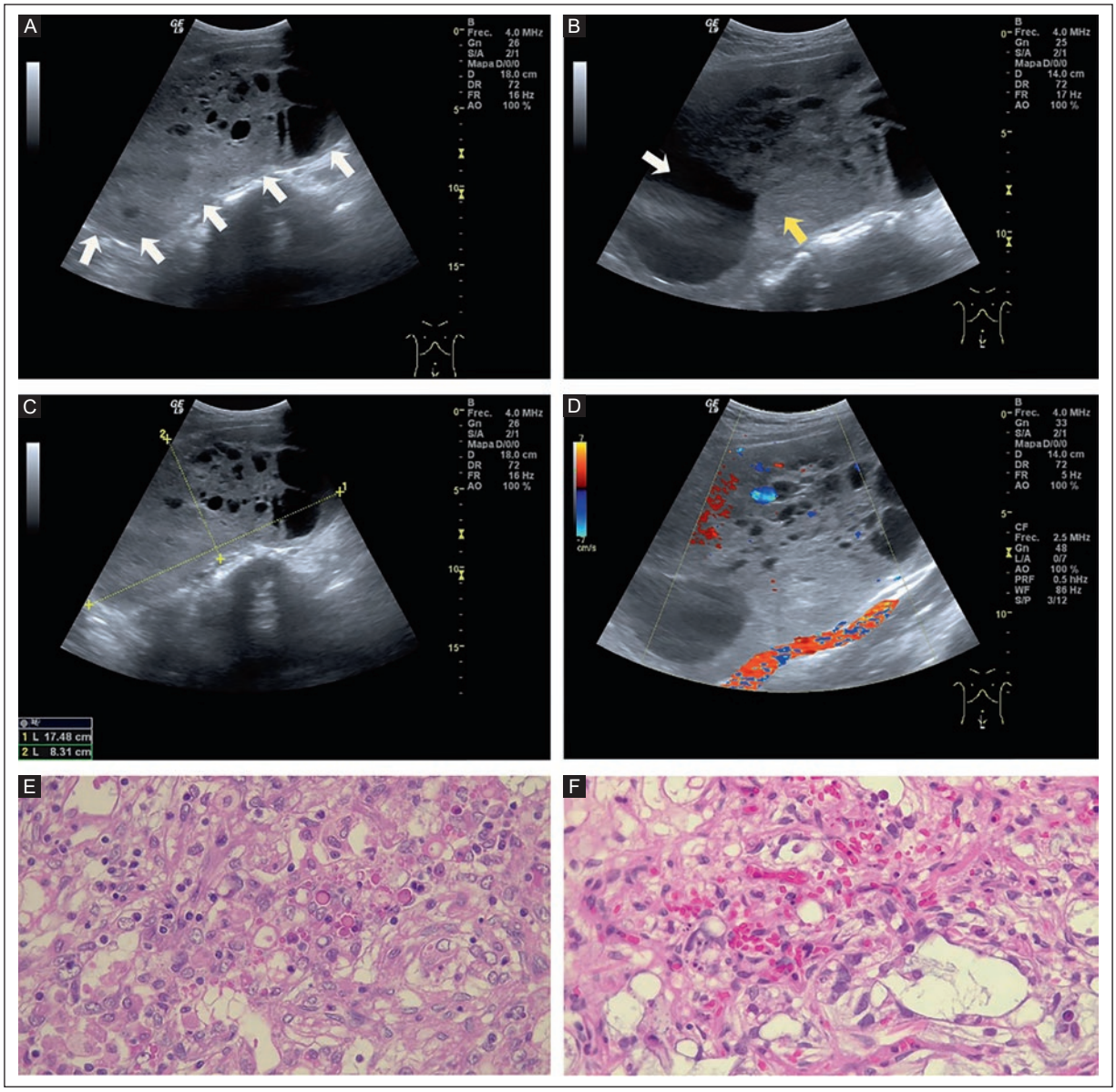

Figure 3. Pelvic grayscale US of a 12-year-old girl with hypermenorrhea and increased abdominal volume. **A:** longitudinal view of the pelvic cavity shows a large heterogeneous ovarian lesion with a solid component greater than 80% and some cystic areas with a smooth contour (arrows). **B:** longitudinal view shows cystic areas (white arrow) with solid portions (yellow arrow). **C:** longitudinal view of the ovarian lesion extends from the hypogastrium to the mesogastrium with a longitudinal axis of 17.4 cm, a transverse axis (not shown) of 9.0 cm, and an anteroposterior axis of 8.3 cm. Ovarian lesion volume is 683.6 cc. **D:** color Doppler US longitudinal view revealed internal vascularity with moderate flow. Color score 3, O-RADS category 4. **E:** H&E stain (40x). A heterogeneous neoplasm with solid growth, moderate nuclear atypia, and hyaline globules, with a focal myxoid background. **F:** H&E stain (40x). Cells with moderate nuclear atypia and a clear microcystic pattern. The histopathologic diagnosis was yolk sac tumor.

US: ultrasound; H&E: hematoxylin and eosin.

Wu[16] included only categories ≥ 4, with specificity ranging from 86.2% to 100%. O-RADS is a useful and reproducible tool for risk stratification in predicting malignant ovarian lesions in female pediatric patients.

A significant association between tumor size and ovarian malignancy has been reported. In the study by Wang et al.[15] the median diameter of malignant lesions was 11.5 cm, significantly larger than that of benign lesions (6.5 cm, p = 0.012), suggesting that accelerated tumor growth may be associated with malignant behavior. However, the authors emphasize that, although size is an important indicator, it is not sufficient on its own to accurately differentiate benign from malignant lesions, as certain benign lesions – such as mature

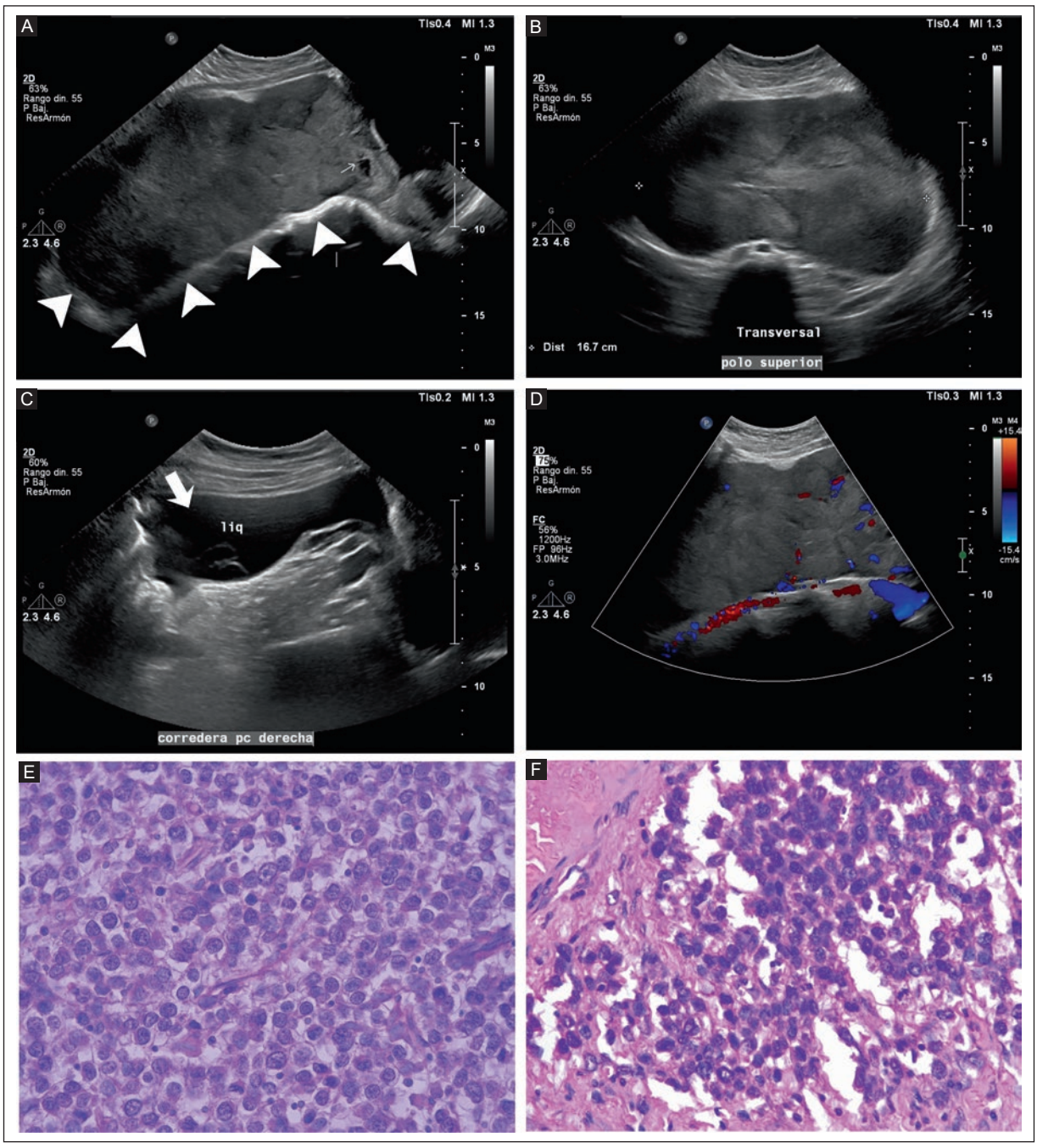

Figure 4. Pelvic grayscale US of a 15-year-old girl with asymptomatic abdominal distention. **A:** longitudinal view shows, in the topography of the left ovary, a large hypoechoic solid lesion with few cystic areas and irregular contour (arrowheads). **B:** transverse view, with dimensions of 25 cm (longitudinal axis, not shown), 16.7 cm (transverse axis), and 10.6 cm (anteroposterior axis, not shown). Ovarian lesion volume is 2,314.5 cc. **C:** longitudinal view at the level of the left parietocolic gutter shows anechoic fluid (arrow). **D:** a color Doppler US in longitudinal view shows moderate peripheral and internal vascularity. Color score 3, O-RADS category 5. **E** and **F:** H&E stain, 40x. Medium-sized cells with an eosinophilic cytoplasm, regular ovoid nuclei, granular chromatin, and moderate nucleoli. Septal infiltrating lymphocytes are seen. The histopathologic diagnosis was dysgerminoma.

US: ultrasound; H&E: hematoxylin and eosin.

teratomas or cystadenomas – can reach similar dimensions. In the study by Wu et al.[16], the median diameter of the lesions was 4.2 cm (interquartile range 3.4-5.7 cm), most ovarian lesions were benign, and only 2.1% were malignant. In our study, larger size was associated with a higher frequency of ovarian malignancy. Both the transverse and anteroposterior diameters were significantly associated with a higher frequency

Table 4. O-RADS US subcategories 4A and 4B associated with benign or malignant ovarian lesions

Description	Total (n = 21)	O-RADS 4A (n = 13)	O-RADS 4B (n = 8)
Benign ovarian lesion, n (%)	18	13 (72.2)	5 (27.8)
Malignant ovarian lesion, n (%)	3	-	3 (100)

O-RADS: Ovarian Reporting and Data System; US: ultrasound.

Table 5. Diagnostic performance of O-RADS US predicting malignant ovarian lesions in female pediatric patients

Parameter	Categories ≥ 3 % (95% CI)	Color score ≥ 2 % (95% CI)
Sensitivity	94.1 (71.3-99.8)	100 (80.4-100)
Specificity	45.3 (31.5-59.5)	86.8 (74.6-94.5)
Positive predictive value	35.2 (29.2-41.6)	70.5 (54.5-82.6)
Negative predictive value	96.0 (78.0-99.4)	100 (92.2-100)
Accuracy	57.0 (44.6-68.7)	89.9 (80.4-95.8)

O-RADS: Ovarian Reporting and Data System; US: ultrasound.

of malignancy (p = 0.001 and p = 0.003, respectively). In our cases, some benign tumors, especially teratomas, were large, which can limit the accuracy of image classification, particularly in standardized systems like O-RADS, where increased size can raise suspicion without necessarily implying malignancy. Diameter should not be used as an isolated risk criterion for ovarian malignancy in female pediatric patients.

O-RADS subcategories 4A and 4B, associated with benign and malignant ovarian lesions, respectively, have been proposed to improve risk stratification for malignancy based on morphological patterns by O-RADS[15]. Unilocular cysts with a solid component and multilocular cysts, no solid components are classified as O-RADS subcategory 4A. In contrast, the remaining cystic lesions with solid components are classified as O-RADS subcategory 4B. This classification showed a 10% risk of malignancy (1 out of 10 patients) for O-RADS subcategory 4A and a 50% risk (8 out of 16 patients) for O-RADS subcategory 4B[15]. Classification into subcategories 4A and 4B significantly improved risk stratification, differentiating groups with low versus high probability of malignancy (p = 0.037)[15]. In our study, among 21 lesions O-RADS category 4, all three (37.5%) malignant ovarian lesions were subcategory 4B, while none were subcategory 4A. Among benign ovarian lesions, 13 (100%) were classified as O-RADS subcategory 4A and 5 (62.5%) as subcategory 4B. Subdividing O-RADS into subcategories 4A and 4B could enhance diagnostic precision and clinical decision-making, particularly in age groups where ovarian preservation is a priority.

Tumor markers (such as LDH, AFP, and β-hCG) can provide complementary information when evaluating pediatric ovarian lesions. Wang et al.[15] showed that these markers are not specific enough to differentiate benign from malignant ovarian lesions on their own. Their usefulness lies in integrating them with a structured evaluation using O-RADS US, which improves preoperative stratification and guides therapeutic decisions aimed at preserving ovarian function. In germ cell tumors, these markers are relevant for monitoring and detecting recurrences. In our study, 53 benign lesions were negative for tumor markers; among the 17 malignant lesions, 29.4% (5 patients) were negative for tumor markers. Our results confirm that the absence of tumor markers does not exclude malignancy and that these markers should be considered only a complementary tool with limited diagnostic utility in female pediatric patients.

The strengths of this study include the use of a validated classification system for ovarian lesions, the O-RADS lexicon. All cases underwent histopathologic examination, and US findings were reported without knowledge of the histological results, ensuring blinded evaluation and reducing interpretation bias. Limitations include the retrospective design and small sample size. The number of cases with malignant results was small, so the specificity of O-RADS categories ≥ 3 for predicting malignancy was low. Including cases with O-RADS category 3 to differentiate malignant from benign ovarian lesions increased the number of false positives. Interobserver agreement was not evaluated in our study, although previous reports have demonstrated high consistency in the application of O-RADS descriptors regardless of the radiologist´s experience[15].

CONCLUSION

O-RADS US categories ≥ 3 showed high sensitivity and negative predictive value in distinguishing malignant from benign ovarian lesions in female pediatric patients. Adding a Color score ≥ 2 improved diagnostic performance for predicting malignant ovarian lesions across all parameters. Subclassifying category 4 into 4A and 4B appears promising for refining malignancy risk stratification in this population. Incorporating O-RADS US categories and Color score parameters into risk stratification for ovarian lesions in female

pediatric patients is recommended. Future studies with larger sample sizes are needed to validate these findings and optimize specific O-RADS adjustments for female pediatric patients.

Acknowledgments

The authors thank Professor Ana M. Contreras-Navarro for her guidance in preparing and writing this scientific paper. This original research in the Radiology Specialty field was an awarded thesis at the *Tercera Convocatoria Nacional 2024-2025 "Las Mejores Tesis para Publicar en el JMeXFRI"*.

Funding

The authors declare that they have not received funding.

Conflicts of interest

The authors declare that they have no conflicts of interest.

Ethical considerations

Protection of Individuals. The authors declare that this study complied with the Declaration of Helsinki (1964) and subsequent amendments.

Confidentiality, informed consent, and ethical approval. The authors declare that they followed their center's protocol for sharing patient data. Informed consent was not required for this observational study of information collected during routine clinical care.

Declaration on the use of artificial intelligence. The authors declare that not use generative artificial intelligence to prepare this manuscript or to create tables, figures, or figure legends.

REFERENCES

1. Heo SH, Kim JW, Shin SS, Jeong SI, Lim HS, Choi YD, et al. Review of ovarian tumors in children and adolescents: radiologic-pathologic correlation. Radiographics. 2014;34(7):2039-2055. doi: 10.1148/rg.347130144.
2. Vázquez-Rueda F, Murcia-Pascual FJ, Siu-Uribe A, Ortega-Salas RM, Escassi-Gil Á, Garrido-Pérez JI, et al. Análisis de los tumores sólidos ováricos pediátricos en nuestra población. Anal Pediatria. 2020;92(2):88-93. doi: org/10.1016/j.anpedi.2019.02.002.
3. Lawrence AE, Gonzalez DO, Fallat ME, Aldrink JH, Hewitt GD, Hertweck SP, et al. Factors associated with management of pediatric ovarian neoplasms. Pediatrics. 2019;144(1):e20182537. doi: 10.1542/peds.2018-2537.
4. Gonzalo-Alonso E, Merino-Marcos I, Ferandez-Teijeiro Alvarez A, Astigarraga-Aguirre I, Navajas-Gutiérrez A. Ovarian tumors in childhood: apropos of a review of cases. An Esp Pediatr. 1998;49(5):491-494.
5. Hanafy AK, Mujtaba B, Yedururi S, Jensen CT, Sanchez R, Austin MT, et al. Imaging in pediatric ovarian tumors. Abdom Radiol. 2020;45(2):520-536. doi: 10.1007/s00261-019-02316-5.
6. Anthony EY, Caserta MP, Singh J, Chen MYM. Adnexal masses in female pediatric patients. AJR Am J Roentgenol. 2012;198(5):W426-431. doi: 10.2214/AJR.11.7920.
7. Madenci AL, Vandewalle RJ, Dieffenbach BV, Laufer MR, Boyd TK, Voss SD, et al. Multicenter pre-operative assessment of pediatric ovarian malignancy. J Pediatr Surg. 2019;54(9):1921-1925. doi: 10.1016/j.jpedsurg.2019.02.019.
8. Andreotti RF, Timmerman D, Strachowski LM, Froyman W, Benacerraf BR, Bennett GL, et al. O-RADS US risk stratification and management system: a consensus guideline from the ACR Ovarian-Adnexal Reporting and Data System Committee. Radiology. 2020;294(1):168-185. doi: 10.1148/radiol.2019191150.
9. Pi Y, Wilson MP, Katlariwala P, Sam M, Ackerman T, Paskar L, et al. Diagnostic accuracy and inter-observer reliability of the O-RADS scoring system among staff radiologists in a North American academic clinical setting. Abdom Radiol. 2021;46(10):4967-4973. doi: 10.1007/s00261-021-03193-7.
10. Solis-Cano DG, Cervantes-Flores HA, De Los Santos-Farrera O, Guzman-Martinez NB, Soria-Céspedes D. Sensitivity and specificity of ultrasonography using Ovarian-Adnexal Reporting and Data System classification versus pathology findings for ovarian cancer. Cureus. 2021;13(9):e17646. doi: 10.7759/cureus.17646.
11. Zhang Q, Dai X, Li W. Systematic review and meta-analysis of O-RADS ultrasound and O-RADS MRI for risk assessment of ovarian and adnexal lesions. AJR Am J Roentgenol. 2023;221(1):21-33. doi: org/10.2214/AJR.22.28396.
12. Lai H-W, Lyu G-R, Kang Z, Li L-Y, Zhang Y, Huang Y-J. Comparison of O-RADS, GI-RADS, and ADNEX for diagnosis of adnexal masses: an external validation study conducted by junior sonologists: an external validation study conducted by junior sonologists. J Ultrasound Med. 2022;41(6):1497-1507. doi: 10.1002/jum.15834.
13. Hack K, Gandhi N, Bouchard-Fortier G, Chawla TP, Ferguson SE, Li S, et al. External validation of O-RADS US risk stratification and management system. Radiology. 2022;304(1):114-120. doi: 10.1148/radiol.211868.
14. Basha MAA, Metwally MI, Gamil SA, Khater HM, Aly SA, El Sammak AA, et al. Comparison of O-RADS, GI-RADS, and IOTA simple rules regarding malignancy rate, validity, and reliability for diagnosis of adnexal masses. Eur Radiol. 2021;31(2):674-684. doi: 10.1007/s00330-020-07143-7.
15. Wang H, Wang L, An S, Ma Q, Tu Y, Shang N, et al. American College of Radiology Ovarian-Adnexal Reporting and Data System ultrasound (O-RADS): diagnostic performance and inter-reviewer agreement for ovarian masses in children. Front Pediatr 2023;11:1091735. doi: 10.3389/fped.2023.1091735.
16. Wu M, Huang L, Chen Y, Wang Y, Zhang M, Cao J, et al. Diagnostic accuracy of Ovarian-Adnexal Reporting and Data System, IOTA Simple Rules and Pediatric Risk of Malignancy Index for pediatric adnexal lesions: comparative study. Ultrasound Obstet Gynecol. 2025;66(3):361-367. doi: 10.1002/uog.29291.
17. Paltiel HJ, Phelps A. US of the pediatric female pelvis. Radiology. 2014;270(3):644-657. doi: 10.1148/radiol.13121724.
18. Phillips CH, Guo Y, Strachowski LM, Jha P, Reinhold C, Andreotti RF. The Ovarian/Adnexal Reporting and Data System for ultrasound: from standardized terminology to optimal risk assessment and management. Can Assoc Radiol J. 2023;74(1):44-57. doi: 10.1177/08465371221108057.
19. Adhikari L, Hassell LA. WHO classification. PathologyOutlines.com website. Available from: https://www.pathologyoutlines.com/topic/ovarytumorwhoclassif.html.

JMeXFRI

Journal of the Mexican Federation of Radiology and Imaging

Check for updates

FULL RESEARCH ARTICLE

Quantitative spectral CT parameters for predicting prostate cancer

Julia Oliva-Lozano[1,2], Emilia S. Tumbarello[1,2], Isolina Herraiz-Romero[1,2], Alvaro Navarro-Guzman[3], Claudia de Molina-Gomez[3] and Luis Concepcion-Aramendia[2]*

[1]Abdominal Radiology Section, Department of Radiology, Hospital General Universitario Dr. Balmis de Alicante; [2]Diagnostic Medical Imaging Research Group, Instituto de Investigacion Sanitaria y Biomedica de Alicante ISABIAL. Alicante; [3]Philips Healthcare, Madrid. Spain

ABSTRACT

Introduction: *The diagnostic performance of spectral computed tomography (CT) for predicting prostate cancer (PC) has not been sufficiently addressed. This study compared the spectral CT parameters of malignant and normal prostate tissue in men with biopsy-proven PC and defined the optimal cut-off values for predicting malignancy.* **Material and methods:** *This cross-sectional study included men with biopsy-proven clinically significant prostate cancer (csPC) who underwent prostate magnetic resonance imaging (MRI) and contrast-enhanced abdominopelvic spectral CT. Images were postprocessed. The diagnostic performance of the spectral CT parameters was assessed using receiver operating characteristic (ROC) analysis to determine thresholds for predicting malignant prostate lesions. The optimal threshold was defined using Youden's index. Sensitivity, specificity, accuracy, and area under the curve (AUC) were also determined.* **Results:** *We included 105 men with csPC. The mean age was 65.5 ± 6.1 years. Most patients (n = 97; 92.4%) showed PI-RADS lesions ≥ 3 on MRI. The optimal cut-off values for differentiating malignant lesions from normal prostate tissue were 137.8 Hounsfield units (HU) for low-energy virtual monoenergetic images (VMI) at 45 keV, 1.5 mg/mL for iodine concentration density (ICD), and 8.2 for Z-effective value. Accuracy was higher for post-processed spectral maps, including VMI at 45 keV (94.3%), ICD (94.3%), and Z-effective (94.3%), with greater discriminatory power than conventional CT reconstruction (91.7%).* **Conclusion:** *Our study showed that quantitative spectral CT parameters have high diagnostic performance with optimal cut-off values for accurately distinguishing malignant prostate lesions from normal prostate tissue in patients with csPC.*

Keywords: *Prostatic neoplasm. Diagnostic imaging. Multidetector computed tomography. Dual energy. Spectral computed tomography.*

INTRODUCTION

Prostate cancer (PC), one of the most prevalent male neoplasms, is difficult to assess with conventional computed tomography (CT). Precise diagnosis and classification are essential for timely management and prognosis of clinically significant prostate cancer (csPC)[1]. Multiparametric magnetic resonance imaging (MRI) is the gold standard for detecting and staging csPC. It integrates anatomical and functional data through the Prostate Imaging Reporting and Data System (PI-RADS). Current European Association of Urology (EAU) guidelines recommend pre-biopsy MRI in men with suspected organ-confined disease[1]. However, MRI availability, cost, long examination time, reader dependence, and, in some patients, contraindications limit its use.

Conventional CT provides limited soft-tissue contrast[2] and is used mainly for metastatic staging in csPC. To overcome these limitations, spectral CT has emerged

***Corresponding author:**
Julia Oliva-Lozano
E-mail: julia.olizano@gmail.com

Received for publication: 03-07-2025
Accepted for publication: 23-08-2025
DOI: 10.24875/JMEXFRI.M25000117

Available online: 15-01-2026
J Mex Fed Radiol Imaging. 2025;4(4):254-263
www.JMeXFRI.com

as an advanced quantitative technique that generates multiple post-processing datasets from a single multiple-energy acquisition[3-5]. Available multi-energy CT systems include dual-layer CT and photon-counting CT[6]. By using tissue-specific attenuation at different photon energies, spectral CT enables material decomposition and virtual monoenergetic image (VMI) reconstruction, improving contrast and tissue characterization. Low-energy VMI enhances iodine contrast sensitivity, while high-energy images reduce metallic artifacts.

The main clinical benefits of spectral CT include lesion detection and characterization through superior material differentiation, evaluation of tumor vascularity and perfusion, and the potential use of quantitative imaging biomarkers for treatment response[3-5]. However, the implementation of quantitative spectral CT parameters remains limited due to equipment-related variability[3,4] and insufficient validation studies. Evidence supporting the potential of spectral CT – particularly low-energy VMI – for diagnosing csPC is limited[7,8]. This study compared spectral CT parameters of malignant and normal prostate tissue in men with confirmed csPC and established optimal cut-off values for predicting malignancy.

MATERIAL AND METHODS

This cross-sectional study was conducted from July 2022 to May 2025 in the Abdominal Radiology Section of the Department of Radiology at the Dr. Balmis University General Hospital in Alicante, Spain. Men diagnosed with PC via transrectal biopsy, staged with MRI and spectral CT, and treated by radical prostatectomy were included. Patients lacking available images in PACS were excluded. The institutional ethics committee approved the study.

Study development and variables

Data were obtained from clinical records, including age, pre-surgery total prostate-specific antigen (PSA) level, PI-RADS score on MRI[9], Gleason score on prostatectomy specimen, and pathology TNM stage. csPC was defined by a Gleason score ≥3 + 4, a volume ≥0.5 cc, and/or invasive behavior[1].

Imaging acquisition and analysis protocol

Prostate MRI

MRI examinations were performed with an Ingenia Elition 3.0T scanner (Philips, Eindhoven, Netherlands). Patients fasted for 4-6 hours and underwent a micro-enema for rectal clearance before imaging. Hyoscine 10 mg was given orally or intravenously to reduce intestinal motion and associated susceptibility artifacts.

The imaging protocol followed multiparametric MRI (mpMRI) standards, including high-resolution T2-weighted imaging (WI) in axial, sagittal, and coronal planes and diffusion-weighted imaging (DWI) with apparent diffusion coefficient (ADC) mapping (axial plane; b-values 0, 1000, and 2000). In some cases, dynamic contrast-enhanced imaging was also acquired. Lesions were evaluated according to PI-RADS v2.1 criteria[9] by two abdominal and genitourinary imaging radiologists with 30 (IHR) and 3 years (JOL) of experience.

Spectral CT

Images were acquired with a spectral CT 7500 scanner (Philips, Eindhoven, Netherlands). Contrast-enhanced abdominopelvic spectral CT examination was performed 70 seconds after intravenous contrast administration (Iomeron 300 mg/mL) at 1.8 mg/kg of body weight using a pump injector at a rate of 2.5 mL/s. Other technical parameters included 2-mm slice thickness, 120 kV, 87 mA, and collimation of 128 × 0.625.

Manual regions of interest (ROIs) were placed over malignant hyper-enhancing prostate lesions on spectral CT maps and over normal prostate tissue based on MRI findings and prostatectomy specimen histological examination reports (Figure 1). The parameters included: a conventional map in Hounsfield units (HU); low-energy (45 keV) VMI in HU; an iodine concentration density (ICD) map in mg/mL; the Z-effective value; normalized HU on low-energy (45 keV) VMI, obtained by dividing the values of the hyper-enhancing lesion by those of the femoral artery; and normalized ICD, obtained by dividing the values of the hyper-enhancing lesion by those of the femoral artery.

Normalization to the femoral artery was performed to reduce the variability related to the contrast phase and intermanufacturer threshold variability[10]. Hyper-enhancing prostatic lesions on spectral CT were compared with PI-RADS ≥ 3 lesions and histological examination reports from prostatectomy specimens, to determine their location.

Statistical analysis

Malignant prostate lesions and normal prostate tissue were assessed in the same subject. The inference test

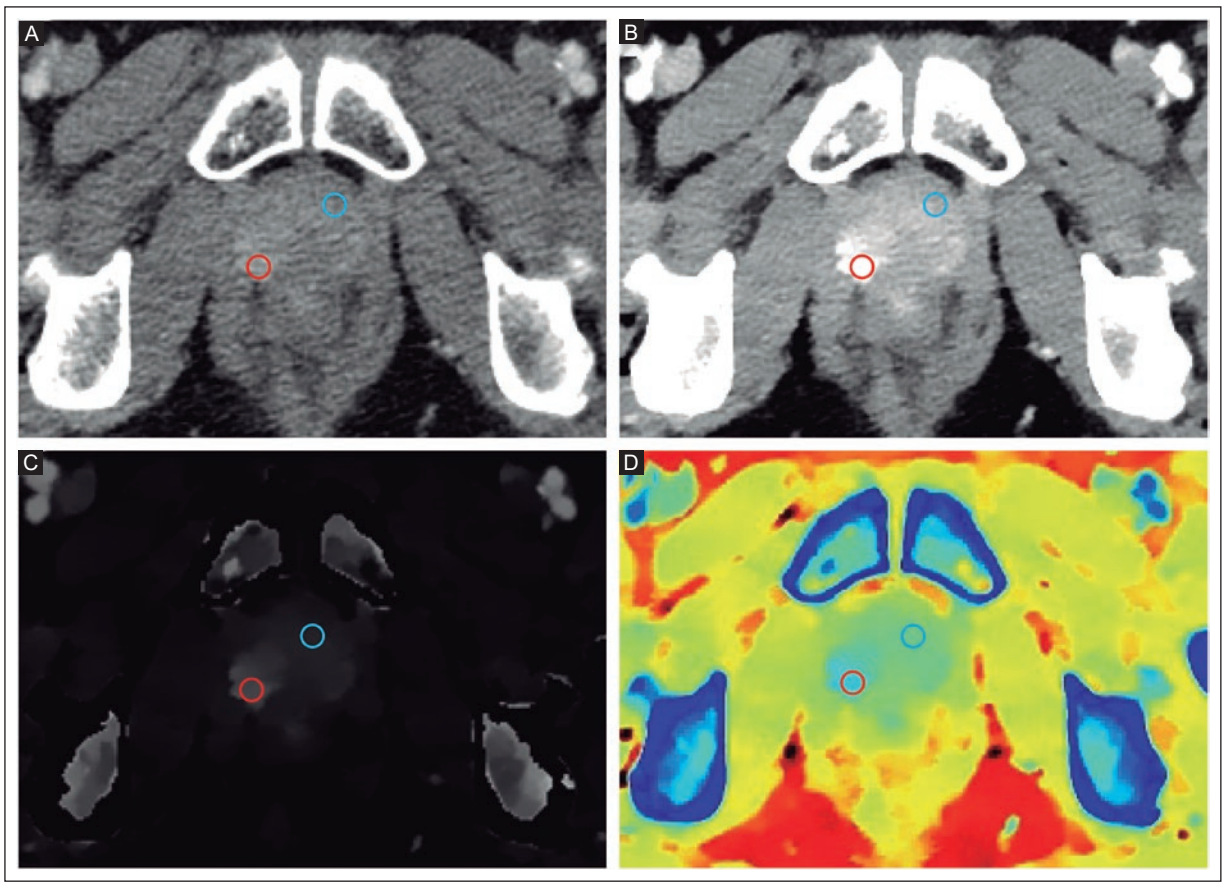

Figure 1. Manual regions of interest (ROIs) were placed on hyperenhancing malignant prostate lesions and on normal prostate tissue using spectral CT maps, guided by MRI findings and prostatectomy specimen histological examination. **A:** conventional spectral CT reconstruction, where PC (red circle) is not clearly visible and appears similar in density to adjacent normal tissue (blue circle). **B:** low-energy VMI at 45 keV, where PC appears hyperenhancing (red circle) in the peripheral zone of the right prostatic lobe compared to normal prostate tissue (blue circle). **C:** ICD map, where PC shows higher density (red circle) than normal tissue (blue circle). **D:** effective Z-map, where cancer shows a higher atomic number in blue (red circle).

CT: computed tomography; VMI: virtual monoenergetic imaging; keV: kiloelectronvolt; ICD: iodine concentration density; ROI: region of interest; PC: prostate cancer.

compared the proportions of detection in spectral CT and MRI using the McNemar test at a 5% significance level. Paired differences in spectral maps between normal prostate tissue and prostate cancer were analyzed with a paired *t*-test for normally distributed data or the Wilcoxon signed-rank test for non-normally distributed data, as determined by the Shapiro-Wilk test. A $p < 0.05$ was considered statistically significant. The diagnostic performance of spectral CT parameters was assessed using receiver operating characteristic (ROC) analysis to determine thresholds for predicting malignant prostate lesions. The optimal threshold was determined using Youden's index. Sensitivity, specificity, accuracy, and area under the curve (AUC) were calculated at this point. Bootstrap resampling (1,000 iterations with replacement) was used to estimate the 95% confidence intervals (CIs) for all metrics. Statistical analyses and figures were performed with Python version 3.10.5 (Python Software Foundation, Wilmington, DE, USA) and the associated libraries, NumPy, Pandas, SciPy, Scikit-learn, Matplotlib, and Seaborn.

RESULTS

We included 105 men with csPC with a mean age of 65.5 ± 6.1 years (Table 1). The mean total PSA before surgery was 11.9 ± 6.4 ng/mL. Most tumors were in the peripheral zone (n = 79, 75.2%). Most patients had PI-RADS lesions ≥ 3 on MRI (n = 97, 92.4%). The most common Gleason score after prostatectomy was 3 + 4 (n = 44, 41.8%), and most cases (n = 81, 77.2%) were classified as T2N0**.** The location of prostate cancer hyper-enhancing lesions on low-energy VMI at 45 keV of spectral CT correlated with MRI findings in 89.7% (n = 94) of the 105 cases. Figure 2 shows spectral CT and MRI findings in a man with csPC.

Table 1. Location, MRI PI-RADS score, Gleason score, and pathology staging of 105 patients with PC

Description	Parameter
Age (yrs), mean ± SD	65.5 ± 6.1
Total PSA (ng/mL), mean ± SD	11.9 ± 6.4
MRI lesion location, n (%)	
Peripheral zone	79 (75.2)
Transitional zone	19 (18.1)
Central zone	5 (4.8)
Peripheral zone + transitional zone	2 (1.9)
MRI PI-RADS score, n (%)	
1	2 (1.9)
2	6 (5.7)
3	17 (16.2)
4	38 (36.2)
5	42 (40.0)
Gleason score, n (%)	
3 + 3	9 (8.6)
3 + 4	44 (41.8)
3 + 5	1 (1.0)
4 + 3	30 (28.6)
4 + 4	8 (7.6)
4 + 5	8 (7.6)
5 + 3	4 (3.8)
5 + 4	1 (1.0)
TNM staging, n (%)	
T2N0	81 (77.2)
T3aN0	4 (3.8)
T3bN0	16 (15.2)
T3bN1	4 (3.8)

MRI: magnetic resonance imaging; PC: prostate cancer; PSA: prostate-specific antigen; PI-RADS: Prostate Imaging Reporting and Data System; TNM: Tumor, Node, Metastasis.

Comparison of spectral CT parameters of malignant prostate lesions and normal prostate tissue

Conventional and spectral CT parameters of malignant prostatic lesions and normal prostate tissue are shown in Figure 3. csPC exhibited significantly higher values than normal prostate tissue for all spectral CT parameters: HU on conventional reconstruction, HU on VMI at 45 keV, ICD, Z-effective value, normalized VMI at 45 keV, and normalized ICD ($p < 0.001$).

ROC analysis for optimal cut-off values to predict malignant prostate lesions

Table 2 shows the optimal cut-off for each spectral CT parameter used to differentiate normal prostate tissue (below the cut-off) from malignant prostate lesions (above the cut-off) with high sensitivity and specificity. The cut-off values for differentiating malignant prostate lesions from normal prostate tissue were 137.8 HU for low-energy VMI at 45 keV, 1.5 mg/mL for ICD, and 8.2 for Z-effective values.

Accuracy was higher for spectral post-processed maps, including VMI at 45 keV (94.3%, 95% CI 91.4-97.1), ICD (94.3 %, 95% CI 91.1-97.4), and Z-effective value (94.3%, 95% CI 91.1-97.4) showing greater discriminatory power than conventional reconstructions (91.7%, 95% CI 88.9-95.7). ROC analysis yielded a high AUC for cut-off thresholds differentiating malignant prostate lesions from normal prostate tissue for the spectral CT parameters studied (Figure 4).

Correlation between spectral CT parameters and MRI ADC values

There was no statistically significant correlation between the spectral CT parameters analyzed (normalized ICD and normalized HU at 45 keV VMI) and MRI ADC values. Figure 5 shows a scatter plot of these results, with points dispersion due to the lack of a relationship between these variables.

Normalized ICD and ADC values showed Pearson and Spearman correlations of 0.058 ($p = 0.607$) and 0.062 ($p = 0.578$), respectively. HU at low-energy VMI and ADC values showed Pearson and Spearman correlations of 0.169 ($p = 0.112$) and 0.146 ($p = 0.171$), respectively.

DISCUSSION

Our study demonstrates that quantitative spectral CT parameters show high diagnostic performance with optimal cut-off values for distinguishing malignant prostate lesions from normal tissue in patients with csPC. Spectral post-processed maps, particularly VMI at 45 keV, improve lesion visibility and support precise tissue characterization. These results highlight spectral CT as a useful adjunct to MRI and a potential alternative for patients with contraindications or incidental findings.

Although quantitative spectral CT thresholds have been proposed for cancer detection in various organs, the standardization of cut-off values is still under

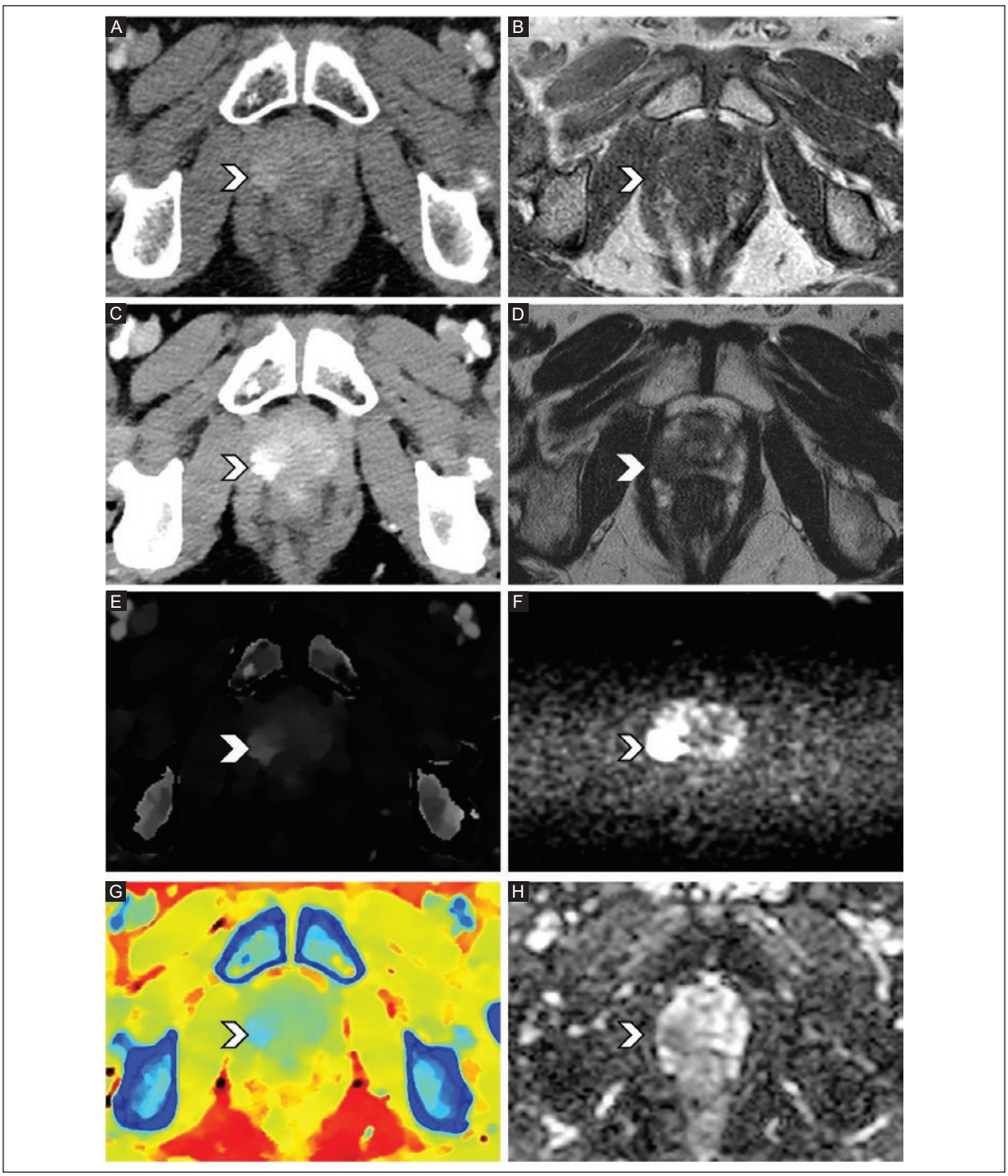

Figure 2. A 67-year-old man with elevated PSA (9.2 ng/mL), a family history of PC, and a recent diagnosis of csPC (Gleason score 4 + 4). **A:** conventional spectral CT reconstruction where PC is not clearly identified (arrowhead) and is similar in density to adjacent normal parenchyma. **B:** low-energy VMI at 45 keV, where PC is a hyperenhancing area (arrowhead) in the peripheral zone of the right prostate lobe, compared to normal parenchyma. **C:** ICD map where PC shows higher density (arrowhead) than normal tissue. **D:** effective Z-map where PC shows a higher atomic number in blue (arrowhead). Pelvic MRI sequences show a focal prostate lesion in the peripheral zone of the right lobe. **E:** T1-WI, where PC (arrowhead) is indistinguishable from normal prostate tissue. **F:** T2-WI, where the lesion appears as a focal hypointense area (arrowhead). **G:** DWI, where a high signal is evident (arrowhead). **H:** ADC map shows a marked low signal corresponding to csPC, confirming diffusion restriction (arrowhead). Taken together, the T2, DWI, and ADC findings are consistent with a PI-RADS of 5, suggesting csPC.

PSA: prostate-specific antigen; CT: computed tomography; VMI: virtual monoenergetic imaging; keV: kiloelectronvolt; ICD: iodine concentration density; MRI: magnetic resonance imaging; WI: weighted image; DWI: diffusion-weighted imaging; csPC: clinically significant prostate cancer; PI-RADS: Prostate Imaging Reporting and Data System; PC: prostate cancer.

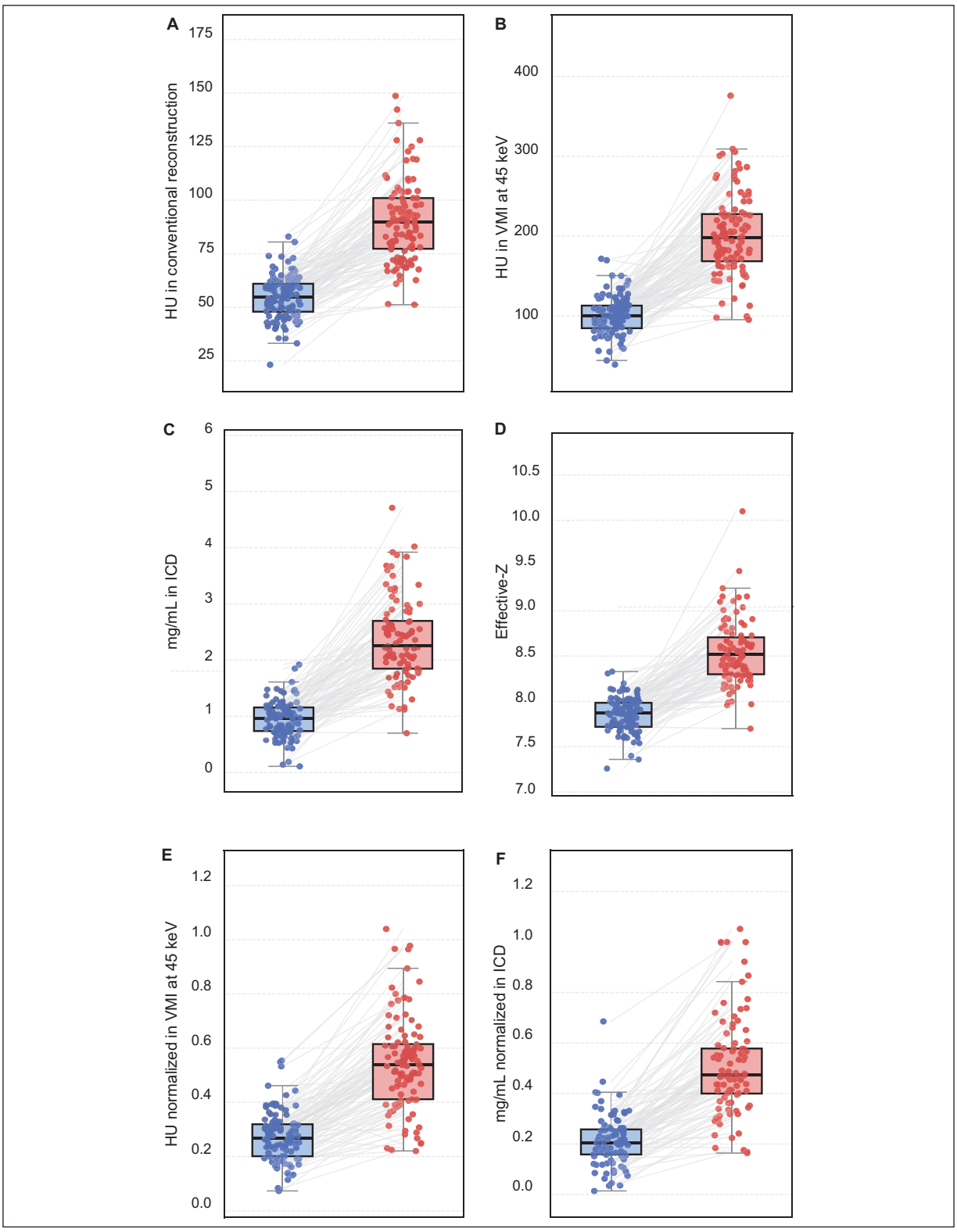

Figure 3. Spectral CT parameters for normal prostatic tissue (blue) and PC (red). **A:** HU in conventional reconstruction; **B:** HU in VMI at 45 keV; **C:** ICD map, mg/mL; **D:** effective Z; **E:** HU in VMI at 45 keV normalized to the femoral artery; **F:** ICD normalized to the femoral artery. The boxes show the interquartile range (IQR, Q1-Q3), the center line is the median, and the whiskers extend to 1.5 times the IQR. Data beyond this range are outliers. All distributions have higher values in PC than in normal tissue.

CT: computed tomography; HU: Hounsfield units; VMI: virtual monoenergetic imaging; keV: kiloelectronvolt; ICD: iodine concentration density; IQR: interquartile range; PC: prostate cancer.

Table 2. Diagnostic performance and cut-off values of spectral CT parameters for predicting malignant prostate lesions

Parameter	Cut-off values[a]	Sensitivity (95% CI)	Specificity (95% CI)	Accuracy (95% CI)	AUC (95% CI)
HU on conventional CT reconstruction	68.5	90.4 (86.5-98.1)	93.3 (85.0-97.3)	91.7 (88.9-95.7)	0.968 (0.945-0.987)
Spectral CT post-processed maps					
HU on VMI at 45 keV	137.8	94.3 (87.6-98.1)	94.3 (90.8-99.2)	94.3 (91.4-97.1)	0.973 (0.952-0.991)
ICD, mg/mL	1.5	91.7 (86.0-96.7)	96.9 (91.9-100)	94.3 (91.1-97.4)	0.973 (0.950-0.991)
Z-effective value	8.2	91.7 (86.4-97.0)	97.4 (92.0-100)	94.3 (91.1-97.4)	0.974 (0.950-0.991)
VMI at 45 keV[b]	0.39	82.9 (75.5-92.9)	92.4 (83.8-98.1)	87.1 (83.8-91.9)	0.927 (0.891-0.959)
ICD[b]	0.34	85.4 (78.4-96.8)	91.7 (80.8-97.9)	88.0 (84.9-93.2)	0.939 (0.903-0.969)

[a]Values above these thresholds predict malignant prostate lesions. [b]HU and ICD were normalized to the femoral artery.
CT: computed tomography; CI: confidence interval; AUC: area under the curve; HU: Hounsfield units; VMI: virtual monoenergetic images; keV: kiloelectronvolt; ICD: iodine concentration density.

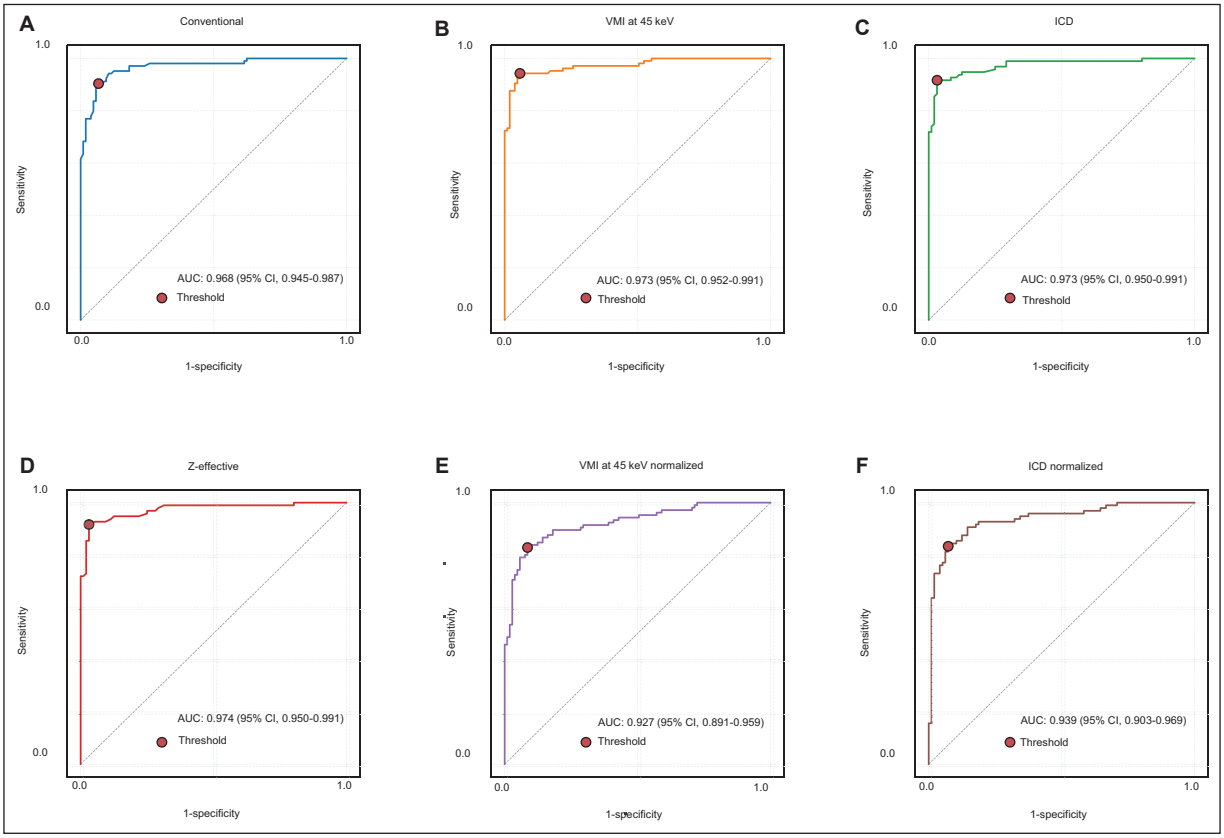

Figure 4. ROC curves of spectral CT parameters for predicting PC. **A:** conventional reconstruction; **B:** VMI at 45 keV; **C:** ICD; **D:** Z-effective; **E:** HU normalized at VMI at 45 keV; **F:** normalized ICD. AUC and optimal threshold points are shown for each parameter. VMI at 45 keV, ICD, and effective Z-value had the highest AUC values and strong discriminative performance.

ROC: receiver operating characteristic; CT: computed tomography; VMI: virtual monoenergetic imaging; ICD: iodine concentration density; keV: kiloelectronvolt; HU: Hounsfield units; AUC: area under the curve; PC: prostate cancer.

development, and must be interpreted in the clinical context[11-13]. Chen et al.[8] evaluated spectral CT in differentiating bladder cancer from benign prostatic hyperplasia (BPH) in a retrospective study of 118 patients. Spectral CT enabled quantitative assessment of CT attenuation values across a range of energies (40-140 keV), spectral HU curve slopes, and effective atomic numbers with significant differences between

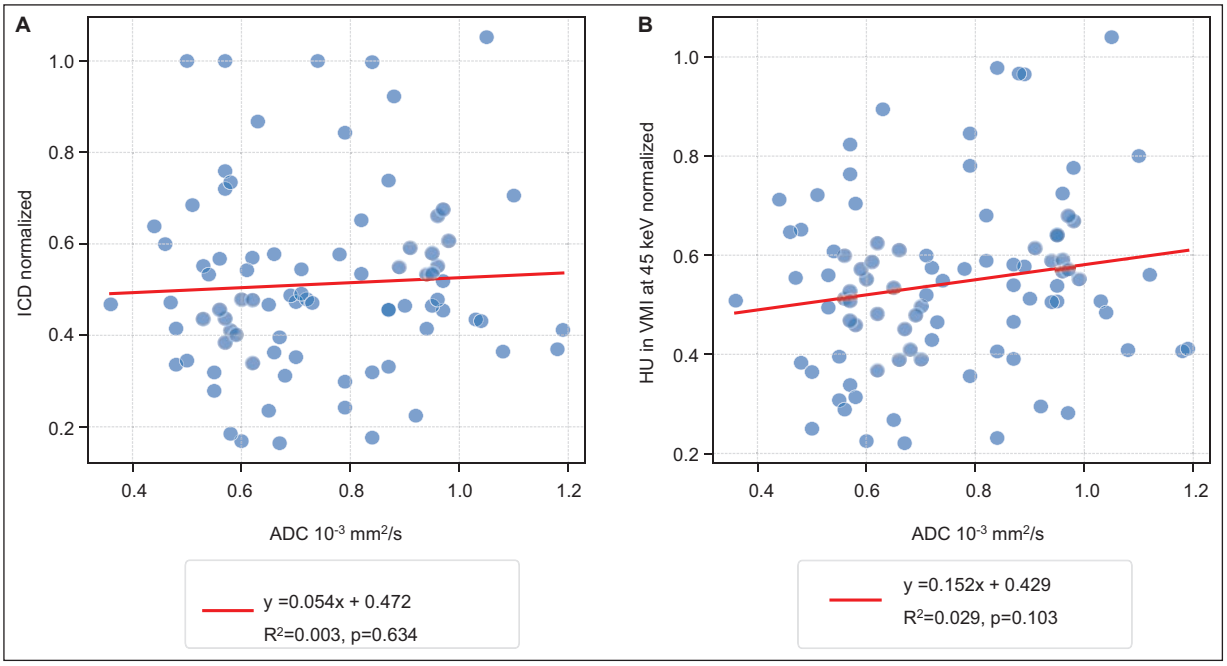

Figure 5. Correlation between MRI ADC values of PC and ICD and HU in VMI at 45 keV, each normalized for the femoral artery. **A:** ADC value ($\times 10^{-3}$ mm²/s) vs. normalized ICD (linear fit: y = 0.054× + 0.472), showing a weak, non-significant correlation (R^2 = 0.003; p = 0.634). **B:** ADC value ($\times 10^{-3}$ mm²/s) vs. normalized HU in VMI at 45 keV (linear fit: y = 0.152× + 0.429) showing a slight non-significant positive trend (R^2 = 0.029; p = 0.103). In both graphs, each point represents a confirmed PC. There was no significant correlation between ADC and spectral CT parameters.

ADC: apparent diffusion coefficient; ICD: iodine concentration density; HU: Hounsfield units; MRI: magnetic resonance imaging; VMI: virtual monoenergetic imaging; PC: prostate cancer.

bladder cancer and BPH, especially at 40 keV VMI, where bladder cancer showed higher values and effective atomic numbers. Klein et al.[14] investigated the correlation between quantitative dual-energy CT parameters and MRI-derived biomarkers in invasive ductal breast carcinoma and found correlations between CT perfusion parameters and tumor immunohistochemical subtypes, suggesting spectral CT can capture functionally relevant tumor features. However, its clinical application requires further validation. Our study found strong correlations between spectral CT parameters and csPC identified on MRI. We established cut-off values for spectral CT parameters that differentiate malignant and normal prostatic tissue with high sensitivity and specificity. The 45 keV VMI threshold of 137.8 HU was the most accurate, with high sensitivity (94.3%) and specificity (94.3%), reinforcing its value as the key parameter for detecting csPC suspicious lesions. While spectral CT does not replace MRI for definitive diagnosis, it may improve lesion conspicuity and support incidental or adjunctive csPC detection.

PC typically shows lower ADC MRI values than normal or benign tissue[15-17]. Li et al.[18] compared spectral CT with DWI MRI for predicting neoadjuvant chemotherapy response in locally advanced gastric cancer. They found comparable performance for both modalities, with improved performance when combined. In our study, spectral CT parameters and ADC values showed a weak, non-significant correlation with normalized ICD and a slight positive trend with normalized HU at 45 keV VMI. Although ADC MRI remains a validated biomarker of PC aggressiveness, spectral CT cannot replicate this functional information, indicating that CT cannot substitute diffusion-based MRI in intraprostatic characterization[19].

Transitional zone PC is difficult to distinguish from hyperplastic adenomas[19], while peripheral zone lesions are challenging to differentiate from prostatitis[20]. BPH-related heterogeneity further limits diagnostic specificity. Korevaar et al.[2] showed that although conventional CT lacks soft-tissue contrast, machine-learning analysis can extract latent features that improve csPC detection. This finding supports the diagnostic value of spectral CT, though its performance remains inferior to multiparametric MRI, particularly for localization and staging. Although we did not analyze spectral parameters separately in the peripheral and transitional zones,

we found that transitional zone cancers closely resembled hyperplastic adenomas. In addition, the nodule capsule – important for PI-RADS assessment – could not be evaluated on conventional or spectral CT, but it can be evaluated on MRI to determine the degree of malignancy. Spectral CT may offer greater specificity in the peripheral zone, but transitional zone adenomas and malignant lesions remain difficult to differentiate.

The strengths of this study are its systematic design, the inclusion of patients with confirmed PC, and the quantitative evaluation of spectral CT parameters from post-processed maps, which yielded consistent, reproducible results. The standardized image acquisition protocol strengthened methodological rigor and internal validity. Limitations include the single-center design, which may affect generalizability, and a unique spectral CT equipment, which may lead to variations in image quality, reconstruction algorithms, and quantitative parameter measurements across systems of different manufacturers; and retrospective ROI selection may introduce bias, as ROIs were manually drawn on previously MRI-identified lesions. Measuring HU on conventional maps in areas already known to be malignant could have optimized diagnostic performance, reducing the difference observed with spectral CT. Another limitation is the lack of a healthy control group, as comparisons were restricted to malignant lesions versus normal prostate tissue in the same patient.

CONCLUSION

Our study found that quantitative spectral CT parameters effectively distinguished malignant from normal tissue and accurately predicted csPC. The high sensitivity and specificity of the optimal cut-offs support spectral CT's potential as complementary to MRI, especially for patients with contraindications or incidental prostate abnormalities. However, MRI remains the reference standard for accurate PC detection, localization, and risk stratification. Multicenter studies with larger cohorts are needed to validate these cut-off values and assess the reproducibility of different scanners and populations. Including a healthy control group would allow for more robust comparisons.

Acknowledgment

The authors thank Professor Ana M. Contreras-Navarro for her guidance in preparing and writing this scientific paper.

Funding

The authors declare that the research foundation of the *Instituto de Investigación Sanitaria y Biomédica de Alicante*, ISABIAL, supported this research.

Conflicts of interest

A. Navarro-Guzman and C. de Molina-Gomez are employees of Philips Healthcare Company. They conducted the statistical analysis for the study. The other authors declare no conflicts of interest.

Ethical considerations

Protection of humans and animals. This study complied with the Declaration of Helsinki (1964) and subsequent amendments.

Confidentiality, informed consent, and ethical approval. The authors declare they followed their center's protocol for sharing patient data. Informed consent was not required for this observational study of information collected during routine clinical care.

Declaration on the use of artificial intelligence. The authors did not use generative artificial intelligence to prepare this manuscript and/or create tables, figures, or figure legends.

REFERENCES

1. Cornford P, van der Bergh RCN, Briers E, van der Broeck, Brunckhorst O, Darraugh J, et al. EAU-EANM-ESTRO-ESUR-ISUP-SIOG Guidelines on Prostate Cancer - 2024 Update. Part I: Screening, Diagnosis, and Local Treatment with Curative Intent. Eur Urol. 2024. 86(2):148-163. doi: 10.1016/j.eururo.2024.03.027.
2. Korevaar S, Tennakoon R, Page M, Brotchie P, Thangarajah J, Florescu C, et al. Incidental detection of prostate cancer with computed tomography scans. Sci Rep. 2021;11:7956. doi: 10.1038/s41598-021-86972-y.
3. García-Figueiras R, Baleato-González S. Quantitative multi-energy CT in oncology: State of the art and future directions. Eur J Radiol. 2025;182: 111840. doi: 10.1016/j.ejrad.2024.111840.
4. García-Figueiras R, Oleaga L, Broncano J, Tardáguila G, Fernández-Pérez G, Vañó, et al. What to Expect (and What Not) from Dual-Energy CT Imaging Now and in the Future? J Imaging. 2024;10(7):154. doi.org/10.3390/jimaging10070154.
5. Greffier J, Villani N, Defez D, Dabli D, Si-Mohamed S. Spectral CT imaging: technical principles of dual-energy CT and multi-energy photon-counting CT. Diagn Interv Imaging. 2023;104(4):167-177. doi: 10.1016/j.diii.2022.11.003.
6. Philips Healthcare. Spectral CT 7500: User Manual. Koninklijke Philips N.V.; 2021.
7. Fan N, Chen X, Li Y, Zhu Z, Chen X, Yang Z, et al. Dual-energy computed tomography with new virtual monoenergetic image reconstruction enhances prostate lesion image quality and improves the diagnostic efficacy for prostate cancer. BMC Med Imaging. 2024;24(1):212. doi: 10.1186/s12880-024-01393-3.
8. Chen A, Liu A, Liu J, Tian S, Wang H, Liu Y. Application of dual-energy spectral CT imaging in differential diagnosis of bladder cancer and benign prostate hyperplasia. Medicine. 2016;95(52):e5705. doi: 10.1097/MD.0000000000005705.
9. Turkbey B, Rosenkrantz AB, Haider MA, Padhani AR, Villeirs G, Macura KJ, et al. prostate imaging reporting and data system Version 2.1: 2019 Update of prostate imaging reporting and data system Version 2. Eur Urol. 2019;76(3):340-351. doi: 10.1016/j.eururo.2019.02.033.

10. Patel BN, Vernuccio F, Meyer M, Godwin B, Rosenberg M, Rudnick N, et al. Dual-Energy CT material density iodine quantification for distinguishing vascular from nonvascular renal lesions: normalization reduces intermanufacturer threshold variability. AJR Am J Roentgenol. 2019; 212(2):366-376. doi:10.2214/AJR.18.20115.
11. Zhu Q, Sun J, Zhu W, Chen W, Ye J. Spectral CT imaging versus conventional CT post-processing technique in differentiating malignant and benign renal tumors. Br J Radiol. 2023;96(1151):20230147. doi: 10.1259/bjr.20230147.
12. Wang X, Liu D, Zeng X, Jiang S, Li L, Yu T, et al. Dual-energy CT quantitative parameters for the differentiation of benign from malignant lesions and the prediction of histopathological and molecular subtypes in breast cancer. Quant Imaging Med Surg. 2021;11(5):1946-1957. doi: 10.21037/qims-20-825.
13. Jacobsen MC, Cressman ENK, Tamm EP, Baluya DL, Duan X, Cody DD, et al. Dual-energy CT: lower limits of iodine detection and quantification. Radiology. 2019;292(2):414-419. doi: 10.1148/radiol.2019182870.
14. Klein K, Schafigh DG, Schömig-Markiefka B, Campbell GM, Weiss K, Malter W, et al. Intermodal correlation of quantitative CT-data and MRI-biomarkers derived from synchronous spectral CT-maps and breast MRI-examinations with molecular biomarkers in invasive ductal breast carcinomas. Eur J Radiol. 2023;165:110919. doi: 10.1016/j.ejrad.2023.110919.
15. De Cobelli F, Ravelli S, Esposito A, Giganti F, Gallina A, Montorsi F, et al. Apparent diffusion coefficient value and ratio as noninvasive potential biomarkers to predict prostate cancer grading: comparison with prostate biopsy and radical prostatectomy specimen. AJR Am J Roentgenol. 2015;204(3):550-557. doi: 10.2214/AJR.14.13146.
16. Buss A, Radzina M, Liepa M, Birkenfelds E, Saule L, Miculis K, et al. Role of apparent diffusion coefficient value and apparent diffusion coefficient ratio as prognostic factors for prostate cancer aggressiveness. Diagnostics (Basel). 2024;14(21):2438. doi: 10.3390/diagnostics14212438.
17. Hambrock T, Somford DM, Huisman HJ, van Oort IM, Witjes JA, de Kaa CAH-V, et al. Relationship between apparent diffusion coefficients at 3.0-T MR imaging and gleason grade in peripheral zone prostate cancer. Radiology. 2011;259(2)453-461. doi:10.1148/radiol.11091409.
18. Li J, Xu S, Wang Y, Ma F, Chen X, Qu J. Spectral CT vs. diffusion-weighted imaging for the quantitative prediction of pathologic response to neoadjuvant chemotherapy in locally advanced gastric cancer. Eur Radiol. 2024;34(9):6193-6204. doi: 10.1007/s00330-024-10642-6.
19. Hötker AM, Mazaheri Y, Aras Ö, Zheng J, Moskowitz CS, Gondo T, et al. Assessment of prostate cancer aggressiveness by use of the combination of quantitative DWI and dynamic contrast-enhanced MRI. Am J Roentgenol. 2016;206(4):756-763. doi:10.2214/AJR.15.14912.
20. Huang G, Lebovic G, Vlachou PA. Diagnostic value of CT in detecting peripheral zone prostate cancer. AJR Am J Roentgenol. 2019;213(4): 831-835. doi: 10.2214/AJR.18.21013.

JMeXFRI

Journal of the Mexican Federation of Radiology and Imaging

Check for updates

FULL RESEARCH ARTICLE

Comparison of three noninvasive quantitative MRI-based methods for estimating liver steatosis

Jorge A. Flores-Ramos[1,2,3], J. Eduardo Valencia-Segura[1], Gerardo Negrete-Granados[3] and Arturo Hernandez-Medina[1,4]*

[1]Department of Magnetic Resonance Imaging, Hospital Angeles Lomas, Huixquilucan, State of Mexico; [2]Department of Radiology, Faculty of Medicine, Universidad Autonoma de Queretaro; [3]Department of Radiology, Hospital H+; [4]Biomedical Engineering Area, Faculty of Engineering, Universidad Autonoma de Queretaro. Queretaro, Queretaro. Mexico

ABSTRACT

Introduction: *Magnetic resonance imaging-proton density fat fraction (MRI-PDFF) has been validated for diagnosing liver steatosis. However, comparisons of MRI-based methods have not been sufficiently addressed. This study compared three noninvasive quantitative MRI methods for evaluating liver steatosis and assessed the correlations between body mass index (BMI) and abdominal circumference with liver fat in Mexican patients.* **Material and methods:** *This cross-sectional study included adults without a prior clinical or laboratory diagnosis of liver disease. Liver fat was quantified using LiverLab software with three MRI-based methods: automatic MRI-PDFF segmentation of the entire liver, manual MRI-PDFF ROI, and magnetic resonance spectroscopy of fat fraction (MRS-FF).* **Results:** *Forty-one participants with a mean age of 40.6 ± 13.7 years were included; 21 (51.2%) were men, and 20 (48.8%) were women. The mean BMI was 27.1 ± 4.6 kg/m². The prevalence of hepatic steatosis was 43.9% (n = 18). The median liver steatosis for automatic MRI-PDFF segmentation was 5.0% (IQR 6.4%); for MRI-PDFF ROI, 2.9% (IQR 6.9%), and for MRS-FF, 5.7% (IQR 8.4%), with a significant difference (p = 0.006). Liver volume was positively correlated with BMI (r = 0.50; p < 0.001); a higher BMI was associated with greater liver volume. Abdominal circumference was positively correlated with the liver fat fraction (r = 0.46, p = 0.001).* **Conclusion:** *Automated MRI-PDFF segmentation and MRS-FF showed comparable results for quantifying liver fat, while MRI-PDFF ROI yielded significantly lower values. Liver steatosis correlated directly with higher BMI and larger abdominal circumference. This is the first study in Mexican patients to report liver fat estimation using three MRI-based methods.*

Keywords: *Magnetic resonance imaging. Liver steatosis. Metabolic dysfunction-associated steatotic liver disease. LiverLab.*

INTRODUCTION

Liver steatosis is a public health problem. Metabolic dysfunction-associated steatotic liver disease (MASLD, formerly MAFLD or NAFLD), the current term for this condition[1], is the most common chronic liver disease in the world[2]. The prevalence of liver steatosis in the Mexican population has been estimated at 42.5%[3,4]. The clinical spectrum of MASLD includes steatosis, steatohepatitis, and liver fibrosis, which can progress to liver failure or hepatocellular carcinoma[5,6]. Liver steatosis remains a challenging diagnosis. Liver biopsy, considered the gold standard, has disadvantages due to its invasive nature and sampling bias, limiting evaluation because of the heterogeneity of fat in liver parenchyma[7].

Magnetic resonance imaging (MRI) and elastography are noninvasive alternatives with good accuracy[8]. MRI-based methods include MRI proton density fat fraction (MRI-PDFF), elastography, and

***Corresponding author:**
J. Eduardo Valencia-Segura
E-mail: eduardo.valencia@saludangeles.mx

Received for publication: 10-07-2025
Accepted for publication: 29-08-2025
DOI: 10.24875/JMEXFRI.M25000118

Available online: 15-01-2026
J Mex Fed Radiol Imaging. 2025;4(4):264-272
www.JMeXFRI.com

magnetic resonance spectroscopy of fat fraction (MRS-FF). MRI-PDFF has been validated for diagnosing steatosis using two fat quantification methods: whole-liver automatic segmentation and manual region-of-interest (ROI). Manual ROI is user-dependent, and there is a difference in accuracy between the two methods[9].

Anthropometric parameters such as body mass index (BMI) and abdominal circumference are diagnostic criteria for MASLD[8,10]. Steatotic liver disease is associated with metabolic dysfunction, and abdominal adiposity is an important feature in the development of MASLD[11]. This study compared three noninvasive quantitative MRI-based methods for evaluating liver steatosis in Mexican patients and assessed the correlation between BMI and abdominal circumference with liver fat. The MRI methods were automatic segmentation of the entire liver volume with MRI-PDFF, manual MRI-PDFF ROI, and MRS-FF.

MATERIAL AND METHODS

This cross-sectional study was conducted from August to November 2024 in the Magnetic Resonance Department of Hospital Angeles Lomas, Huixquilucan, State of Mexico, Mexico. Adults aged 18 years or older referred for an MRI of other body regions with no known clinical or laboratory diagnosis of liver disease were included. Patients with focal liver lesions, hepatic or extrahepatic neoplasia, contraindications for MRI (such as metallic implants or claustrophobia), incomplete MRI studies, or studies with artifacts or interference affecting the accuracy of automated liver segmentation were excluded. All participants provided written informed consent. The Institutional Research Ethics and Research Committees approved this study.

Development and study variables

Age, sex, comorbidities such as type 2 diabetes and systemic arterial hypertension, BMI (kg/m²), and waist circumference (cm) were recorded. MRI liver fat fraction parameters were expressed as percentages using three methods: automatic MRI-PDFF segmentation, MRI-PDFF ROI, and MRS-FF.

Liver steatosis grading

Liver steatosis was graded according to proton density fat fraction (PDFF) thresholds validated in an independent biopsy-based cohort reported by Tang et al.[12]: Grade 1, PDFF ≥ 6.4%; Grade 2, PDFF ≥ 17.4%, and Grade 3, PDFF ≥ 22.1%. Histological severity was established using the NASH CRN system[13]. The PDFF cut-off points showed high specificity with moderate to high sensitivity for the dichotomized classification of the three grades. These thresholds were estimated using multi-echo MRI sequences with T2* correction (q-Dixon) sequences, which are recommended for noninvasive steatosis classification.

Imaging acquisition protocol

Liver MRI was performed with a 1.5T MAGNETOM Aera scanner (Siemens Healthineers, Erlangen, Germany) with an 18-channel abdominal coil. Conventional T2-weighted sequences were acquired in coronal, sagittal, and axial planes. All images were acquired during a single breath-hold to minimize motion artifacts. LiverLab software (Siemens Healthineers, Erlangen, Germany) was used with the following three sequences (Table 1): T1 VIBE e-Dixon (First Look Dixon), T1 VIBE q-Dixon (multi-echo Dixon), and single-voxel HISTO spectroscopy (Figure 1). The T1 VIBE e-Dixon sequence generated a four-image series (in-phase, out-of-phase, water-only, and fat-only) with total coverage of the liver parenchyma (at least 3 cm above and below its borders).

The system performed automated online liver segmentation and generated a 20 mm region of interest (ROI), which was manually positioned by technical staff under the supervision of a radiologist (EVS) with five years of experience and a radiologist (JFR) with two years of experience in body MRI. The ROI was manually placed in segment VII, free of blood vessels. Subsequently, the T1 VIBE q-Dixon sequence was used for liver fat quantification. The HISTO MRS-FF sequence, based on STEAM (Stimulated Echo Acquisition Mode) spectroscopy, was acquired during a single 15 second breath-hold with a 30 mm³ voxel placed at the same ROI site (segment VII).

Post-processing and data analysis

Post-processing was performed immediately after image acquisition using LiverLab software tools. The T1 VIBE q-Dixon sequence provided quantitative fat fraction maps for both automatic segmentation and manual ROI; fat fraction was calculated by MRI-PDFF (Figure 2). The HISTO map calculated the transverse relaxation (T2) corrected fat fraction by spectroscopy (MRS-FF), represented by color bars. Liver fat quantification was recorded in a database directly from the software-generated report.

Table 1. 1.5T MRI protocol with three main sequences for quantification of liver fat by multiparametric assessment using LiverLab software

Sequence	FOV/voxel size (mm)	Matrix	TR (ms)	TE (ms)	Slice thickness/gap (mm)
T1 VIBE e-Dixon	308.8*380/1.2*1.2*3.0	195*320	6.69	2.39, 4.77	3.0/3.6
T1 VIBE q-Dixon	450*393.8/1.4*1.4*3.5	111*160	15.6	2.38, 4.76, 7.14, 9.52, 11.90, 14.28	3.5/4.2
HISTO spectroscopy	30*30*30	-	3000	12, 24, 36, 48, 72	30

T: tesla; MRI: magnetic resonance imaging; T1-weighted image; VIBE: volumetric interpolated breath-hold examination; FOV: field-of-view; TR: time repetition; TE: time echo; ms: milliseconds; mm: millimeters.

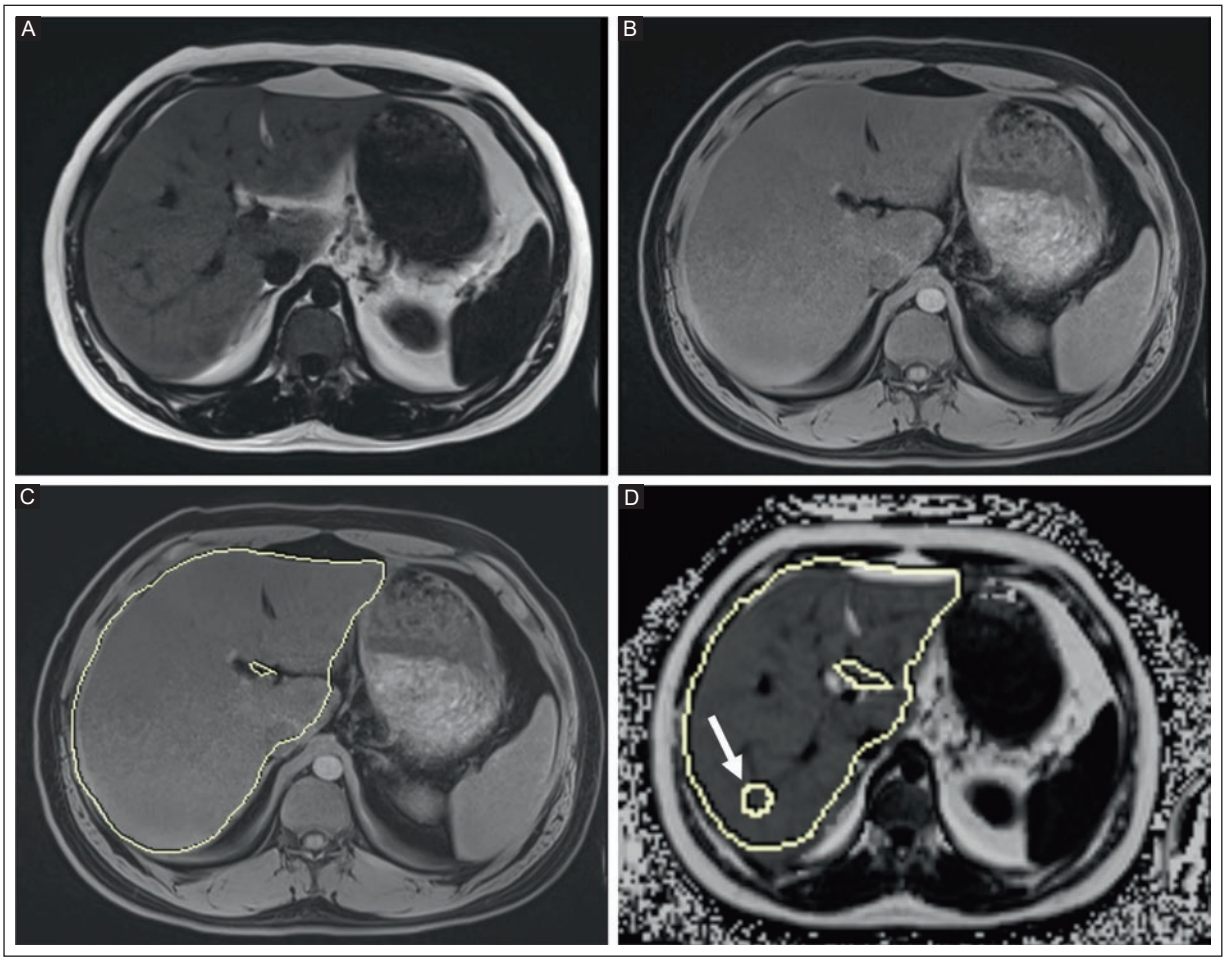

Figure 1. T1 VIBE e-Dixon or First Look Dixon sequence 3D acquisition performed with a single breath-hold with full coverage of the entire hepatic parenchyma, generating the following images: water, fat, and automatic segmentation on water. **A:** T1 VIBE Dixon Fat shows the macroscopic fat component of tissues without free water protons. This component appear isointense. **B:** T1 VIBE Dixon Water shows the free water component without the macroscopic fat component; free water protons appear isointense. **C:** T1 VIBE e-Dixon sequence with automatic MRI-PDFF segmentation performed after acquisition. **D:** T1 VIBE Dixon Fat Fraction. After acquisition, the system automatically performs liver MRI-PDFF segmentation, and a manual ROI approximately 20 mm in size is placed over the hepatic parenchyma, standardized to hepatic segment VII (arrow).

VIBE: volumetric interpolated breath-hold examination; MRI-PDFF: magnetic resonance imaging-proton density fat fraction; ROI: region of interest.

Statistical analysis

Results were expressed as means, standard deviations (SD), medians, and interquartile range (IQR). Descriptive statistics summarized quantitative variables, including measures of central tendency. Qualitative variables were summarized as frequency and percentage. The liver fat percentage, BMI, and abdominal circumference were assessed with Pearson's

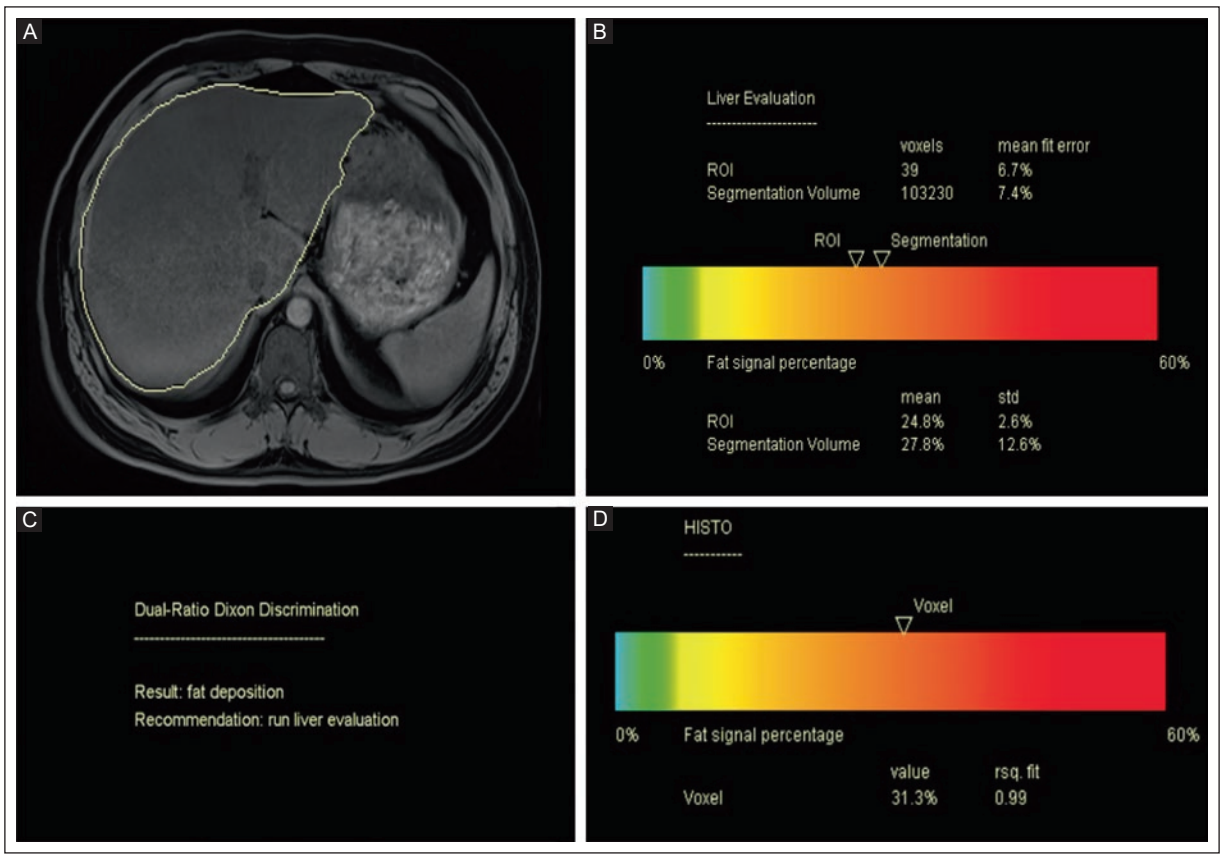

Figure 2. MRI quantification of liver fat using LiverLab software. **A:** T1 VIBE e-Dixon sequence with automatic MRI-PDFF segmentation performed by the software after acquisition. **B:** dual-Ratio Dixon Discrimination. The system generates a result from the segmented liver tissue, recommending whether to perform liver q-Dixon evaluation, based on the measured fat deposition. **C:** liver evaluation report displayed as a color bar using PDFF, showing the liver fat fraction obtained by automatic MRI-PDFF segmentation (27.8% ± 12.6%) and manual MRI-PDFF ROI (24.8% ± 2.6%). The number of voxels occupied by the ROI and the segmentation are shown. **D:** HISTO report displayed as a color bar by spectroscopy (MRS-FF) showing the liver fat fraction (31.3% ± 0.99%).

VIBE: volumetric interpolated breath-hold examination; MRI-PDFF: magnetic resonance imaging-proton density fat fraction; MRS-FF: magnetic resonance spectroscopy-fat fraction; ROI: region of interest; PDFF: proton density fat fraction.

correlation coefficient. The Mann-Whitney U test was used to compare segmentation quality (optimal vs. suboptimal) and sex. Statistical significance was a p-value < 0.05. RkWard v0.8.0 software was used for the analysis[14].

RESULTS

Forty-six patients underwent liver MRI; five were excluded due to SWAP artifact (uncorrectable fat-water exchange), leaving forty-one participants. The mean age was 40.6 ± 13.7 years (Table 2); 21 (51.2%) were men and 20 (48.8%) were women. The mean BMI was 27.1 ± 4.6 kg/m²; 24.5% (n = 10) were normal weight; 51.2% (n = 21) were overweight; 21.9% (n = 9) were obese; and 2.4% (n = 1) were underweight. The mean abdominal circumference was 93.2 ± 16.5 cm. Among participants, 4.9% (n = 2) had type 2 diabetes and 9.8% (n = 4) had hypertension. The prevalence of liver steatosis was 43.9% (n = 18 of 41); 11 (61.1%) were men, and 7 (38.9%) were women. Liver steatosis was quantified by automatic MRI-PDFF segmentation: 88.9% (n = 16) were grade 1, 5.6% (n = 1) were grade 2, and 5.6% (n = 1) were grade 3.

Quality of liver fat segmentation by MRI-PDFF

Optimal segmentation was observed in 85.4 % (n = 35) of MRI scans (Figure 3A), with no significant difference in fat percentage between optimal and suboptimal segmentation. The median difference with optimal segmentation did not change the proportion of cases above the PDFF threshold or the distribution of the three grades of liver steatosis.

Table 2. Characteristics and prevalence of liver steatosis in 41 patients assessed by MRI

Description	Parameter
Age (years), mean ± SD	40.6 ± 13.7
Sex, n (%)	
Men	21 (51.2)
Women	20 (48.8)
BMI (kg/m²), mean ± SD	27.1 ± 4.6
BMI classification, n (%)	
Underweight	1 (2.4)
Normal weight	10 (24.5)
Overweight	21 (51.2)
Obesity grade I	6 (14.6)
Obesity grade II	3 (7.3)
Waist circumference (cm), mean ± SD	93.2 ± 16.5
T2 diabetes, n (%)	
Yes	2 (4.9)
No	39 (95.1)
Systemic hypertension, n (%)	
Yes	4 (9.8)
No	37 (90.2)
Prevalence of liver steatosis by MRI-PDFF[a], n (%)	18 (43.9%)
Liver steatosis grading[b], n (%)	
Grade 1	16 (88.8)
Grade 2	1 (5.6)
Grade 3	1 (5.6)

[a]Steatosis grade of liver fat using automatic MRI-PDFF segmentation. [b]Grade 1: PDFF ≥ 6.4%; Grade 2: PDFF ≥ 17.4%; Grade 3: PDFF ≥ 22.1%[12]. BMI: body mass index; SD: standard deviation; MRI: magnetic resonance imaging; PDFF: proton density fat fraction.

Comparison of the three quantitative MRI-based methods for estimating liver fat

The median liver fat fraction for automatic MRI-PDFF segmentation was 5.0% (IQR 6.4%) (Figure 3B); MRI-PDFF ROI was 2.9% (IQR 6.9%), and MRS-FF, 5.7% (IQR 8.4%). Liver fat quantification by ROI exhibited lower central values compared to automatic segmentation (MRI-PDFF) and spectroscopy (MRS-FF) ($p = 0.006$).

BMI and liver fat correlation estimated by three quantitative MRI-based methods

Liver volume positively correlated with BMI ($r = 0.50$; $p < 0.001$); a higher BMI was associated with greater liver volume (Figure 4). There was a morphometric relationship between BMI and liver size. The correlation between BMI and the liver fat fraction was demonstrated by automatic MRI-PDFF segmentation, MRI-PDFF ROI, and spectroscopy (MRS-FF) (Figure 5). The correlation was positive, with an ascending fat fraction gradient as BMI increased; the magnitude was moderate, uniform, and significant; automatic MRI-PDFF segmentation ($r = 0.42$, $p = 0.006$), MRI-PDFF ROI ($r = 0.39$, $p = 0.011$), and spectroscopy (MRS-FF) ($r = 0.41$, $p = 0.005$).

Correlation between abdominal circumference and liver fat fraction by three quantitative MRI-based methods

Abdominal circumference showed a consistent positive correlation with liver fat fraction across all quantification methods (Figure 6). Significant correlations between abdominal circumference and liver fat fraction were observed with MRI-PDFF automatic segmentation ($r = 0.44$, $p = 0.004$), MRI-PDFF ROI ($r = 0.45$, $p = 0.003$), and MRS-FF ($r = 0.46$, $p = 0.001$). Liver fat fraction increased as abdominal circumference increased.

Comparison by sex of liver fat fraction estimated by three quantitative MRI-based methods

The median liver fat fraction was higher in men than in women for MRI-PDFF, MRI-PDFF ROI, and MRS-FF, with no significant difference (Figure 7). Liver fat values obtained by MRI-PDFF ROI were lower than those from automatic MRI-PDFF segmentation and MRS-FF, with no significant difference between sexes.

DISCUSSION

Our study demonstrated comparable liver fat quantification using automated MRI-PDFF segmentation and MRS-FF. In contrast, MRI-PDFF ROI showed significantly lower liver fat quantification. Liver steatosis was directly correlated with increases in BMI and abdominal circumference. This is the first study in Mexican patients to evaluate liver fat using MRI-based methods and LiverLab software. Based on our results, the specific

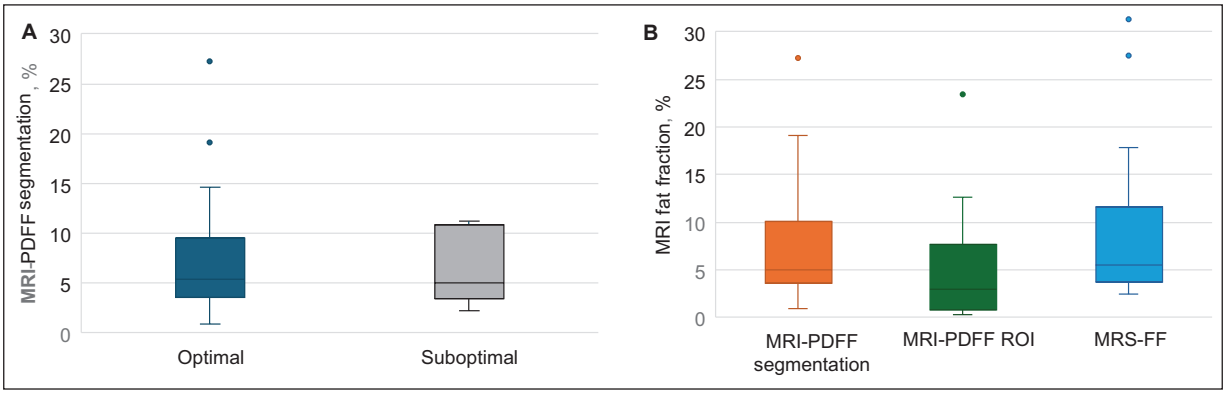

Figure 3. A: box plot comparing the quality of entire liver segmentation by MRI-PDFF, measuring liver fat fraction across optimal (n = 35, 85.4%) and suboptimal (n = 6, 14.6%) evaluations. There was no significant difference between groups. **B:** liver fat fraction, estimated by three noninvasive quantitative MRI methods. The median for automatic MRI-PDFF segmentation was 5.0% (IQR 6.4%), for MRI-PDFF ROI, 2.9% (IQR 6.9%), and for MRS-FF, 5.7% (IQR 8.4%)[a]. MRI-PDFF ROI showed lower values than MRS-FF and automatic MRI-PDFF segmentation in liver fat fraction measurement (p = 0.006).

[a]One outlier with a 31.3% liver fat fraction was not displayed in MRS-FF. MRI: magnetic resonance imaging; IQR: interquartile range; MRI-PDFF: magnetic resonance imaging-proton density fat fraction; ROI: region of interest; MRS-FF: magnetic resonance spectroscopy-fat fraction.

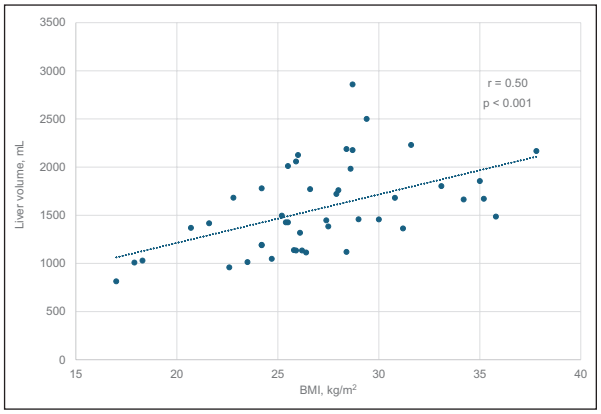

Figure 4. Scatter plot showing the correlation between liver volume and BMI. The dotted line represents the linear regression fit with r = 0.50 and a significant Pearson's test (p < 0.001). A higher BMI was associated with greater liver volume.

BMI: body mass index.

MRI method used should be explicitly stated in the radiology report.

MRI is the best noninvasive tool for diagnosing liver steatosis. Several studies have demonstrated the utility of MRI-PDFF with advanced multi-echo Dixon sequences and LiverLab software[15-18]. These methods quantify total liver fat in a single acquisition and classify steatosis with high precision and reproducibility, while also reducing study time, post-processing time, and intraobserver variability[19]. MRI-PDFF has been proposed as the gold standard for quantifying liver steatosis, comparable to liver biopsy[20] and a correlation between MRI-PDFF and spectroscopy (MRS-FF) has been demonstrated[21,22]. In a meta-analysis by Al-Huneidi et al.[18] MRI-PDFF correlated significantly with liver biopsy as the reference standard for liver fat fraction and steatosis grade. In a study of 120 adult patients aged 18 years or older in Innsbruck, Austria, Henninger et al.[16] evaluated MRI-PDFF and MRS-FF for liver fat quantification using multi-echo Dixon sequences (Avanto scanner, Siemens Healthcare, Erlangen, Germany). Manual ROI showed a strong correlation between the two methods (r = 0.957). Our study evaluated liver fat using LiverLab software and three MRI-based methods for steatosis assessment in patients with no previous history of liver disease. The significant difference between MRI-PDFF ROI and the other two methods is likely due to the user-dependent nature of ROI placement. The literature reports comparisons between MRI-PDFF and MRS-FF using ROI[16,21,23], but a comparison of MRI-PDFF between ROI and automatically segmented volume has not been reported.

Eslam et al.[6] reported that individuals with MASLD have a higher BMI. Furthermore, a high BMI is a diagnostic criterion for MASLD[10]. Liver steatosis is particularly high in obese or overweight individuals[24,25]. In a study by Zou et al.[26] BMI and waist-to-hip ratio were associated with elevated ALT and AST levels in 1,816 adults in Nantong, China. The mean age was 42.8 years, and the mean BMI was 24.48 kg/m^2. Gupta et al.[23] evaluated 55 adult Indians with a mean BMI of 25.33 kg/m^2 and no history of liver disease.

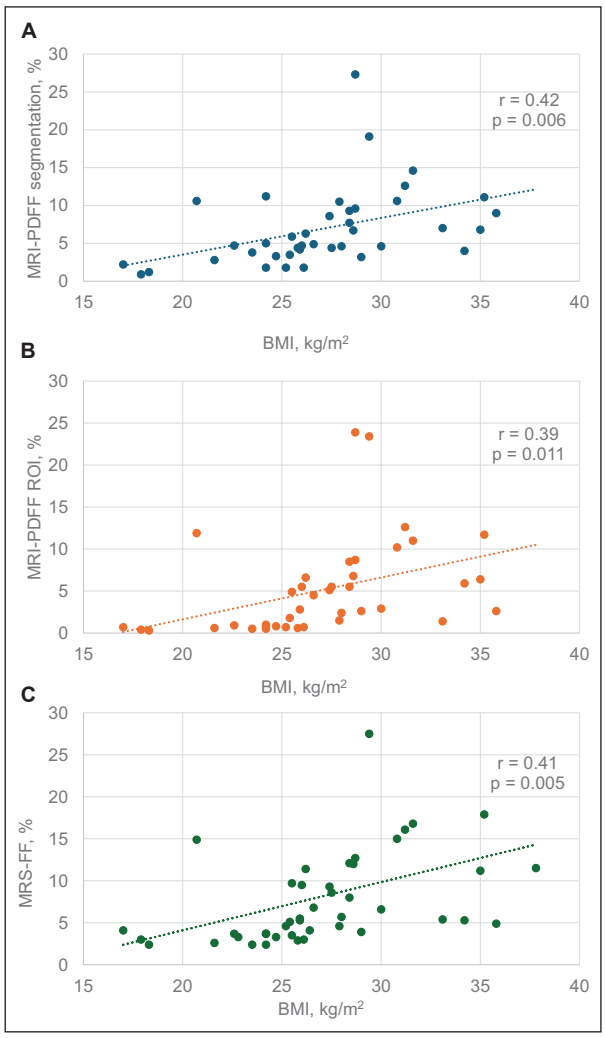

Figure 5. Correlation between BMI and liver fat fraction estimated by three noninvasive quantitative MRI-based methods. The dotted line represents the linear regression fit, with a positive slope indicating a direct association between BMI and liver fat. **A:** blue scatter plot of MRI-PDFF by automatic segmentation of the liver area (r = 0.42, p = 0.006). **B:** orange scatter plot of liver fat fraction estimated in MRI-PDFF ROI (r = 0.39, p = 0.011). **C:** green scatter plot showing the correlation between BMI and liver fat fraction calculated by MRS-FF[a] (r = 0.41, p = 0.005). All three methods showed a positive trend: as BMI increases, liver fat increases. In the Pearson correlation test, all three methods were significantly correlated ($p < 0.05$). The MRI-PDFF ROI liver fat values were lower than those obtained by automatic MRI-PDFF segmentation and MRS-FF. However, all three methods showed a similar significant association with BMI.

[a]One outlier with a liver fat fraction of 31.3% was not displayed in MRS-FF. BMI: body mass index; MRI-PDFF: magnetic resonance imaging-proton density fat fraction; ROI: region of interest; MRS-FF: magnetic resonance spectroscopy-fat fraction.

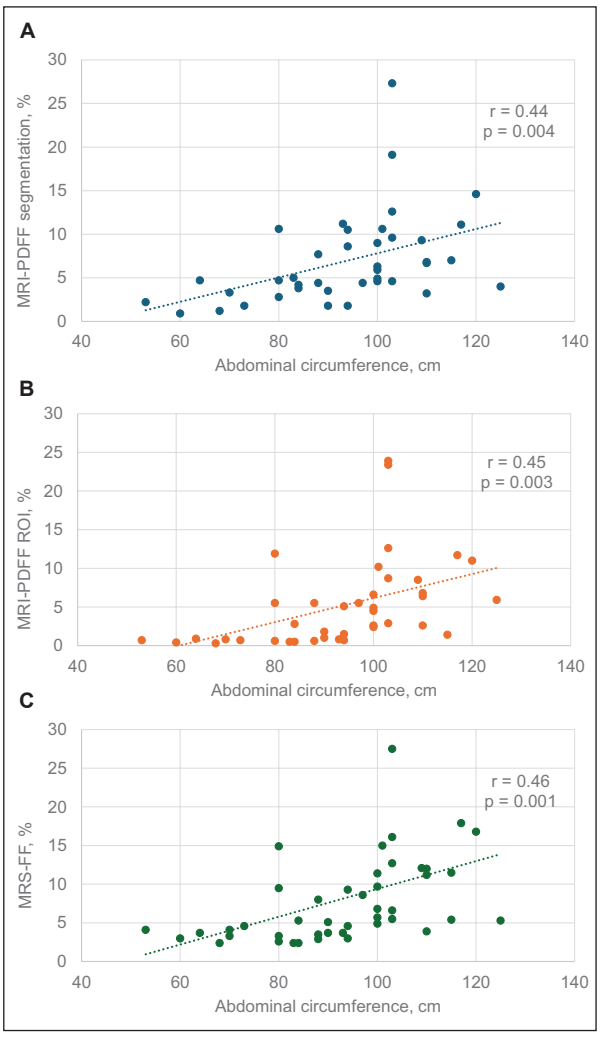

Figure 6. Correlation between abdominal circumference and liver fat fraction by three noninvasive quantitative MRI-based methods for estimating liver fat. **A:** blue scatter plot showing the correlation between abdominal circumference and liver fat fraction quantified by MRI-PDFF in the automatic segmentation area (r = 0.44, p = 0.004). **B:** orange scatter plot showing the correlation between abdominal circumference and the selected MRI-PDFF ROI (r = 0.45, p = 0.003). **C:** green scatter plot showing the correlation between abdominal circumference and liver fat fraction by MRS-FF[a] (r = 0.46, p = 0.001). All three methods show a positive trend: as abdominal circumference increases, liver fat increases. In the Pearson correlation test, all three methods significantly correlated ($p < 0.005$). The MRI-PDFF ROI liver fat values were lower than those from the automatic MRI-PDFF segmentation and MRS-FF.

[a]One outlier with a liver fat fraction of 31.3% was not displayed in MRS-FF. MRI-PDFF: magnetic resonance imaging-proton density fat fraction; ROI: region of interest; MRS-FF: magnetic resonance spectroscopy-fat fraction.

Liver fat fraction was quantified using a 3.0T MRI scanner and LiverLab software with whole-liver and MRI-PDFF ROI (q-Dixon) and MRS-FF. They found a positive correlation between BMI and liver fat fraction with both methods. In Mexico, de Celis Alonso et al.[27] conducted a study of 81 children aged 7 to 9, who were asymptomatic for liver disease. The relationships between obesity, metabolic factors, and liver fat were evaluated using MRI-PDFF and iron-corrected T1 time. They found that children with a higher BMI

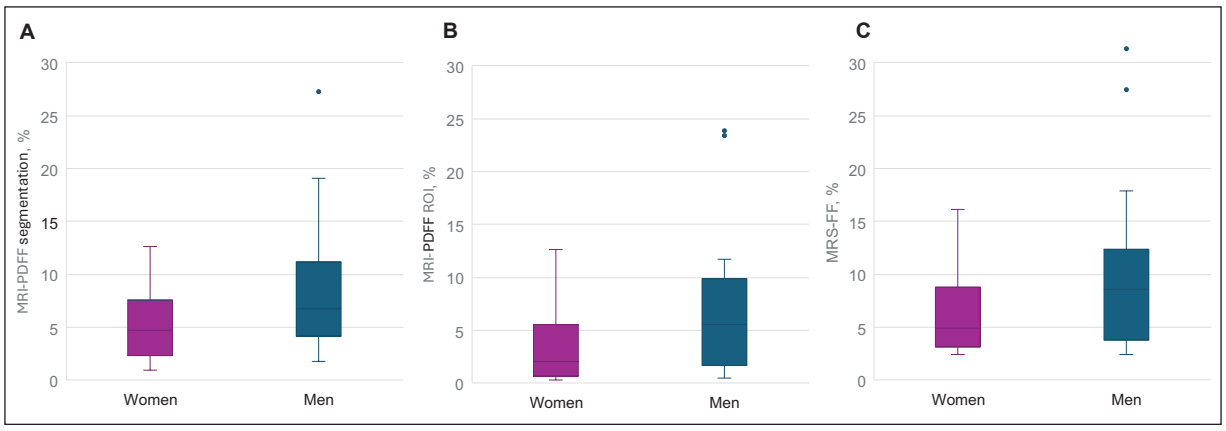

Figure 7. Comparison of liver fat fraction by sex calculated using three noninvasive quantitative MRI-based methods. **A:** box plot for liver fat obtained by automatic MRI-PDFF segmentation. **B:** box plot for liver fat obtained by MRI-PDFF ROI selection. **C:** box plot for liver fat obtained by the MRS-FF[a]. The liver fat values obtained by MRI-PDFF ROI are lower than those from automatic MRI-PDFF segmentation and MRS-FF, with no significant differences between the sexes.

[a]One outlier with a liver fat fraction of 31.3% was not displayed in MRS-FF. MRI-PDFF: magnetic resonance imaging–proton density fat fraction; ROI: region of interest; MRS-FF: magnetic resonance spectroscopy-fat fraction.

had higher liver fat levels. We found a significant correlation between BMI, abdominal circumference, and liver fat percentage in Mexican patients with no history of liver disease. Increases in liver volume and liver fat are directly associated with increases in BMI and abdominal circumference and may serve as MASLD biomarkers.

The global prevalence of MASLD is about 32%, with regional variations. This prevalence is reaching 42.5% in Mexico[4]. Liver steatosis in the Mexican population has been evaluated with grayscale US[28]. A Turkish study[29] of 178 patients evaluated routine MRI sequences on a 1.5T Philips scanner with MRI-PDFF ROI and Dixon sequence. They reported a prevalence of 42.9% for liver steatosis in this population. In the study by Gupta et al.[23], the prevalence of liver steatosis was 30.9% (n = 17) with MRI-PDFF and 32.7% (n = 18) with MRS-FF. The prevalence of liver steatosis in our study was 43.9% among patients with a mean age of 40.6 ± 13.7 without a history of liver disease. The majority (n = 16, 88.8%) had grade I liver steatosis. This prevalence is comparable to that reported in the literature.

The strengths of the study include the use of LiverLab software with a standardized protocol and MR-PDFF for automatic segmentation, which are independent of observer experience and reduce intraobserver error. Study limitations include a small sample size, the lack of biochemical liver function parameters, and the use of liver biopsy as the reference standard.

CONCLUSION

In our study, automated MRI-PDFF segmentation and MRS-FF showed comparable liver fat quantification, while MRI-PDFF ROI yielded significantly lower liver fat values. Liver fat fraction measured by all three MRI-based methods correlated significantly with BMI and abdominal circumference. These exploratory findings should be validated in larger, more diverse cohorts using different MRI scanners and acquisition protocols.

Acknowledgments

The authors thank Professor Ana M. Contreras-Navarro for her guidance in preparing and writing this scientific paper. This original research in the Radiology Specialty field was an awarded thesis at the Tercera Convocatoria Nacional 2024-2025 “Las Mejores Tesis para Publicar en el JMeXFRI”.

Funding

The authors declare that they have not received funding.

Conflicts of interest

The authors declare that they have no conflicts of interest.

Ethical considerations

Protection of humans and animals. The authors declare that this study complied with the Declaration of Helsinki (1964) and subsequent amendments.

Confidentiality, informed consent, and ethical approval. The authors declare they followed their center's protocol for sharing patient data. All participants provided written informed consent. The study was approved by the Institutional Research Ethics Committee and the Research Committee.

Declaration on the use of artificial intelligence. The authors declare that no generative artificial intelligence was used to prepare this manuscript and/or create tables, figures, or figure legends.

REFERENCES

1. Le MH, Yeo YH, Li X, Li J, Zou B, Wu Y, et al. 2019 Global NAFLD prevalence: a systematic review and meta-analysis. Clin Gastroenterol Hepatol. 2022;20(12):2809-2817.e28. doi: 10.1016/j.cgh.2021.12.002.
2. Chan WK, Chuah KH, Rajaram RB, Lim LL, Ratnasingam J, Vethakkan SR. Metabolic Dysfunction-Associated Steatotic Liver Disease (MASLD): a state-of-the-art review. J Obes Metab Syndr. 2023;32(3):197-213. doi: 10.7570/jomes23052.
3. Bernal-Reyes RR, Icaza-Chávez ME, Chi-Cervera LA, Remes-Troche JM, Amieva-Balmori M, Priego-Parra BA, et al. Prevalence and clinical-epidemiological characteristics of a Mexican population with metabolic (dysfunction) associated fatty liver disease: An open population study. Rev Gastroenterol Mex (Engl Ed). 2023;88(3):199-207. doi: 10.1016/j.rgmxen.2022.04.001.
4. Bernal-Reyes RR , Priego-Parra BA, Icaza-Chávez ME, Remes-Troche JM. Adjusted prevalence of metabolic-associated steatotic liver disease (MASLD) in a Mexican. Rev Gastroenterol Mex (Engl Ed). 2025:90(4); 637-638. doi: 10.1016/j.rgmxen.2025.10.027.
5. Lindenmeyer CC, McCullough AJ. The natural history of nonalcoholic fatty liver disease-an evolving view. Clin Liver Dis. 2018;22(1):11-21. doi: 10.1016/j.cld.2017.08.003.
6. Eslam M, Newsome PN, Sarin SK, Anstee QM, Targher G, Romero-Gomez M, et al. A new definition for metabolic dysfunction-associated fatty liver disease: an international expert consensus statement. J Hepatol. 2020;73(1):202-209. doi: 10.1016/j.jhep.2020.03.039.
7. Lee H, Jun DW, Kang BK, Nam E, Chang M, Kim M, et al. Estimating of hepatic fat amount using MRI proton density fat fraction in a real practice setting. Medicine (Baltimore). 2017;96(33):e7778. doi: 10.1097/MD.0000000000007778.
8. Ringe KI, Yoon JH. Strategies and techniques for liver magnetic resonance imaging: new and pending applications for routine clinical practice. Korean J Radiol. 2023;24(3):180-189. doi: 10.3348/kjr.2022.0838.
9. Zhang QH, Zhao Y, Tian SF, Xie LH, Chen LH, Chen AL, et al. Hepatic fat quantification of magnetic resonance imaging whole-liver segmentation for assessing the severity of nonalcoholic fatty liver disease: comparison with a region of interest sampling method. Quant Imaging Med Surg. 2021;11(7):2933-2942. doi: 10.21037/qims-20-989.
10. Rinella ME, Lazarus JV, Ratziu V, Francque SM, Sanyal AJ, Kanwal F, et al. NAFLD Nomenclature consensus group. A multisociety Delphi consensus statement on new fatty liver disease nomenclature. Hepatology. 2023;78(6):1966-1986. doi: 10.1097/HEP.0000000000000520.
11. Basil B, Myke-Mbata BK, Eze OE, Akubue AU. From adiposity to steatosis: metabolic dysfunction-associated steatotic liver disease, a hepatic expression of metabolic syndrome - current insights and future directions. Clin Diabetes Endocrinol. 2024;10(1):39. doi: 10.1186/s40842-024-00187-4.
12. Tang A, Tan J, Sun M, Hamilton G, Bydder M, Wolfson T, et al. Nonalcoholic fatty liver disease: MR imaging of liver proton density fat fraction to assess hepatic steatosis. Radiology. 2013;267(2):422-431. doi: 10.1148/radiol.12120896.
13. Juluri R, Vuppalanchi R, Olson J, Unalp A, Van Natta ML, Cummings OW, et al. Generalizability of the nonalcoholic steatohepatitis Clinical Research Network histologic scoring system for nonalcoholic fatty liver disease. J Clin Gastroenterol. 2011;45(1):55-58. doi: 10.1097/MCG.0b013e3181dd1348.
14. Friedrichsmeier T, The RKWard Team. RKWard: graphical interface to the statistical language R. Version 0.8.0. 2024. Available from: https://rkward.kde.org.
15. Bannas P, Kramer H, Hernando D, Agni R, Cunningham AM, Mandal R, et al. Quantitative magnetic resonance imaging of hepatic steatosis: Validation in ex vivo human livers. Hepatology. 2015;62(5):1444-1455. doi: 10.1002/hep.28012.
16. Henninger B, Zoller H, Kannengiesser S, Zhong X, Jaschke W, Kremser C. 3D Multiecho Dixon for the evaluation of hepatic iron and fat in a clinical setting. J Magn Reson Imaging. 2017;46(3):793-800. doi: 10.1002/jmri.25630.
17. Starekova J, Hernando D, Pickhardt PJ, Reeder SB. Quantification of liver fat content with CT and MRI: state of the art. Radiology. 2021;301(2):250-262. doi: 10.1148/radiol.2021204288.
18. Al-Huneidi LI, Zhao F, Maas R, Ermans SJE, Runge J, Chen X, et al. Liver fat quantification and steatosis grading in fatty liver disease by magnetic resonance imaging: systematic review and meta-analysis. J Gastroenterol Hepatol. 2025. doi: 10.1111/jgh.70086. Epub ahead of print.
19. Frittoli B, Bertuletti M, Angelini V, Grazioli L. Case series: clinical application in liver fat and iron quantification using LiverLab. MAGNETOM Flash. 2020;76(1):63-72.
20. Sterling RK, Duarte-Rojo A, Patel K, Asrani SK, Alsawas M, Dranoff JA, et al. AASLD Practice Guideline on imaging-based noninvasive liver disease assessment of hepatic fibrosis and steatosis. Hepatology. 2025;81(2):672-724. doi: 10.1097/HEP.0000000000000843.
21. Di Martino M, Pacifico L, Bezzi M, Di Miscio R, Sacconi B, Chiesa C, et al. Comparison of magnetic resonance spectroscopy, proton density fat fraction and histological analysis in the quantification of liver steatosis in children and adolescents. World J Gastroenterol. 2016;22(39):8812-8819. doi: 10.3748/wjg.v22.i39.8812.
22. Idilman IS, Keskin O, Celik A, Savas B, Elhan AH, Idilman R, et al. A comparison of liver fat content as determined by magnetic resonance imaging-proton density fat fraction and MRS versus liver histology in non-alcoholic fatty liver disease. Radiol Act. 2016;57(3):271-278. doi: 10.1177/0284185115580488.
23. Gupta A, Dixit R, Prakash A. Non-invasive hepatic fat quantification: can multi-echo Dixon help? Radiol Bras. 2024;57:e20230125. doi: 10.1590/0100-3984.2023.0125.
24. Teng ML, Ng CH, Huang DQ, Chan KE, Tan DJ, Lim WH, et al. Global incidence and prevalence of nonalcoholic fatty liver disease. Clin Mol Hepatol. 2023;29(Suppl):S32-S42. doi: 10.3350/cmh.2022.0365.
25. Li J, Zhou J, Li P, Wang Y, Ridderhof N, Al-Tawfiq JA, et al. The global prevalence and impact of steatotic liver disease and viral infections: a systematic review and meta-analysis. Hepatol Commun. 2025;9(5):e0689. doi: 10.1097/HC9.0000000000000689.
26. Zou C, Duan Z, Chen X. Mediation of blood lipid levels on the relationship between BMI/WHR and liver function in normal, overweight, and obese individuals. Sci Rep. 2025;15:38417. doi: 10.1038/s41598-025-22211-y.
27. de Celis Alonso B, Shumbayawonda E, Beyer C, Hidalgo -Tobon S, López-Martínez B, Dies-Suarez P, et al. Liver magnetic resonance imaging, non-alcoholic fatty liver disease and metabolic syndrome risk in prepubertal Mexican boys. Sci Rep. 2024;14(1):26104. doi: 10.1038/s41598-024-77307-8.
28. Ruiz -Manriquez J, Olivas-Martinez A, Chávez-García LC, Fernández-Ramírez A, Moctezuma-Velazquez C, Kauffman-Ortega E, et al. Prevalence of metabolic-associated fatty liver disease in Mexico and development of a screening tool: the MAFLD-S score. Gastro Hep Adv. 2022;1(3):352-358. doi: 10.1016/j.gastha.2021.12.011.
29. Abbasoğlu A, Karçaaltıncaba M, Karaosmanoğlu AD, Özmen MN, Akata D, İdilman İS. Associations between hepatic and pancreatic steatosis with lumbar spinal bone marrow fat: a single-center magnetic resonance imaging study. Turk J Gastroenterol. 2023;34(6):618-625. doi: 10.5152/tjg.2023.22225.

JMeXFRI

Journal of the Mexican Federation of Radiology and Imaging

Check for updates

FULL RESEARCH ARTICLE

Benign breast diseases in men beyond gynecomastia

Abraham Ortiz-Garcia[1,2], *L. Leticia Rosales-Rosales*[1,2]* *and Javier Hernandez-Hernandez*[3]

[1]*Breast Imaging Department, Instituto de Enfermedades de la Mama FUCAM, A.C.;* [2]*Division of Postgraduate Studies, Faculty of Medicine, Universidad Nacional Autonoma de Mexico;* [3]*Department of Pathology, Instituto de Enfermedades de la Mama FUCAM, A.C. Mexico City, Mexico*

ABSTRACT

Introduction: *Benign breast diseases in men, other than gynecomastia, are poorly understood due to their low prevalence. This study describes the clinical characteristics, mammographic and ultrasound (US) findings, and the histology of benign breast lesions in Mexican men.* **Material and methods:** *Men over 18 years of age with benign breast lesions, with or without gynecomastia, were included. The reason for consultation and associated clinical abnormalities were described. Mammography and/or US were performed and reported according to Breast Imaging Reporting and Data System (BI-RADS) categories. The histopathology diagnosis was reported.* **Results:** *Twenty-eight men with a mean age of 44.6 ± 18.2 years were included. A palpable lump was the main reason for consultation (n = 22, 78.6%). Oval or irregular masses without calcifications predominated on mammography. US findings commonly showed solid, oval, circumscribed, hypoechoic masses with absent or peripheral vascularity. BI-RADS categories 2 (n = 10, 35.7%) and 4A (n = 9, 32.1%) were the most common, followed by 4B (n = 3, 10.7%), 3 (n = 3, 10.7%), and 1 (n = 2, 7.2%), with only one case (3.6%) in category 5. Predominantly diffuse gynecomastia (71.4%) was found in 20 men. Mastitis was the most common histopathology diagnosis (n = 8, 28.6%), followed by epidermoid cyst, pseudoangiomatous stromal hyperplasia, ductal ectasia, myofibroblast, dermoid cyst, hemangioma and cyst, leiomyoma, inclusion cyst, and pilomatrixoma.* **Conclusion:** *Benign breast diseases in men, other than gynecomastia, showed imaging findings suspicious for malignancy, with more than 50% classified as BI-RADS categories 3, 4, or 5. Histopathology revealed a wide range of benign diagnoses. This case series is the largest report of Mexican men with benign breast lesions beyond gynecomastia.*

Keywords: *Male breast. Benign breast disease. Gynecomastia. Ultrasound. Mammography. Mastitis.*

INTRODUCTION

Male breast abnormalities have attracted interest due to an increase in imaging examinations[1]. The main reasons for breast pathology consultation in men are a palpable lump, a pain or burning sensation, increased volume, and, less frequently, nipple discharge[2]. Gynecomastia is the most common benign diagnosis in men and can present simultaneously with other benign breast lesions such as lipoma, epidermoid cyst, stromal pseudoangiomatosis, or mastitis[3-5].

Mammographic findings with a high negative predictive value for malignancy (99%) include a retroareolar location, non-eccentricity, isodense density, and the absence of calcifications or retraction[6]. Benign breast ultrasound (US) findings include an oval shape, a circumscribed margin, and homogeneous echogenicity[7]. US is very precise because the relatively small size of the male breast allows good penetration with a high-frequency beam. It should be performed if suspicious findings are detected on mammography[4]. Other advanced imaging modalities

***Corresponding author:**
L. Leticia Rosales-Rosales
E-mail: letycyarosales@gmail.com

Received for publication: 13-08-2025
Accepted for publication: 18-09-2025
DOI: 10.24875/JMEXFRI.M25000116

Available online: 15-01-2026
J Mex Fed Radiol Imaging. 2025;4(4):273-283
www.JMeXFRI.com

such as contrast-enhanced mammography, magnetic resonance imaging, computed tomography, and positron emission tomography are reserved for specific conditions or used as complements to mammography and US, although their use is limited by high costs and limited accessibility[5].

Benign breast lesions in men other than gynecomastia can present findings suspicious for malignancy, classified as BI-RADS categories 3, 4, or 5 with an indication for biopsy[8,9]. This study describes the clinical characteristics, mammographic and US findings, and histology of benign breast lesions, other than gynecomastia, in Mexican men.

MATERIAL AND METHODS

This retrospective case series was conducted from January 2014 to July 2025 in the Department of Breast Imaging of the Instituto de Enfermedades de la Mama FUCAM, A.C. in Mexico City, Mexico. Men with breast abnormalities, with or without gynecomastia, aged over 18 years and diagnosed with benign breast lesions by imaging and/or histopathology were included. Patients with only gynecomastia, pseudogynecomastia, incomplete medical records, or a malignant breast diagnosis were excluded. Data were collected as part of routine medical care; therefore, informed consent was not required. The institutional research and research ethics committees approved the study.

Study development and variables

Electronic and physical medical records of men with benign breast lesions were analyzed. Mammography and/or US were performed according to the clinical indication of the referring clinician in patients with a palpable mass, nipple discharge, nipple retraction, or breast skin thickening. The variables included age, reason for consultation, associated clinical breast manifestations, simultaneous presence of gynecomastia, and mammographic and/or US findings described according to BI-RADS categories[10].

Image acquisition and analysis

Mammography

Mammography was performed with a Hologic system (Hologic, Inc., Bedford, MA, USA) or a digital IMS Giotto Tomo system (Sasso Marconi, BO, Italy). Conventional projections included two craniocaudal (CC) and two mediolateral oblique (MLO) images of both breasts.

Table 1. Clinical characteristics of 28 men with benign breast lesions other than gynecomastia

Description	Parameter
Age, years ± SD	44.6 ±18.2
Reasons for consultation, n (%)	
Palpable lump	22 (78.6)
Mastalgia	2 (7.1)
Nipple discharge	1 (3.6)
Nipple mass	2 (7.1)
Pruritus	1 (3.6)
Associated clinical manifestations, n (%)	
Mastalgia	7 (24.1)
Pruritus	1 (3.6)
Desquamation	1 (3.6)
Nipple retraction with pain	1 (3.6)
Foreign body sensation	1 (3.6)

SD: standard deviation.

Table 2. Mammography findings[a] in 24 men with benign breast lesions other than gynecomastia

Description[b]	n (%)
Mass, n (%)	23 (96.0)
Shape, n (%)	
Oval	12 (52.2)
Round	1 (4.3)
Irregular	10 (43.5)
Margin, n (%)	23
Circumscribed	10 (43.5)
Obscured	10 (43.5)
Microlobulated	1 (4.3)
Indistinct	2 (8.7)
Spiculated	0
Density, n (%)	23
High	5 (21.7)
Equal	12 (52.2)
Fat containing	6 (26.1)
Asymmetry, n (%)	1 (4.0)
Associated features, n (%)	
No	18 (62.1)
Yes	11 (37.9)
Skin thickening	8 (72.7)
Nipple retraction	3 (27.3)

[a]BI-RADS: Breast Imaging Reporting and Data System.
[b]No evidence of calcifications or architectural distortion.

Breast US

Examination was performed with a LOGIQ E9 system (GE Healthcare, Wauwatosa, WI, USA) using a 10-MHz linear multifrequency transducer in radial and antiradial orientations in all patients as a first-line examination or as a complementary tool to mammography when suspicious features were detected. All studies were independently reviewed by a breast radiologist (LRR) with 10 years of experience, according to the fifth edition of the ACR BI-RADS categories[10].

Gynecomastia was characterized according to the imaging criteria proposed by Mannix et al.[4] who classified the condition into three morphological patterns: nodular, dendritic, and diffuse, based on mammography or US features.

Breast biopsy

Core biopsies were performed with 14 G × 10 cm Tru-cut™ needles (BARD, Tempe, AZ, USA) under US guidance. Breast biopsies were assessed by oncology pathologists (JHH) with 10 years of experience. A histopathology evaluation was considered the reference standard for diagnosis. In cases without a biopsy, the diagnosis was determined based on mammography and/or US findings.

Statistical analysis

Quantitative variables are presented as measures of central tendency and dispersion, and categorical variables as absolute and relative frequencies. The statistical analysis was performed using Microsoft Excel 2021 (Microsoft Corp., Seattle, WA, USA).

RESULTS

Twenty-eight men with benign breast lesions, with or without gynecomastia, were included (Table 1). The mean age was 44.6 ± 18.2 years. A palpable mass was the main reason for consultation (n = 22, 78.6%), followed by less common manifestations such as mastalgia, nipple discharge, nipple mass, and pruritus. Associated clinical manifestations were found in 11 cases (39.3%). These included mastalgia, pruritus, desquamation, nipple retraction with pain, and foreign body sensation.

Mammography findings in men with benign breast lesions

Mammography was performed in 24 men (Table 2). Four patients had conclusive US findings for benign breast lesions and therefore did not require mammography. In 23 masses (96.0%) of 24 cases: masses were oval (n = 12, 52.2%) or irregular (n = 10, 43.5%), while round lesions were uncommon (n = 1, 4.3%). Circumscribed (n = 10, 43.5%) and obscured (n = 10, 43.5%) margins were common. No spiculated margin was identified. Most masses were isodense (n = 12, 52.2%), followed

Table 3. US findings[a] in 28 men with benign breast lesions other than gynecomastia

Description[b]	n (%)
Fluid collection, n (%)	5 (17.9)
Mass, n (%)	23 (82.1)
Shape	
Oval	19 (82.6)
Irregular	4 (17.4)
Margin, n (%)	
Circumscribed	16 (69.6)
Obscured	3 (13.0)
Microlobulated	3 (13.0)
Indistinct	1 (4.4)
Echo pattern, n (%)	
Hypoechoic	10 (43.6)
Hyperechoic	2 (8.7)
Isoechoic	6 (26.0)
Anechoic	2 (8.7)
Heterogeneous	2 (8.7)
Complex cystic and solid	1 (4.3)
Posterior features, n (%)	
Enhancement	8 (34.7)
Shadowing	4 (17.5)
Combined pattern	2 (8.7)
No posterior features	9 (39.1)
Vascularity, n (%)	
Internal flow	5 (17.8)
Peripheral	6 (21.5)
Absent	17 (60.7)
Associated features, n (%)	
No	18 (64.3)
Yes	10 (35.7)
Edema	5 (50.0)
Skin thickening	3 (30.0)
Nipple retraction	2 (20.0)

[a]BI-RADS: Breast Imaging Reporting and Data System.
[b]No case showed round shape, spiculated margin, calcifications, or architectural distortion. US: ultrasound.

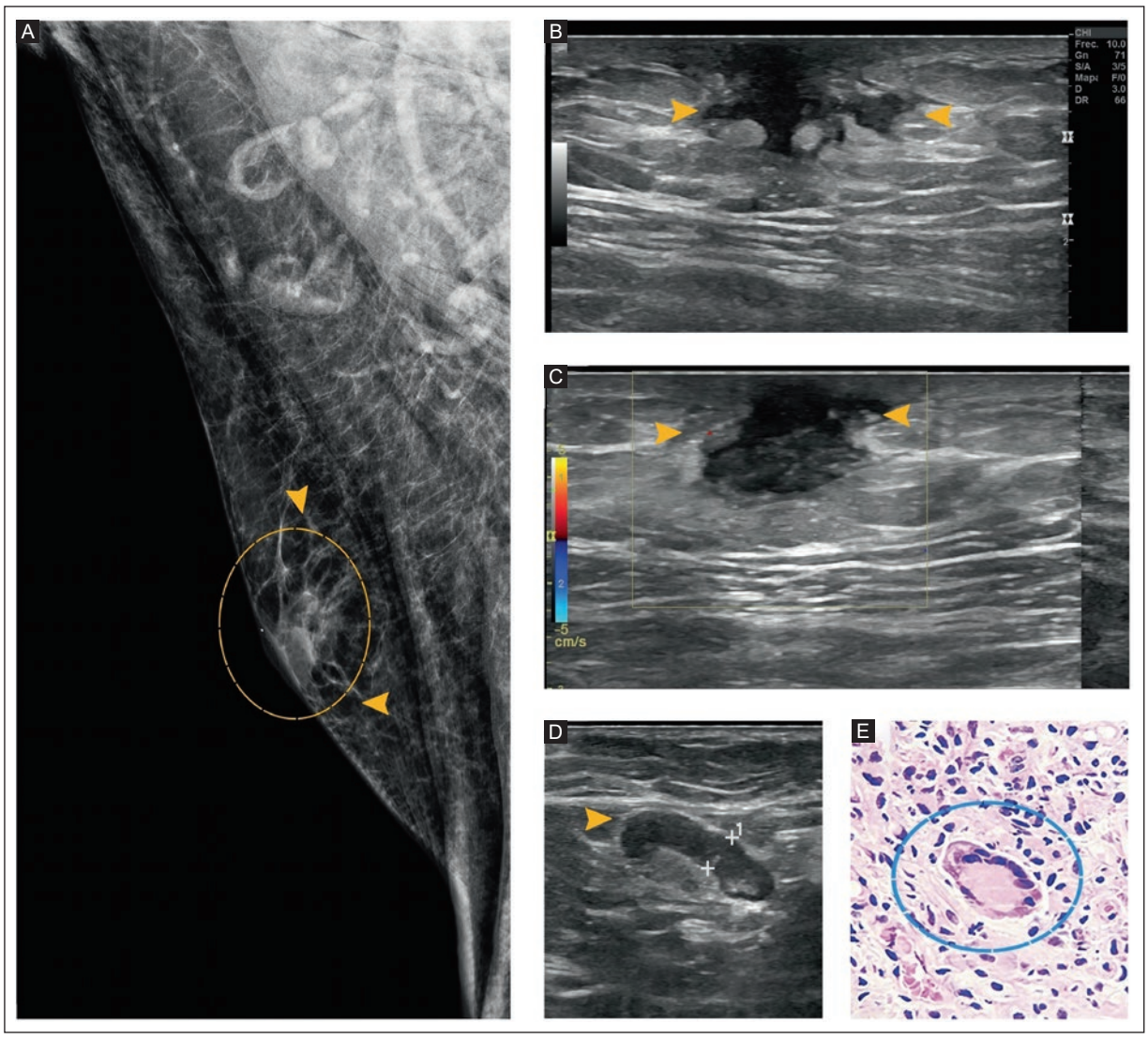

Figure 1. A 44-year-old man with a palpable lump in the right breast. **A:** mammography, MLO projection of the retroareolar region of the right breast, shows an irregular, isodense mass with indistinct margin (arrowheads), associated with skin thickening of the nipple-areolar complex (dashed circle). **B:** grayscale US shows an irregular, heterogeneous, predominantly hypoechoic collection in the right retroareolar region, without acoustic features or a fistulous tract (arrowheads). **C:** color Doppler US shows absence of vascularity (arrowhead). **D:** grayscale US of the right axillary region shows nodes with diffuse cortical thickening and an echogenic hilum (arrowhead). BI-RADS 4A. **E:** histologic section (H&E 40x) shows a stromal inflammatory infiltrate of lymphocytes, plasma cells, macrophages, a few neutrophils, and multinucleated giant cells (dashed circle). The histopathologic diagnosis was mastitis.

US: ultrasound; H&E: hematoxylin and eosin; MLO: mediolateral oblique; BI-RADS: Breast Imaging Reporting and Data System.

by fat-containing (n = 6, 26.1%) and high-density (n = 5, 21.7%) masses. Associated findings were present in 11 men (37.9%), including skin thickening (n = 8, 72.7 %) and nipple retraction (n = 3, 27.3%). No calcifications or architectural distortions were found.

US findings in men with benign breast lesions

Among the 28 patients evaluated by US, the predominant finding was a solid mass (n = 23, 82.1%), most frequently oval (n = 19, 82.6%) with a circumscribed margin (n = 16, 69.6%). No spiculated margin was observed (Table 3). Regarding echogenicity, nearly half of the lesions were hypoechoic (n = 10, 43.6%), followed by isoechoic (n = 6, 26.0%), with less common patterns such as hyperechoic, anechoic, heterogeneous, or complex. Posterior acoustic features were variable, with enhancement in 8 cases (34.7%), shadowing in 4 (17.5%), and absence of posterior features in 9 (39.1%). Vascularity was absent in the majority of cases (n = 17, 60.7%), while peripheral and internal flow were identified

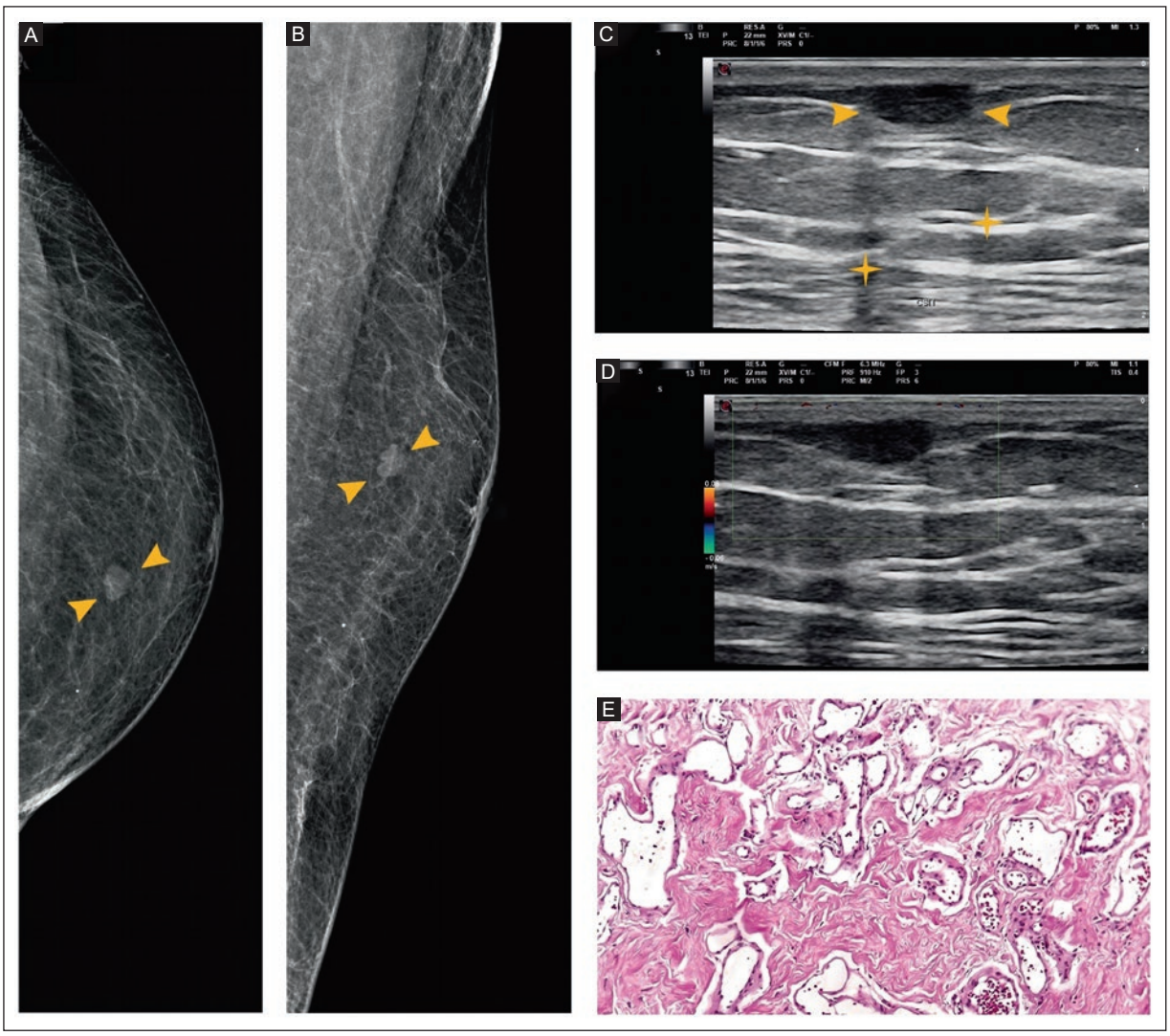

Figure 2. A 79-year-old man with a self-detected palpable lump in the left breast. **A-B:** MLO and CC views of the left upper inner quadrant of the left breast, middle third, show an irregular mass with microlobulated margin, isodense (arrowheads). **C:** grayscale US of the upper inner quadrant of the left breast at the hypodermis shows a circumscribed, oval, hypoechoic mass (arrowheads) with lateral shadows (stars). **D:** Doppler US shows the mass with absence of vascularity. BI-RADS 4A. **E:** histologic section (H&E 20x) shows lobulated proliferation of small-caliber capillaries, densely adherent, lined by endothelium without atypia, with intraluminal erythrocytes and minimal fibrous stroma; no necrosis or significant mitotic activity. The histopathologic diagnosis was hemangioma.

US: ultrasound; H&E: hematoxylin and eosin; MLO: mediolateral oblique; CC: craniocaudal; BI-RADS: Breast Imaging Reporting and Data System.

in 6 (21.5%) and 5 (17.8%) cases, respectively. No calcifications were detected. Associated findings were present in 10 cases (35.7%), including edema, skin thickening, and nipple retraction.

BI-RADS categories of benign breast lesions in men

Benign breast lesions were classified as BI-RADS category 2 (n = 10, 35.7%), category 4A (n = 9, 32.1%), category 4B (n = 3, 10.7%), category 3 (n = 3, 10.7%), and category 1 (n = 2, 7.2%), with only one case (3.6%) in category 5 (Table 4). Benign breast lesions in men spanned a wide range of BI-RADS categories; 57.1% (n = 16) were suspicious for malignancy and classified as BI-RADS categories 3, 4, or 5.

Gynecomastia present simultaneously with benign breast lesions in men

Most men with benign breast lesions also had gynecomastia, which was detected in 20 (71.4%) of 28 cases by mammography and/or US (Table 5). The most common patterns were dendritic (n = 9, 45.0%) and diffuse

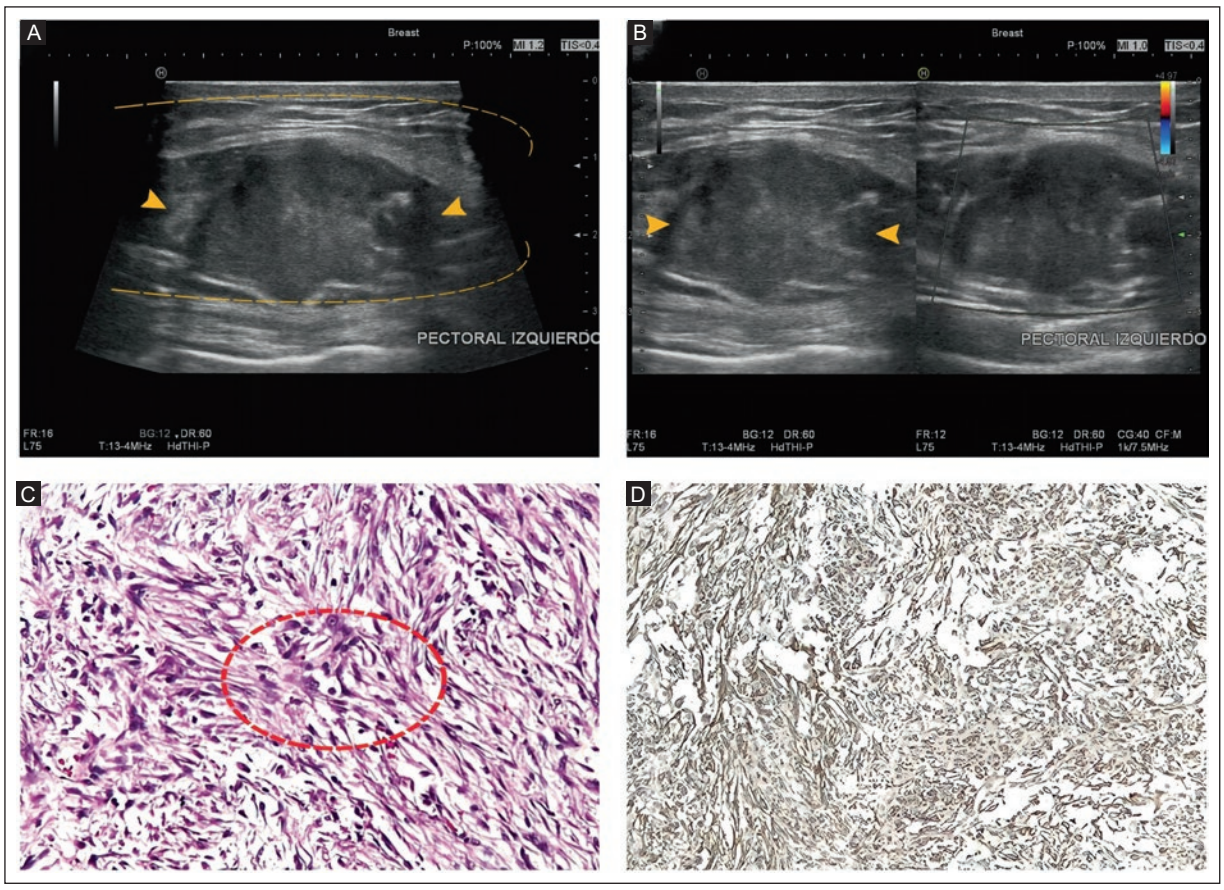

Figure 3. A 30-year-old man with a palpable lump in the left breast. **A:** grayscale US, shows a circumscribed, oval, hypoechoic mass (arrowheads) within the left pectoralis muscle (dashed line). **B:** Doppler US shows the mass without vascularity (arrowheads). BI-RADS category 2. **C:** histologic section (H&E 40x) shows a benign spindle cell lesion, well demarcated, composed of crisscrossed fascicles of smooth muscle cells with eosinophilic cytoplasm and elongated nuclei with blunt ends, displaying a fascicular pattern (dashed circle) without cytologic atypia, necrosis, or mitosis. **D:** immunohistochemistry for actin (40x) shows diffuse positive cytoplasmic staining in of smooth muscle cell fascicles (brown chromogen). The histopathologic diagnosis was leiomyoma.

US: ultrasound; H&E: hematoxylin and eosin; BI-RADS: Breast Imaging Reporting and Data System.

(n = 10, 50.0%), while the nodular type was less common (n = 1, 5.0%). Eight (28.6%) of 28 men with benign lesions did not present simultaneous gynecomastia.

Histopathology and imaging diagnosis in men with benign breast lesions

Twenty cases were confirmed histopathologically (Table 6). Eight were diagnosed based only on imaging findings. Mastitis was confirmed histologically in 8 cases (28.5%). Epidermoid cyst, pseudoangiomatous stromal hyperplasia, and duct ectasia were each diagnosed in 2 cases. There was only one case for each of the following diagnoses: myofibroblastoma, dermoid cyst, hemangioma with cyst, sebaceous cyst, leiomyoma, inclusion cyst, and pilomatrixoma. Lipoma was diagnosed only by US in 6 (21.4%) of the 28 benign breast lesions. The other two diagnoses by imaging were simple and sebaceous cysts. Figure 1 shows a case

Table 4. Benign breast lesions in 28 men according to BI-RADS categories

Description	n (%)
BI-RADS category	
1	2 (7.2)
2	10 (35.7)
3	3 (10.7)
4A	9 (32.1)
4B	3 (10.7)
5	1 (3.6)

BI-RADS: Breast Imaging Reporting and Data System.

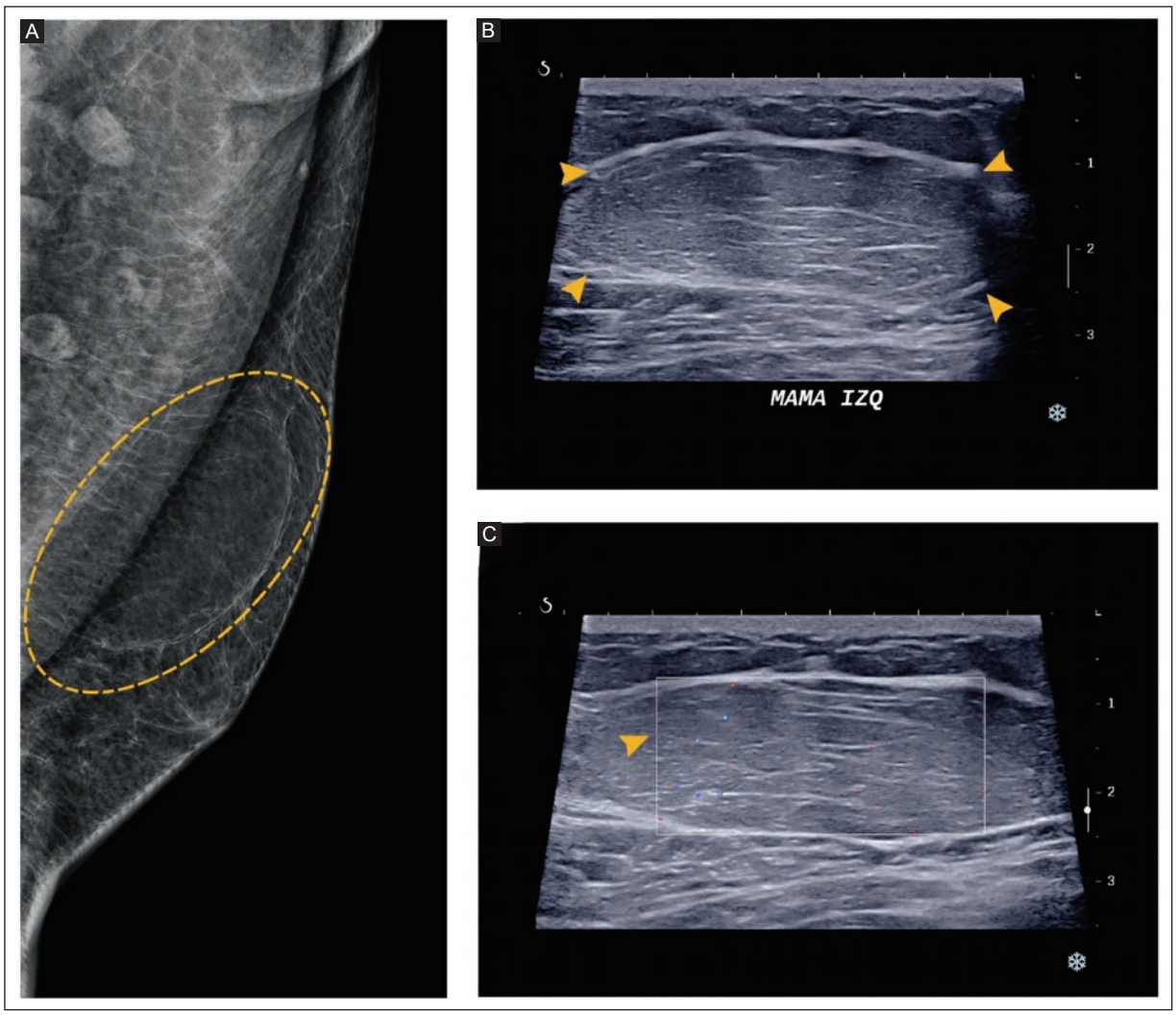

Figure 4. A 34-year-old man with a slow-growing palpable lump in the left breast. **A:** MLO mammography projection of the left breast, upper quadrants, middle to posterior third, shows an oval, circumscribed, fatty mass (dashed circle). **B:** grayscale US shows a circumscribed, oval isoechoic fatty tissue mass (arrowheads) without posterior acoustic findings. **C:** Doppler US shows an avascular mass (arrowhead). BI-RADS 2. The diagnosis was lipoma.

US: ultrasound; H&E: hematoxylin and eosin; MLO: mediolateral oblique; BI-RADS: Breast Imaging Reporting and Data System.

diagnosed as mastitis. Figure 2 shows a case diagnosed as hemangioma. Figure 3 shows a case diagnosed as leiomyoma. Figure 4 shows a case diagnosed as lipoma. Figure 5 shows a case diagnosed as myofibroblastoma. Figure 6 shows a case diagnosed as pilomatrixoma.

DISCUSSION

In our study of benign breast lesions in men, beyond gynecomastia, more than half showed suspicious findings for malignancy on mammography and/or US and were classified as BI-RADS category 3, 4, or 5**.** A palpable mass was the main reason for consultation. Histopathologic examination revealed a wide range of benign breast diagnoses. This case series includes the largest number of Mexican patients with benign breast lesions other than gynecomastia published to date. These findings highlight that, while imaging is an important assessment tool, histopathology is essential for establishing the definitive diagnosis of benign breast lesions in men.

Benign breast lesions in men, other than gynecomastia, can show imaging findings suspicious for malignancy and are classified as BI-RADS 3, 4, or 5. categories[8,9,11,12]. In particular, BI-RADS 3 lesions in men have a higher percentage of malignancy (37.5%) than those reported in women[13]. Yuan et al.[7] in a

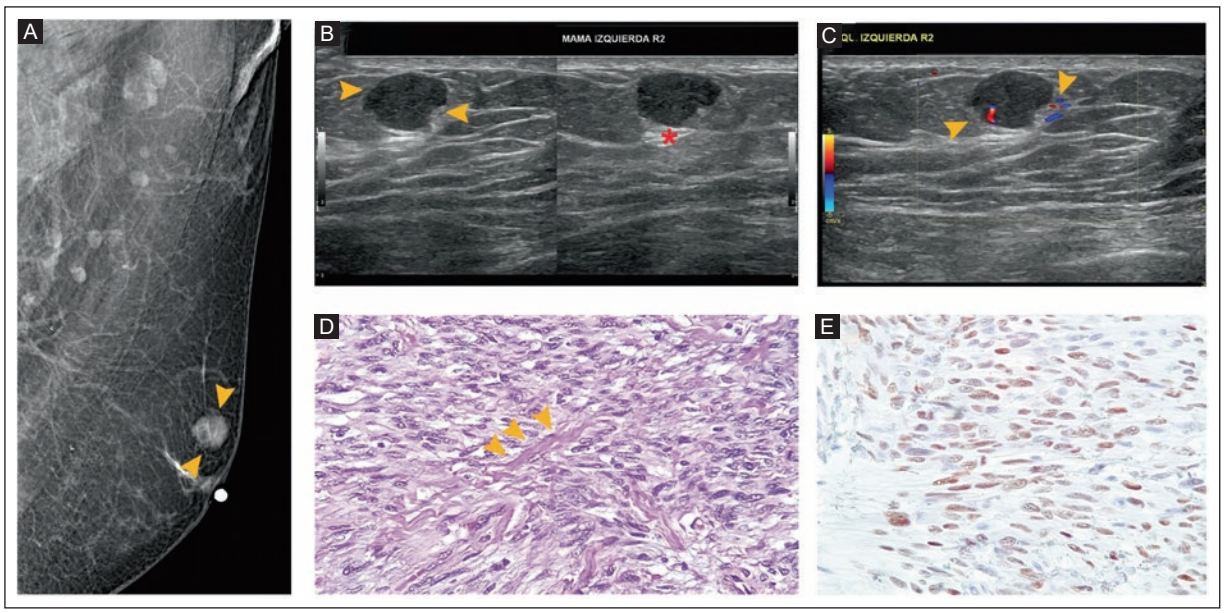

Figure 5. A 62-year-old man with a palpable lump in the left breast. **A:** MLO view of the left breast, upper quadrants, anterior third, shows an oval, circumscribed, isodense mass (arrowheads). **B:** grayscale US shows a circumscribed, oval, hypoechoic mass (arrowheads) with posterior acoustic enhancement (asterisk). **C:** Doppler US shows the mass with central vascularity (arrowheads). BI-RADS 4A. **D:** histologic section (H&E 40x) shows a spindle cell lesion without cell atypia or mitosis, forming a pattern of compact hypercellular areas and thick collagen bands (arrowheads). The cells have a distinct eosinophilic cytoplasm and elongated nuclei with dense chromatin. **E:** estrogen receptor immunohistochemistry (40x) demonstrated nuclear positivity. The histopathologic diagnosis was myofibroblastoma.
US: ultrasound; H&E: hematoxylin and eosin; MLO: mediolateral oblique; BI-RADS: Breast Imaging Reporting and Data System.

Table 5. Gynecomastia[a] present simultaneously with benign breast lesions in men

Description	n (%)
Gynecomastia	
No	8 (28.6)
Yes	20 (71.4)
Nodular	1 (5.0)
Dendritic	9 (45.0)
Diffuse	10 (50.0)

[a]Mammography and/or US.

retrospective analysis conducted in Taiwan with 125 men, showed that US findings such as an echogenic halo, internal vascularity, and irregular shape are also seen in benign processes such as mastitis and fat necrosis without distinguishing benign from malignant masses. On the other hand, findings such as echogenicity, margin, orientation, and acoustic features were not useful for differentiating benign breast lesions. The most common findings on mammography in our study were oval or irregular masses with a circumscribed or obscured margin. Most masses were isodense, and associated findings were present in 11 (37.9%) cases, including skin thickening (n = 8, 72.7 %) and nipple retraction (n = 3, 27.3%). No calcifications or architectural distortions were found. US commonly showed solid, oval, hypoechoic masses with a circumscribed margin and absent vascularity. Associated findings were present in 10 cases (35.7%), including edema, skin thickening, and nipple retraction. Comparable results were reported by Yuan et al.[7] who found hypoechoic and well-defined masses on breast US in 125 men. Breast lesion evaluation with bilateral mammography supplemented by US is recommended for symptomatic men aged 25 and older because breast cancer, though rare, is an important diagnosis that must be ruled out[4]. In our study of benign breast lesions in men, other than gynecomastia, more than half (n = 16, 57.1%) showed suspicious findings for malignancy on mammography and/or US with BI-RADS category 3, 4, or 5. These men required a breast biopsy with histopathologic examination to establish a definitive diagnosis of a benign breast lesion.

Clinical data on benign breast lesions include a painful palpable mass, which may or may not be associated with gynecomastia[7]. Patterson et al.[2] in a retrospective study of 165 American men evaluated by US and mammography, reported that the main clinical

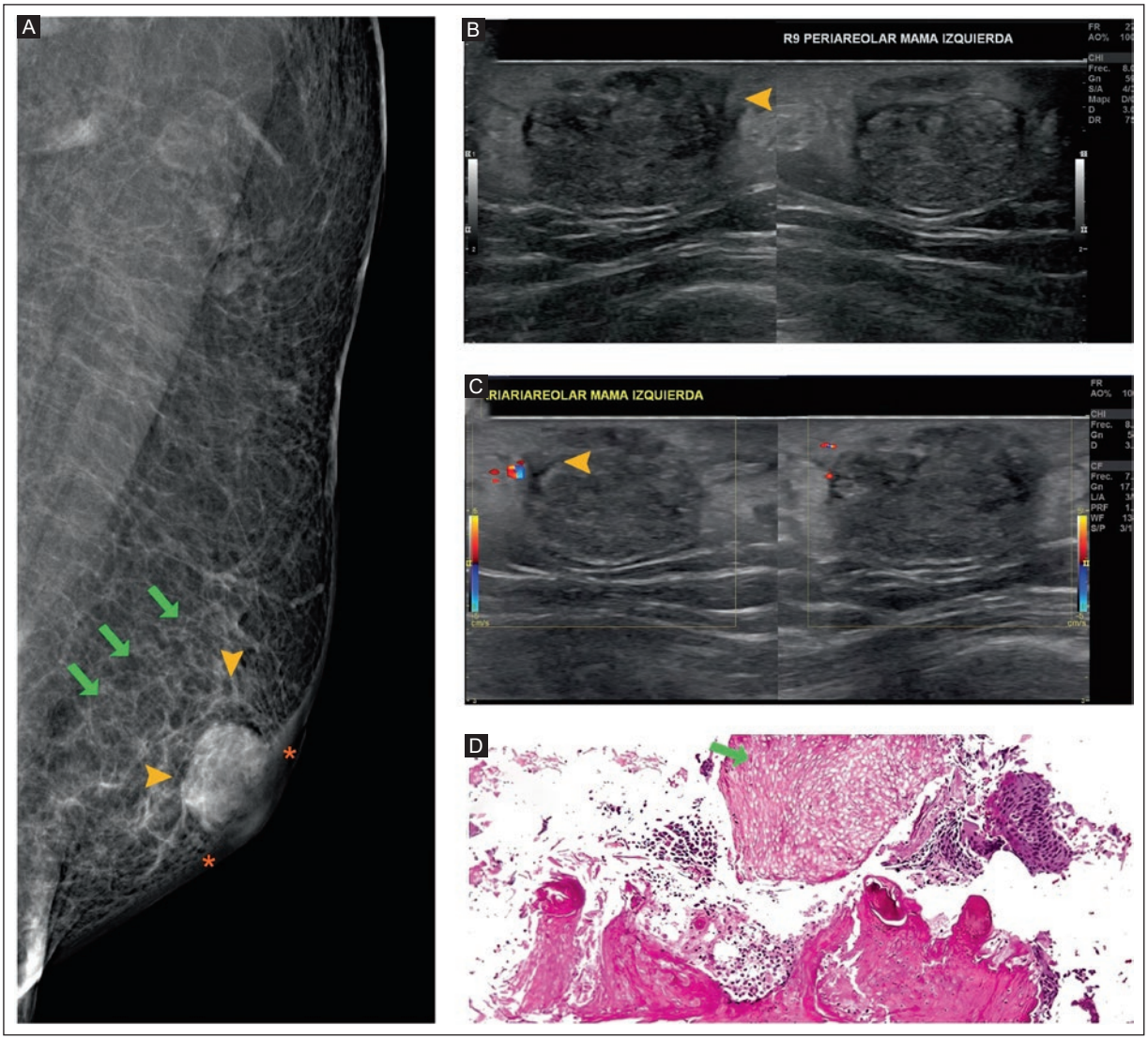

Figure 6. An 80-year-old man with a palpable lump in the left breast, associated with mastalgia. **A:** MLO mammography projection of the retroareolar region of the left breast shows an oval, circumscribed, hyperdense mass (arrowheads) associated with skin (asterisks) and trabecular (arrows) thickening. **B:** grayscale US shows a heterogeneous, predominantly hypoechoic irregular mass with a microlobulated margin and posterior acoustic shadowing (arrowhead). **C:** Doppler US shows a mass with peripheral vascularity (arrowhead). BI-RADS 4A. **D:** histologic section (H&E 40x) shows fragments of a benign adnexal neoplasm with differentiation toward a hairy matrix composed of peripheral basaloid cell lobules that transition to nucleated "ghost" cells with abrupt keratinization (arrow) in fibrous stroma. There is no evidence of cytologic atypia, mitosis, or necrosis. The histopathologic diagnosis was pilomatrixoma.

US: ultrasound; H&E: hematoxylin and eosin; MLO: mediolateral oblique; BI-RADS: Breast Imaging Reporting and Data System.

manifestations were a palpable mass in 92 cases (55.8%) and pain in 50 (30.3%). Muñoz et al.[8] in a retrospective study of 628 Spanish men with 518 mammograms and 454 USs, reported that the most frequent reasons for consultation were a palpable mass (n = 298, 47.5%), followed by increased breast size (n = 251, 39.7%) and pain (n = 232, 36.6%). The main reason for consultation in our study was a palpable mass, followed by mastalgia, nipple discharge, nipple mass, and pruritus. Associated clinical manifestations, mastalgia, pruritus, desquamation, nipple retraction with pain, and foreign body sensation, were found in 11 cases (39.3%). Mastalgia appeared both as a primary complaint and as an associated symptom, making it the most recurrent accompanying clinical feature. Symptomatic men with clinical findings such as a palpable mass, breast pain, or nipple abnormalities require mammography and US evaluation[4].

Most breast lesions in men are benign, and gynecomastia is the most common[4]. It is caused by metabolic,

Table 6. Histopathologic and imaging diagnosis in 28 men with benign breast lesions other than gynecomastia

Description	n (%)
Histopathologic diagnosis	
Mastitis	8 (28.5)
Epidermoid cyst	2 (7.1)
Pseudoangiomatous stromal hyperplasia	2 (7.1)
Duct ectasia	2 (7.1)
Myofibroblastoma	1 (3.6)
Dermoid cyst	1 (3.6)
Hemangioma and cyst	1 (3.6)
Leiomyoma	1 (3.6)
Inclusion cyst	1 (3.6)
Pilomatrixoma	1 (3.6)
Imaging diagnosis[a]	
Lipoma	6 (21.4)
Simple cyst	1 (3.6)
Sebaceous cyst	1 (3.6)

[a]The diagnosis was made by imaging findings on mammography and/or US in 8 men.

endocrinological, neoplastic, or drug-induced diseases[8]. Gynecomastia presents as an enlarged breast or palpable mass, sometimes accompanied by pain or increased local sensitivity[4,11,12,14]. Fibroglandular tissue detected on imaging establishes the diagnosis of gynecomastia[15]. Muñoz et al.[8] in a retrospective study of 628 Spanish men, reported that gynecomastia was the most common diagnosis (n = 502, 80.4%). Gynecomastia can present simultaneously with other benign breast lesions. In our study, gynecomastia was detected in 20 (71.4%) of 28 men with other benign breast lesions. A comparable result was reported by Santana-Vela et al.[16] in Mexican men with gynecomastia present in 60.9% (n = 28). Most cases of gynecomastia can be distinguished from other breast diagnoses by combining clinical and imaging findings.

Benign histopathological breast lesions in men beyond gynecomastia, are diverse and include mastitis, lipoma, and epidermoid cyst, as well as less common entities such as pilomatrixoma and hemangioma[4,17]. AlSharif et al.[18] in a narrative review of unusual breast lesions in men, highlighted uncommon entities such as pilomatrixoma and hemangioma. These breast lesions, detected incidentally or more often as a palpable mass on clinical examination, may have imaging findings that mimic malignancy, such as irregular borders and heterogeneous echogenicity on US. In our study, 20 (71.4%) breast biopsies were performed, while 8 cases were based only on imaging findings. The histopathologic diagnoses of non-gynecomastia benign breast lesions in men were varied. Mastitis was the most common diagnosis (n = 8, 28.5%), followed by epidermoid cyst, pseudoangiomatous stromal hyperplasia, ductal ectasia, myofibroblast, dermoid cyst, hemangioma and cyst, leiomyoma, inclusion cyst, and pilomatrixoma. In contrast, Santiago-Sanabria et al.[9] reported that in Mexican men, myofibroblastoma was the predominant lesion (n = 4, 25.0%). Other diagnoses included fibroadenoma, ductal ectasia, mastitis, and duct hyperplasia. There is great heterogeneity among benign lesions of the male breast. Histopathology examination may be needed to establish a definitive diagnosis.

The strengths of this study of benign breast lesions in men are related to the integration of clinical manifestations, imaging findings, and histopathologic examination. The imaging findings were assessed using the BI-RADS lexicon. The limitations of the study include a small sample size, a single-center, retrospective design, and its conduction at a tertiary care center, which introduces potential selection bias.

CONCLUSION

This study provides clinical, imaging, and histopathological evidence on a scarcely studied population of Mexican men with non-gynecomastia benign breast lesions. Our study demonstrated that other benign breast lesions may occur simultaneously with gynecomastia. More than half of the cases showed suspicious findings for malignancy on mammography and/or US with BI-RADS category 3, 4, or 5, and required breast biopsy for diagnosis. These results highlight the need to integrate clinical and imaging findings with histopathologic examination to achieve a definitive diagnosis of breast lesions in men.

Acknowledgments

The authors thank Professor Ana M. Contreras-Navarro for her guidance in preparing and writing this scientific paper.

Funding

The authors declare that they have not received funding.

Conflicts of interest

The authors declare no conflicts of interest.

Ethical considerations

Protection of humans and animals. This study complied with the Declaration of Helsinki (1964) and subsequent amendments.

Confidentiality, informed consent, and ethical approval. The authors declare they followed their center's protocol for sharing patient data. Informed consent was not required for this observational study of information collected during routine clinical care.

Declaration on the use of artificial intelligence. The authors did not use generative artificial intelligence to prepare this manuscript and/or create tables, figures, or figure legends.

REFERENCES

1. Giordano SH, Cohen DS, Buzdar AU, Perkins G, Hortobagyi GN. Breast carcinoma in men: a population-based study. Cancer. 2004;101(1):51-57. doi: 10.1002/cncr.20312.
2. Patterson SK, Helvie MA, Aziz K, Nees AV. Outcome of men presenting with clinical breast problems: the role of mammography and ultrasound. Breast J. 2006;12(5):418-423. doi: 10.1111/j.1075-122X.2006.00298.x.
3. Chau A, Jafarian N, Rosa M. Male breast: clinical and imaging evaluations of benign and malignant entities with histologic correlation. Am J Med. 2016;129(8):776–791. doi:10.1016/j.amjmed.2016.01.009.
4. Mannix J, Duke H, Almajnooni A, Ongkeko M. Imaging the male breast: gynecomastia, male breast cancer, and beyond. RadioGraphics. 2024; 44(6):e230181. doi:10.1148/rg.230181.
5. Yang S, Leng Y, Chau CM, Ma KFJ, Fung WY, Chan RLS, et al. The ins and outs of male breast and anterior chest wall lesions from childhood to adulthood. Clin Radiol. 2022;77(7):503-513. doi: 10.1016/j.crad.2022.02.020.
6. Huang Y, Xiao Q, Sun Y, Li Q, Wang S, Gu Y. Differential diagnosis of benign and malignant male breast lesions in mammography. Eur J Radiol. 2020;132:109339. doi: 10.1016/j.ejrad.2020.109339.
7. Yuan WH, Li AF, Chou YH, Hsu HC, Chen YY. Clinical and ultrasonographic features of male breast tumors: a retrospective analysis. PLoS One. 2018; 20;13(3):e0194651. doi: 10.1371/journal.pone.0194651.
8. Muñoz-Carrasco R, Alvarez-Benito M, Muñoz-Gomariz E, Raya-Povedano JL, Martínez-Paredes M. Mammography and ultrasound in the evaluation of male breast disease. Eur Radiol. 2010; 20(12):2797-2805. doi:10.1007/s00330-010-1867-7.
9. Santiago-Sanabria L, Sosa-Reyes AA, Ruiz-Antonio RI, Aguilar-Araiza CP, Cisneros-Vieyra SA. Características clínicas, imagenológicas e histopatológicas de desórdenes benignos de mama en hombres. Cir Cir. 2025;93(4):385-394. doi:10.24875/CIRU.24000267.
10. American College of Radiology. ACR BI-RADS® Atlas, Breast Imaging Reporting and Data System. 5th ed. Reston, VA, USA: American College of Radiology; 2013.
11. Nguyen C, Kettler MD, Swirsky ME, Miller VI, Scott C, Krause R, et al. Male breast disease: pictorial review with radiologic-pathologic correlation. Radiographics. 2013;33(3):763-779. doi: 10.1148/rg.333125137.
12. Charlot M, Béatrix O, Chateau F, Dubuisson J, Golfier F, Valette PJ, et al. Pathologies of the male breast. Diagn Interv Imaging. 2013;94(1): 26-37. doi: 10.1016/j.diii.2012.10.011.
13. Kim EK, Ko KH, Oh KK, Kwak JY, You JK, Kim MJ, et al. Clinical application of the BI-RADS final assessment to breast sonography in conjunction with mammography. AJR Am J Roentgenol. 2008;190(5):1209-1215. doi: 10.2214/AJR.07.3259.
14. Shaaban AM. Pathology of the male breast. Diagn Histopathol. 2019;25(4):138-142. doi: 10.1016/j.mpdhp.2019.01.004.
15. Fricke A, Lehner GM, Stark GB, Penna V. Gynecomastia: histological appearance in different age groups. J Plast Surg Hand Surg. 2018;52(3): 166-171. doi: 10.1080/2000656X.2017.1372291.
16. Santana-Vela IA, Córdova-Chávez NA, Putz-Botello MD, Onofre-Castillo J, Cuevas-Betancourt RE, Arreozola-Mayoral MA. Características por imagen de afecciones de la mama masculina. An Radiol Mex. 2016;15(2): 120-130.
17. Önder Ö, Azizova A, Durhan G, Elibol FD, Akpınar MG, Demirkazık F. Imaging findings and classification of the common and uncommon male breast diseases. Insights Imaging. 2020;11(1):27. doi: 10.1186/s13244-019-0834-3.
18. AlSharif S, Alshamrani KM, Scaranelo A, Khoumais N, Subahi A, Mesurolle B. Unusual male breast lesions. J Clin Imaging Sci. 2021;11:21. doi: 10.25259/JCIS_43_2021.

JMeXFRI

Journal of the Mexican Federation of Radiology and Imaging

Check for updates

CASE REPORT

Diagnostic imaging challenge of an extensive anorectal cavernous hemangioma: a case report

I.F. Alejandro Lopez-Beltran[1], *Osiris G. Salazar-Lopez*[1]* and *Jose A. Matute-Briceño*[2]

[1]*Department of Radiology and Imaging, Hospital de Especialidades Num. 2, Unidad Medica de Alta Especialidad, Centro Medico Nacional del Noroeste "Lic. Luis Donaldo Colosio Murrieta", Ciudad Obregon;* [2]*Department of Pathology, Hospital General de Zona Num. 14, Hermosillo. Sonora, Mexico*

ABSTRACT

Anorectal vascular lesions, such as hemangiomas and vascular malformations, are uncommon clinical entities. Cavernous hemangioma is particularly rare, with only a limited number of histopathologically confirmed cases reported in the literature. This case report presents a 20-year-old woman with lifelong hematochezia and transfusion-dependent anemia. She was previously misdiagnosed with grade III hemorrhoidal disease. Non-contrast-enhanced computed tomography (CT) images showed multiple mural phleboliths in the rectal region. Contrast-enhanced CT showed concentric mural thickening of the rectum, multiple perirectal serpentine vascular structures, and phleboliths in the rectal wall. Contrast-enhanced pelvic magnetic resonance imaging (MRI) demonstrated diffuse circumferential rectal wall thickening and numerous perirectal serpiginous vessels. There was marked enhancement of the rectal wall and perirectal vessels after gadolinium administration with signal voids corresponding to phleboliths. The combination of phleboliths and serpentine vessels is a pathognomonic feature that suggests the diagnosis of cavernous hemangioma. Laparoscopic abdominoperineal resection was successful, and the patient was discharged with a functional colostomy. Postoperative imaging confirmed complete lesion resection. Histopathologic examination of the surgical specimen confirmed the diagnosis of cavernous hemangioma. This case report is for educational purposes. It exemplifies the essential imaging-pathologic correlation and highlights the critical role of multimodality imaging.

Keywords: *Cavernous hemangioma. Magnetic resonance imaging. Multidetector computed tomography. Gastrointestinal hemorrhage. Case report.*

INTRODUCTION

Hemangiomas are congenital hamartomatous vascular malformations characterized by excessive proliferation of blood vessels, predominantly veins and capillaries. These rare benign tumors account for approximately 5% of all gastrointestinal neoplasms of this type and typically arise within the submucosal connective tissue, as solitary or multiple lesions[1,2]. The principal pathological variants include cavernous, capillary, and mixed forms[3]. Although hemangiomas usually range from a few millimeters to two centimeters, they can reach considerable size in the rectal region. Clinically, they follow an insidious course, manifesting as recurrent and often occult transrectal hemorrhage that can lead to chronic anemia[2,4].

Computed tomography (CT) and magnetic resonance imaging (MRI) play a pivotal role in distinguishing the characteristic findings of hemangiomas from other pathologies[5,6]. We present the case of a young woman with lifelong hematochezia, initially misdiagnosed as hemorrhoidal disease, in whom contrast-enhanced CT and MRI were instrumental in identifying an anorectal cavernous hemangioma.

***Corresponding author:**
Osiris G. Salazar-Lopez
E-mail: osiris.salazar@gmail.com

Received for publication: 26-01-2025
Accepted for publication: 10-11-2025
DOI: 10.24875/JMEXFRI.25000004

Available online: 15-01-2026
J Mex Fed Radiol Imaging. 2025;4(4):284-289
www.JMeXFRI.com

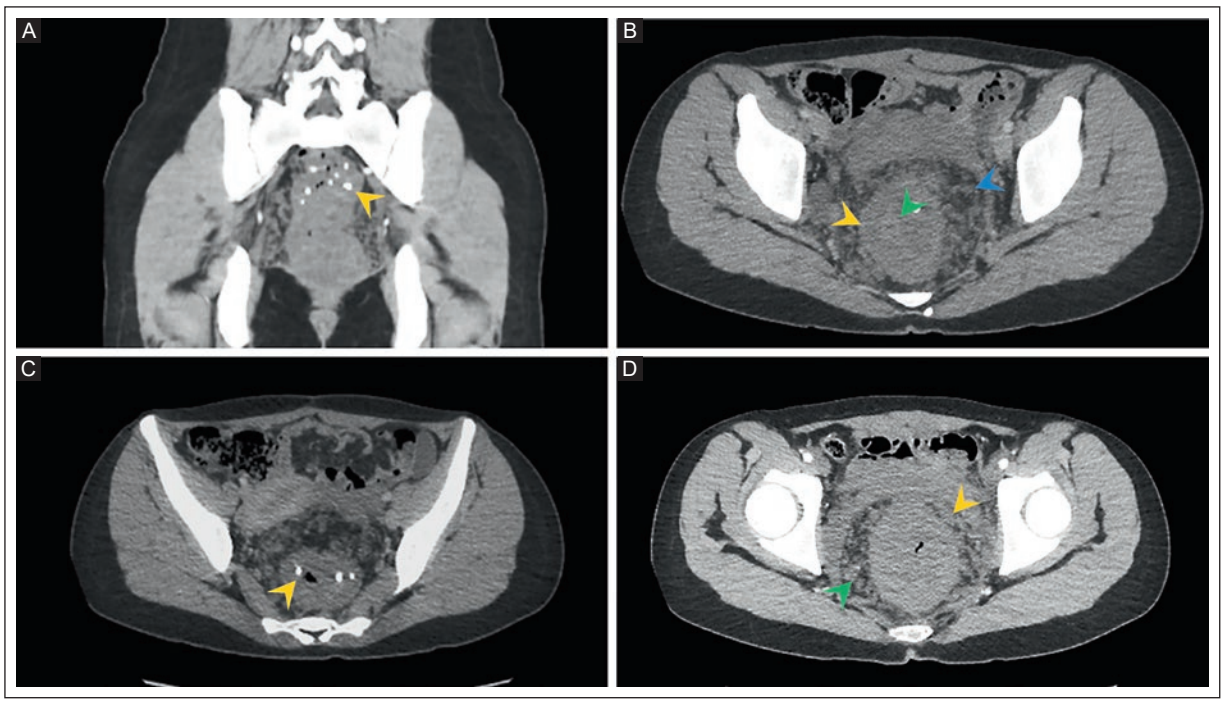

Figure 1. Non-contrast and contrast-enhanced abdominopelvic CT of a 20-year-old woman with intermittent hematochezia and severe anemia. **A:** coronal non-contrast CT image shows multiple mural phleboliths in the rectal region (orange arrowhead). **B:** axial contrast-enhanced venous phase CT image shows concentric rectal thickening (orange arrowhead), mild mucosal enhancement (green arrowhead), and multiple perirectal serpentine vascular structures (blue arrowhead). **C:** axial contrast-enhanced CT image shows phleboliths in the rectal wall (orange arrowhead). **D:** axial contrast-enhanced CT image shows concentric mural thickening of the rectum (orange arrowhead) and multiple perirectal serpentine vascular structures (green arrowhead).

CT: computed tomography.

CASE DESCRIPTION

A 20-year-old woman with a lifelong history of intermittent hematochezia, requiring blood transfusions twice a year, was admitted to the emergency department due to lower gastrointestinal bleeding. Physical examination revealed the patient was pale but hemodynamically stable. Digital rectal examination was deferred.

She had previously been diagnosed with grade III hemorrhoidal disease based on the presence of blood clots in the anal region. Laboratory test showed severe anemia with a hemoglobin level of 4 g/dL. Colonoscopy revealed rectal luminal collapse caused by multiple submucosal nodular lesions with a soft, compressible consistency that collapsed under instrumental compression. The overlying mucosa exhibited diffuse telangiectasias, with preserved mucosa and no evidence of ulceration, active bleeding, or inflammatory changes. These findings were suggestive of an extensive submucosal vascular lesion.

IMAGING FINDINGS

Computed tomography

A non-contrast and contrast-enhanced abdominopelvic CT scan was performed using a GE Revolution EVO/128 (GE Medical Systems, Chicago, IL, USA). The examination revealed diffuse rectal wall thickening measuring 2.5 to 3.5 cm, with a craniocaudal extent of approximately 13.8 cm (Figure 1). Multiple intramural phleboliths and serpiginous perirectal vessels were also observed.

Magnetic resonance imaging

Non-contrast and contrast-enhanced pelvic MRI was performed using a MAGNETOM Skyra 3.0T scanner (Siemens Healthineers, Erlangen, Germany). The imaging examination confirmed diffuse concentric mural thickening of the anorectal region, which measured 13.8 cm in length from the anal verge. Additional findings included small punctate phleboliths of low

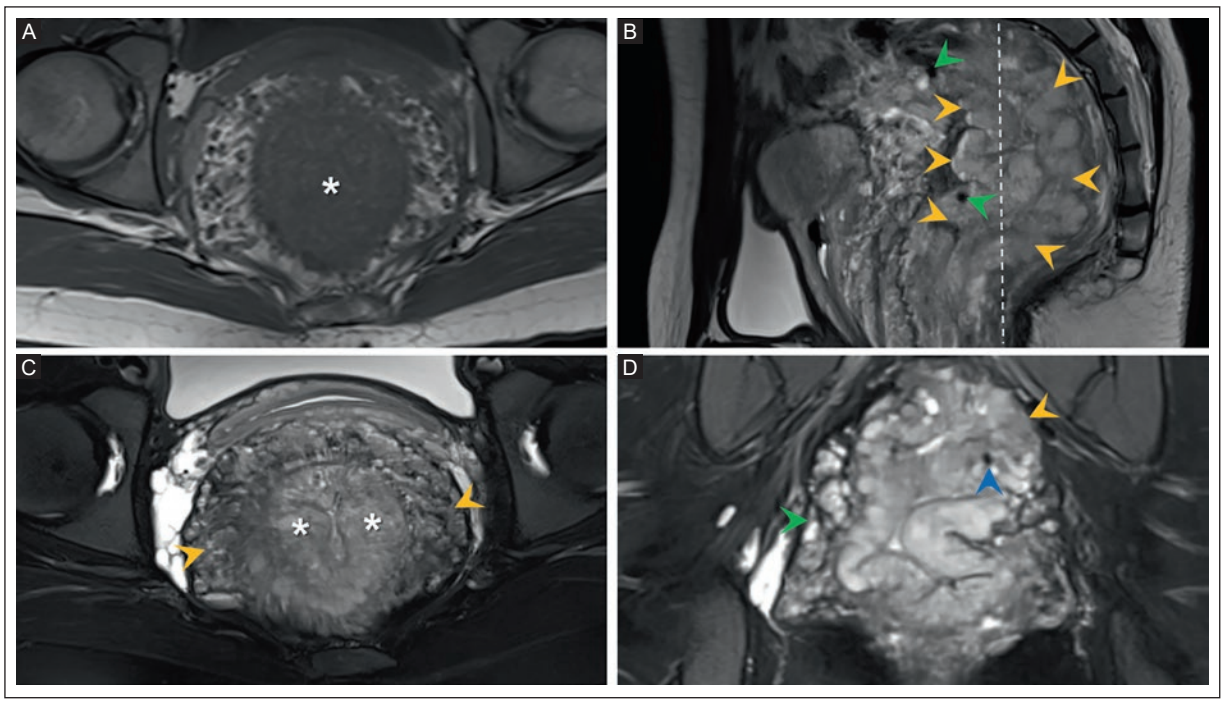

Figure 2. Non-contrast and contrast-enhanced pelvic MRI of a 20-year-old woman with intermittent hematochezia and severe anemia. **A:** axial T1-weighted image reveals concentric anorectal mucosal and submucosal thickening (asterisk). **B:** sagittal T2-weighted image shows diffuse concentric thickening of the anterior and posterior anorectal walls (orange arrowheads). This thickening measures 13.8 cm in craniocaudal length from the anal verge (dotted line), and contains small, punctate, low-signal intensity phleboliths within the anorectal wall (green arrowheads). **C:** axial fat-saturated T2-weighted image shows numerous serpentine vascular structures within the perirectal fat (orange arrowheads) and concentric mucosal and submucosal thickening of the anorectal region (asterisks). **D:** coronal fat-saturated post-contrast T1-weighted image shows intense enhancement of the anorectal wall (orange arrowhead) and multiple enhancing serpentine perirectal vascular structures (green arrowhead), one of which contains a signal void corresponding to a phlebolith (blue arrowhead).

MRI: magnetic resonance imaging.

signal intensity within the anorectal wall (Figure 2). The lesion exerted a mass effect, causing anterior displacement of the uterus and urinary bladder with no evidence of invasion. Numerous enhancing serpiginous vessels within the anorectal wall were well visualized on post-contrast fat-saturated sequences, with increased signal intensity in the perirectal fat. These imaging features were suggestive of an anorectal cavernous hemangioma.

Clinical outcome

The patient underwent laparoscopic abdominoperineal resection with a colostomy. Postoperative imaging confirmed complete resection (Figure 3). Gross examination of the surgical specimen revealed a large intestinal segment with hemorrhagic serosa and congested adipose tissue. The mucosa was hemorrhagic and edematous. Histopathologic analysis confirmed numerous dilated, congested blood vessels with organized thrombi in the submucosa, diagnostic findings of a cavernous hemangioma (Figure 4). The lesion consisted of many large, irregular vascular channels closely apposed in a sinusoidal pattern, lacking cellular atypia. The overlying rectal mucosa showed no atypia but exhibited nodular protrusion due to displacement by the underlying submucosal mass.

DISCUSSION

This case of a 20-year-old woman with intermittent hematochezia and severe anemia highlights the pathognomonic imaging findings of anorectal cavernous hemangioma on contrast-enhanced CT and pelvic MRI, such as circumferential anorectal wall thickening, multiple intramural vessels, and intramural phleboliths, with the latter being the most specific sign. Contrast-enhanced CT and pelvic MRI are also useful for preoperative planning, providing critical information about lesion extent and involvement of adjacent structures.

Anorectal cavernous hemangioma can be easily overlooked when appropriate imaging modalities are

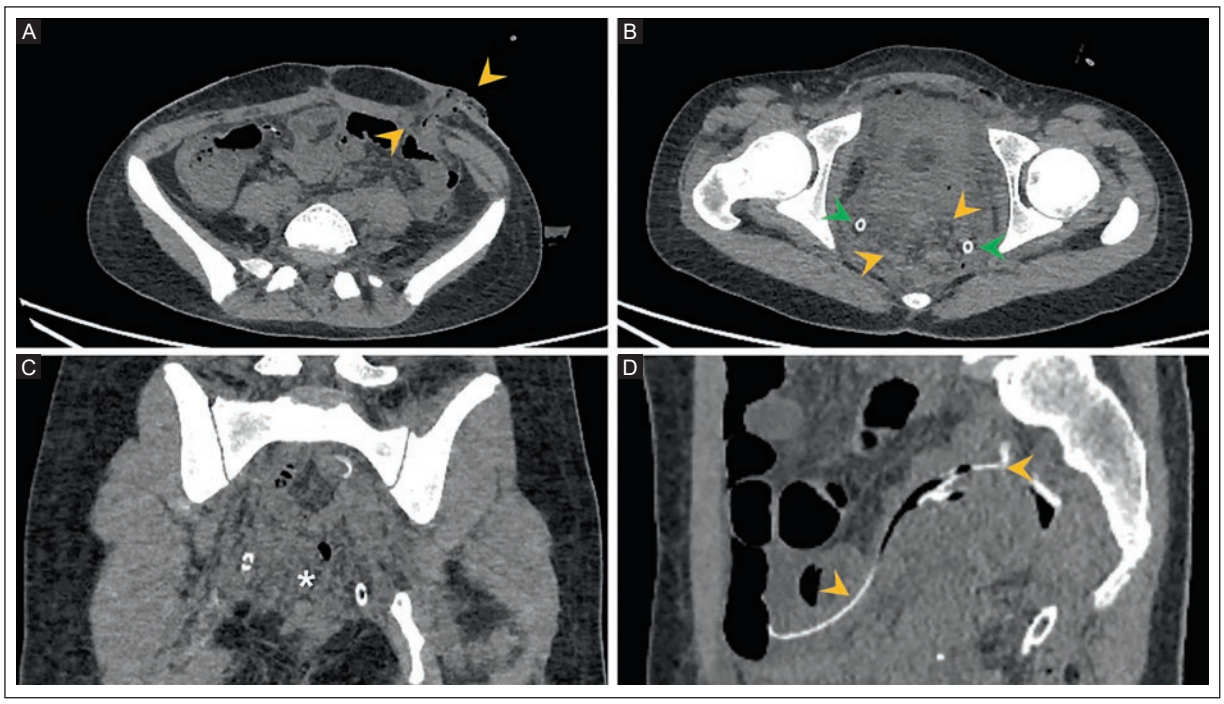

Figure 3. Non-contrast post-surgical abdominopelvic CT. **A:** axial image of a colostomy stoma (orange arrowheads). **B:** axial image shows surgical resection of the anorectal segment (orange arrowheads) and silicone drain tubes in the pelvic cavity (green arrowheads). **C:** coronal image demonstrates persistent serpentine perirectal vessels (asterisk). **D:** a sagittal image shows a silicone drain tube in the pelvis (orange arrowheads).

CT: computed tomography.

unavailable or when clinicians are unfamiliar with this rare entity. Therefore, contrast-enhanced cross-sectional imaging, particularly pelvic MRI, has a crucial role in diagnosis and surgical planning due to its high precision in delineating lesion boundaries and defining their relationship to adjacent anatomical structures[2]. Serpiginous vascular structures and the presence of phleboliths are useful diagnostic signs for cavernous hemangioma[1,3,4,6]. Radiologists must be familiar with the pathognomonic imaging characteristics visible on contrast-enhanced CT and MRI to establish an accurate diagnosis and avoid misdiagnosing malignant neoplasms or benign stenotic processes.

Anorectal cavernous hemangioma commonly occurs insidiously with recurrent rectal bleeding[2-4,6-8]. Although these lesions lack malignant potential, they can cause significant morbidity due to chronic blood loss[9]. The craniocaudal extent in our case exceeded the dimensions typically described in the literature[1,10]. Zhang et al.[11] reported a cavernous hemangioma of the mesorectum involving the rectum measuring approximately 3 × 3 cm. Colonoscopy is often considered the most sensitive modality for detecting gastrointestinal lesions because it allows direct visualization of telangiectasias and vascular nodules[3,4]. When a colonoscopy is inconclusive for diagnosing cavernous hemangioma due to anorectal luminal collapse, as in our case, contrast-enhanced CT and pelvic MRI are essential for accurate diagnosis.

The nonspecific nature of the clinical presentation of cavernous hemangioma leads to a broad differential diagnosis, including proctitis, inflammatory bowel disease, vasculitis, and gastrointestinal neoplasms, often resulting in significant diagnostic delay[4,12]. Angiomatosis is an important differential diagnosis in the evaluation of anorectal vascular malformations. Kaijser categorization provides a systematic framework for distinguishing various vascular lesions in this anatomical region[13]. Hemangioendothelioma or hemangiopericytoma can present with similar characteristics, although very rarely. However, they are considered malignant vascular neoplasms based on the Wood classification[4]. Some anorectal vascular malformations manifest as rigid luminal narrowing with radiological features that mimic carcinoma and stenosis secondary to diverticulitis, ischemia, or radiation[6]. Tariq et al.[2] performed a

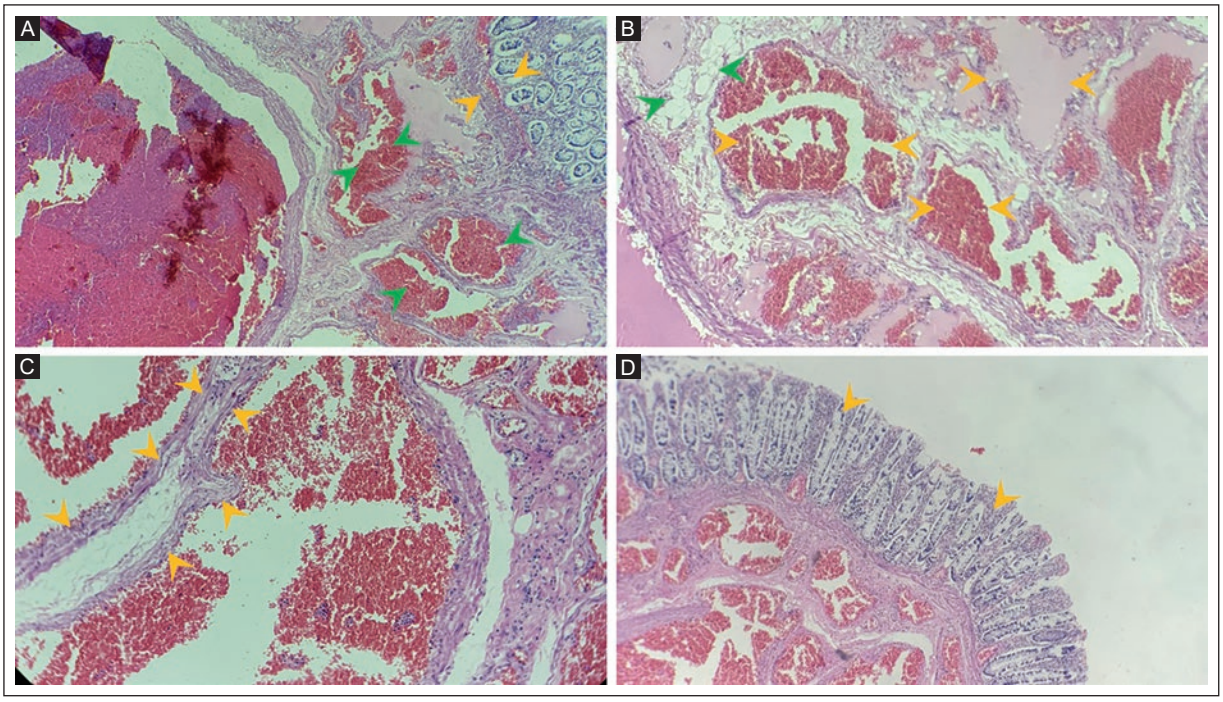

Figure 4. Histopathologic findings of anorectal cavernous hemangioma. **A:** transition zone between rectal mucosa without atypia (orange arrowheads) and vascular channel proliferation with sinusoidal appearance containing partially organized hematic content (green arrowheads) (H&E stain, 5x). **B:** cavernous vascular channels without atypia (orange arrowheads), irregular in shape, size, and contour, intimately apposed in a sinusoidal pattern, embedded within loose connective tissue and fibroadipose stromal tissue (green arrowheads) (H&E stain, 10x). **C:** detail of the cavernous vascular architecture showing wide, thin-walled channels lined by endothelial cells without atypia (orange arrowheads), filled with erythrocytes, confirming the benign nature of the lesion (H&E stain, 40x). **D:** rectal mucosa without atypia (orange arrowheads) displaying nodular protrusion secondary to displacement by an underlying submucosal lesion consisting of cavernous vascular channel proliferation without atypia (H&E stain, 10x).

H&E: hematoxylin and eosin.

double-contrast barium enema in a patient with cavernous hemangioma, which yielded a radiological impression of sigmoid colon carcinoma. Radiologists must be familiar with the pathognomonic findings on contrast-enhanced CT and MRI to establish an accurate diagnosis and avoid misdiagnosis.

While histology remains the definitive diagnostic standard, radiological suspicion helps avoid misdiagnosis and unnecessary invasive procedures[3]. In our case, histopathological analysis of the resected specimen confirmed the diagnosis, revealing dilated, congested submucosal vessels with intraluminal thrombi and hemorrhage, consistent with cavernous hemangioma. Postoperative imaging confirmed successful resection of the primary anorectal segment but also revealed persistent perirectal serpiginous vessels, highlighting the infiltrative nature of these lesions. Djourhi et al.[5] recommend MRI as the preferred modality for both pre- and postoperative evaluation, as it avoids repeated exposure to ionizing radiation and intravenous contrast material associated with CT.

CONCLUSION

This case report of an anorectal cavernous hemangioma underscores the essential role of multimodality imaging in diagnosis. Contrast-enhanced CT and pelvic MRI are the cornerstones that identify the pathognomonic triad: circumferential wall thickening, serpiginous perirectal vessels, and intramural phleboliths. Recognition of these characteristic imaging features by radiologists is critical to prevent diagnostic delays and guide appropriate surgical intervention in patients with chronic gastrointestinal bleeding.

Acknowledgment

We thank Professor Ana M. Contreras-Navarro for her guidance in preparing and writing this scientific paper.

Funding

The authors declare that they have not received funding.

Conflicts of interest

The authors declare no conflicts of interest.

Ethical considerations

Protection of humans and animals. This paper complies with the Declaration of Helsinki (1964) and its subsequent amendments.

Confidentiality, informed consent, and ethical approval. The authors declare they followed their center's protocol for sharing patient data. Informed consent was not required to analyze and publish routinely acquired clinical and imaging data.

Declaration on the use of artificial intelligence. The authors state that they did not use generative artificial intelligence to prepare this manuscript and/or create figures or figure legends.

REFERENCES

1. Ruiz de la Hermosa A, Zorrilla-Ortuzar J, Valle-Hernández ED. Diffuse cavernous hemangioma of the rectum. Cir Cir. 2021;89(6):818-821. doi: 10.24875/ciru.20000746.
2. Tariq Akhtar K, Shahadot Hossain S. Cavernous hemangioma of sigmoid colon and ano-rectum: a rare cause of haematochezia. J Surg Sci. 2019;18(2): 83-86. doi:10.3329/jss.v18i2.43767.
3. Ruiz-Cáez KM, Cure-Michailith JH, Canedo-Matute JA, Jiménez-Canedo J. Cavernous hemangioma of the colon in a young patient. Rev Colomb Gastroenterol. 2021; 36(1): 93-97. doi: 10.22516/25007440.453.
4. Varela-Gutiérrez G, Cervera-Servín JA, Fernández Sobrino G, Rodríguez Delgado N, Flores Armenta J, Robles C. Hemangioma cavernoso del colon. Reporte de un caso y revisión de la literatura. Rev Gastroenterol Mex. 2004; 69(2): 94-99.
5. Djouhri H, Arrivé L, Bouras T, Martin B, Monnier-Cholley L, Tubiana JM. MR imaging of diffuse cavernous hemangioma of the rectosigmoid colon. AJR Am J Roentgenol. 1998;171(2):413-417. doi:10.2214/ajr.171.2.9694466.
6. Levy AD, Abbott RM, Rohrmann CA, Frazier AA, Kende A. Gastrointestinal hemangiomas: imaging findings with pathologic correlation in pediatric and adult patients. AJR Am J Roentgenol. 2001;177(5):1073-1081. doi: 10.2214/ajr.177.5.177107.
7. Amati AL, Hecker A, Schwandner T, Ghanem H, Holler J, Reichert M, et al. Hemangioma of the sigmoid colon mesentery presenting as a retroperitoneal tumor: a case report and review. World J Surg Oncol. 2014; 31(12):79. doi: 10.1186/1477-7819-12-79.
8. Hanatate F, Mizuno Y, Murakami T. Venous hemangioma of the mesoappendix: report of a case and a brief review of the Japanese literature. Surg Today. 1995;25(11):962-964. doi: 10.1007/BF00312382.
9. Oner Z, Altaca G. Diffuse cavernous rectal hemangioma-clinical appearance, diagnostic modalities and sphincter saving approach to therapy: report of 2 and a collective review of 79 cases. Acta Chir Belg. 1993;93(4): 173-176.
10. Guardiola A, Navajas J, Valle J, López-Pardo R, Rodríguez-Merlo R, Lombera M del M, et al. Small bowel giant cavernous hemangioma diagnosed by capsule endoscopy. Rev Esp Enferm Dig. 2012;104(5): 277-278. doi: 10.4321/s1130-01082012000500011.
11. Zhang Y, Wu B. Cavernous hemangioma of the mesorectum involving the rectum: a rare case report. BMC Gastroenterol. 2021;21(1):378. doi. 10.1186/s12876-021-01949-5.
12. Díaz-Ríos R, Pérez-Pereyra J, Perea-Guerrero H, Palomino-Portilla A, Frisancho-Velarde O. Rectorragia intermitente por Hemangioma Difuso de recto. Rev Gastroenterol Perú. 2017;28(2):158-161.
13. Marine R. Cavernous hemangioma of the gastrointestinal tract. Radiology. 1958;70(6):860-863. doi: 10.1148/70.6.860.

JMeXFRI

Journal of the Mexican Federation of Radiology and Imaging

Check for updates

IMAGES IN RADIOLOGY

Head CT: rebleeding subdural hematoma in acute myeloid leukemia

Laura J. Vega-Gonzalez and Abel Medina-Islas*

Diagnostic and Therapeutic Imaging Department, Hospital Español de Mexico, Mexico City, Mexico

A 34-year-old man with acute myeloid leukemia with central nervous system metastases presented to the emergency department with a holocranial headache rated 8 out of 10 on the pain scale, which began after his first intrathecal chemotherapy two months before admission. A non-contrast computed tomography (NCCT) scan of the head revealed a mixed-age subdural hematoma (SDH) with acute and subacute components, mass effect, rightward midline shift, and subfalcine herniation (Figure 1). After treatment with atorvastatin, a follow-up NCCT 12 days later showed a reduction in the size of the hematoma and the rightward midline shift (Figure 2).

SDHs are typically associated with head trauma[1]. In the absence of trauma, their incidence is rare and

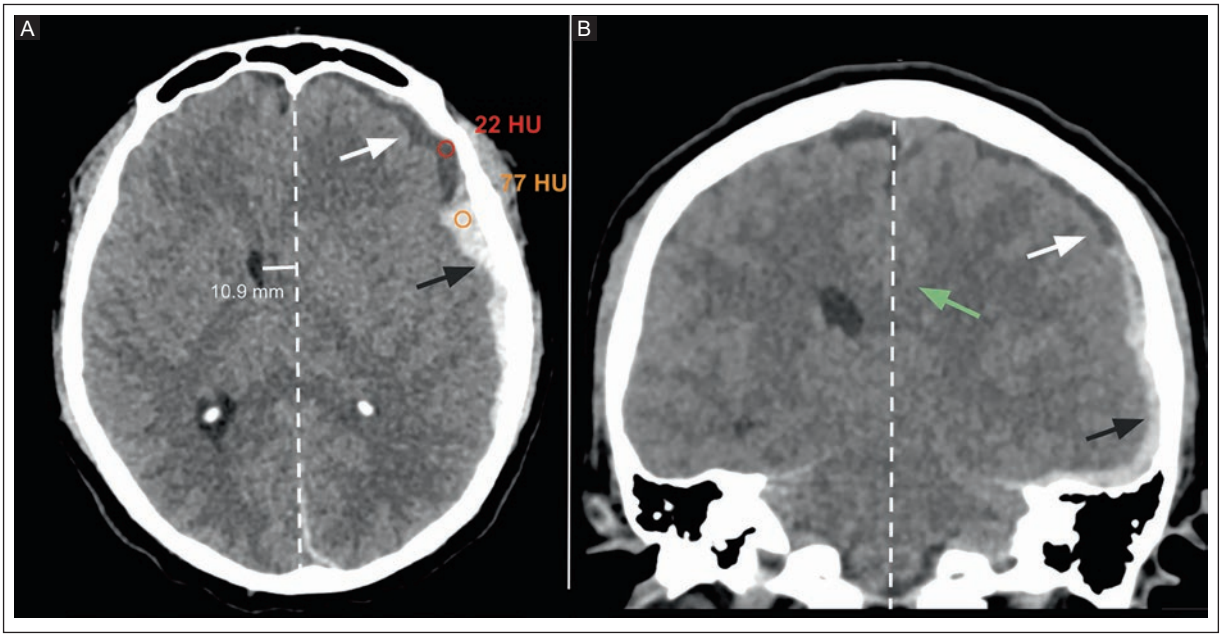

Figure 1. Head NCCT of a 34-year-old man with acute myeloid leukemia and severe headache. **A:** axial section and **B:** coronal reconstruction show a mixed-age SDH overlying and compressing the left hemisphere (white arrows), with 22 HU indicating subacute evolution and 77 HU indicating acute evolution (black arrows). The subdural collection measures up to 11 mm thickness, causing mass effect with a rightward midline shift of 10.9 mm, development of subfalcine herniation (green arrow), and compression of the left lateral ventricle and adjacent brain parenchyma.

NCCT: non-contrast computed tomography; SDH: subdural hematoma; HU: Hounsfield units.

***Corresponding author:**
Laura J. Vega-Gonzalez
E-mail: laura.vega@hospitaleducacion.com

Received for publication: 22-07-2025
Accepted for publication: 24-10-2025
DOI: 10.24875/JMEXFRI.25000019

Available online: 15-01-2026
J Mex Fed Radiol Imaging. 2025;4(4):290-291
www.JMeXFRI.com

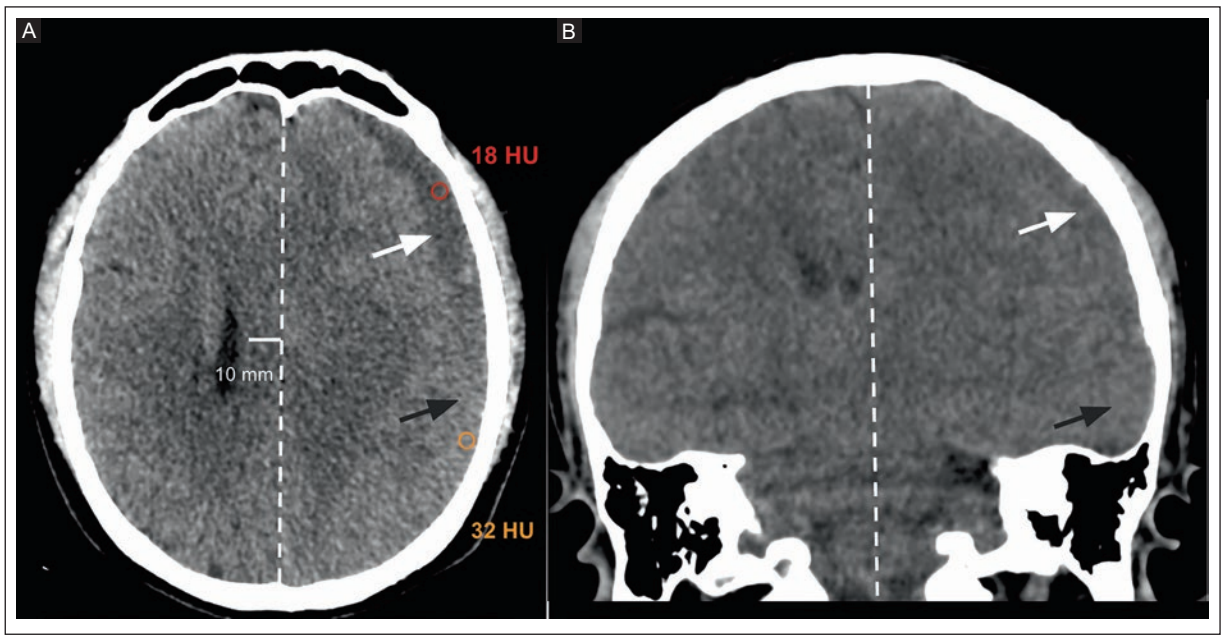

Figure 2. Follow-up head NCCT, 12 days after treatment of a 34-year-old man with acute myeloid leukemia and severe headache. **A:** axial section and **B:** coronal reconstruction. Compared to the previous scan, the diameter of the left hemispheric mixed-age SDH has decreased, with 18 HU (white arrows) and 32 HU (black arrows), and a slight reduction in midline shift (10 mm).
NCCT: non-contrast computed tomography; SDH: subdural hematoma; HU: Hounsfield units.

related to underlying medical conditions, with leukemia being the most common cause. Dural metastases can cause leukocytic stasis, occlusion, and rupture of dural vessels, allowing blood to enter the subdural space[2]. In patients receiving chemotherapy, iatrogenic breach of the subarachnoid space or intracranial hypotension can create traction on bridging subdural veins, leading to SDH with an increased risk of rebleeding[3]. A head NCCT can identify the age of the hematoma by its density: densities greater than 50 Hounsfield units (HU) indicate an acute stage, while densities of 20 to 40 HU suggest a subacute stage[4].

Acknowledgment

We thank Professor Ana M. Contreras-Navarro for her guidance in preparing and writing this scientific paper.

Funding

The authors declare that they have not received funding.

Conflicts of interest

The authors declare no conflicts of interest.

Ethical considerations

Protection of humans and animals. The procedures of this clinical case were conducted in agreement with the Declaration of Helsinki (1964) and its amendments.

Confidentiality, informed consent, and ethical approval. The authors followed the protocols of their work center in the publication of patient data. Informed consent was not required for this article, which used routinely collected clinical data.

Declaration on the use of artificial intelligence. The authors did not use generative artificial intelligence to prepare this manuscript.

REFERENCES

1. Moshref R, Alsinani TA, Al-Sinani A. Case report: surgical management in acute subdural hematoma induced by chronic myelogenous leukemia. Am J Case Rep. 2021;22:e932787. doi: 10.12659/AJCR.932787.
2. Xia G, Zhang W, Xiao J, Shi L, Zhang Y, Xue H. Chronic subdural hematoma caused by acute myeloblastic leukemia: a case report. Front Neurol. 2022;13:911195. doi: 10.3389/fneur.2022.911195.
3. Chia XX, Bazargan A. Subdural hemorrhage - a serious complication post-intrathecal chemotherapy. A case report and review of literature. Clin Case Rep. 2015;3(1):57-59. doi: 10.1002/ccr3.147.
4. Sieswerda-Hoogendoorn T, Postema FAM, Verbaan D, Majoie CB, van Rijn RR. Age determination of subdural hematomas with CT and MRI: a systematic review. Eur J Radiol. 2014;83(7):1257-1268. doi: 10.1016/j.ejrad.2014.03.015.

PHILIPS

Ultrasound

Affiniti

Designed for your everyday

Stepping up to today's Philips Affiniti Ultrasound System means stepping up to the next level of performance to help with a confident diagnosis using streamlined workflow.

Upgrade to the latest Affiniti capabilities

Intuitive use

Experience a user interface and workflow that helps increase your productivity.

- Enhances user workflow with **system-guided protocols** that can be easily customized to suit your needs
- **Tablet-like 30.48 cm (12 in) touchscreen** with workflow-related controls for ease of use
- **Next Gen AutoSCAN reduces button pushes by up to 54%** with pixel-by-pixel real-time optimization and reduces the need for user adjustment while also enhancing transducer plunkability.*
- At just 83.5 kg (184 lb), the system is **16% lighter** than its predecessor system**
- **Shared transducer family** across Affiniti and Compact 5000*** series systems helps maximize your investment
- **Wireless networking** aids workflow

* When comparing VM10 performance to VM7.
** HD15.
*** R.S. #1437E2024 SSA.

Battery backup with sleep mode allows the system to **sleep in 2 seconds and return to full functionality in 20 seconds**

Consumes nearly 40% less power compared to our legacy predecessor system*

Intelligent imaging

Flow Viewer

Defines vasculature with a 3D-like appearance using both the velocity and power of the Doppler signal to accurately represent vascular flow topography

MicroFlow Imaging (MFI)

Provides remarkable sensitivity and detail in assessing blood flow

Find out more at
www.philips.com.mx/healthcare/solutions/ultrasound

Lunit

Improved Diagnostic Accuracy, Especially for Dense Breasts

Automatically analyze and generate quantitative density assessment

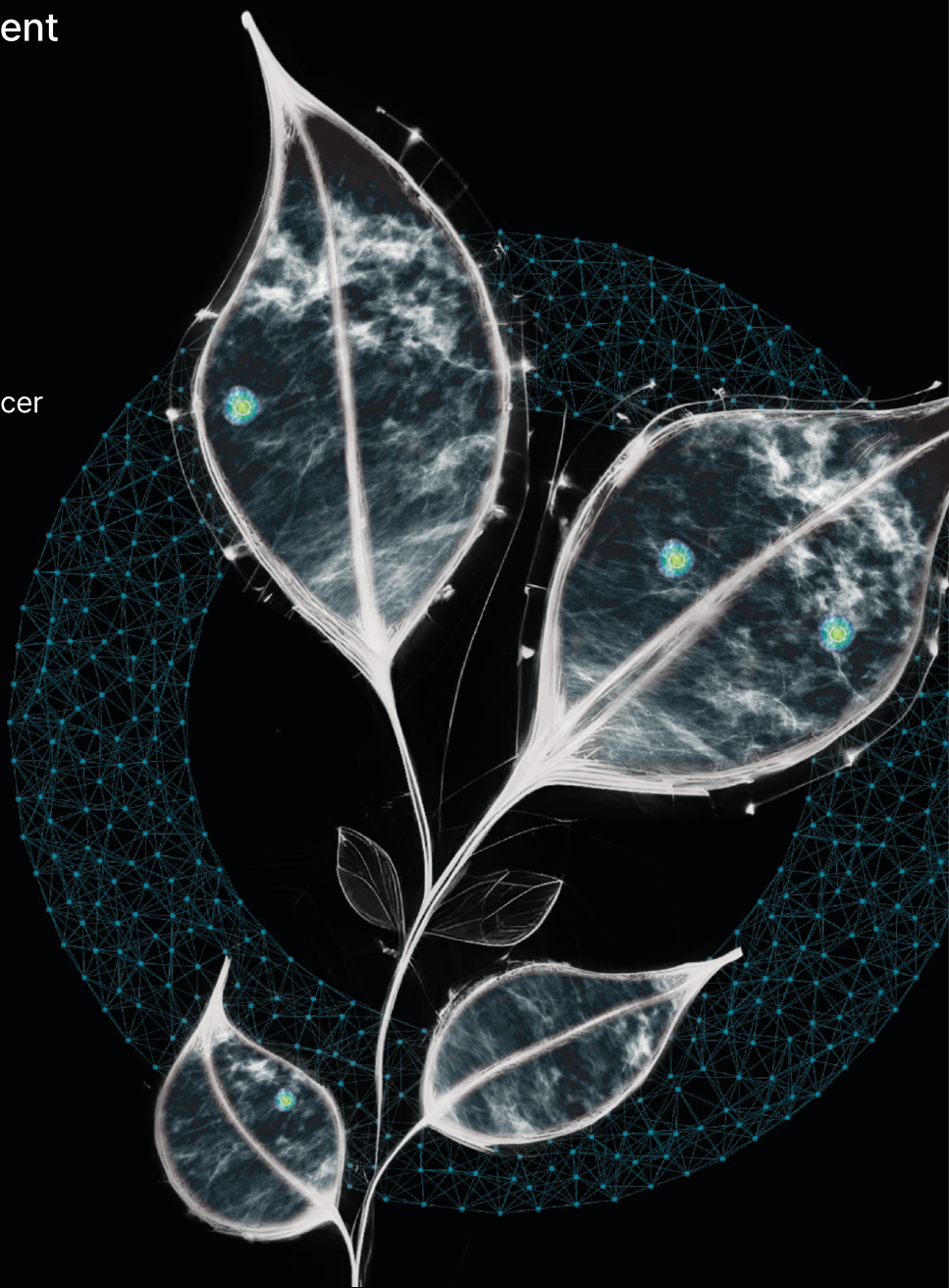

Lunit AI-driven technology empowers radiologists to:

- Enable early diagnosis for breast cancer
- Reduce radiologists reading volume
- Automatically analyze and generate quantitative density assessment
- Promote workflow efficiency

Informed decisions to conquer cancer

Lunit #13
lunit.io

FUTURA MEDICA

DIAGNÓSTICOS EN RADIOLOGÍA & LABORATORIO

SUPPORTING RADIOLOGY MEDICAL EDUCATION SINCE 1979

www.futuramedicademorelia.com

EI

Diagnóstico Especializado en Imágen

Dr. Gerardo S Navarro Gomez
Radiologist

Dr. Eduardo Sarda Inman
Radiologist

Dra. Beatriz Gonzalez Ulloa
Radiologist

Clinical Laboratory	General Ultrasound
Digital Radiology	Color Doppler Ultrasound
Digital Mammography	4D Structural Obstetric Ultrasound
Tomosynthesis	Musculoskeletal Ultrasound
Contrast-Enhanced Mammography	Peripheral Doppler Ultrasound
Computed Tomography (CT)	gnetic Resonance Imaging (MRI)

Guadalajara, Jalico. Mexico

imax ...te da Vida

Advanced Specialization Course in Breast Imaging

Hybrid Program (Academic-Work-Based)

*Theoretical and Practical
*100% On-Site

*Accredited by:

IEST ANÁHUAC

+52 833 212 9170 +52 833 658 5800

Tampico, Tamaulipas, México.

RADIOLOGY SOLUTIONS

YOUR TRUSTED CABINET

OAXACAN RADIOLOGY OFFICE DEDICATED TO OFFERING IMAGING SERVICES.

Committed to offering image quality and diagnostic certainty to its patients and doctors in Imaging studies.

OUR SERVICES:

Tomography | Ultrasonido

Special X-rays | X-rays

LOCATION:

Calle Álamos #603, Col. Reforma, between Jazmines and Heroico Colegio Militar, Oaxaca de Juárez, Oaxaca.